

The Material Separation Process for Recycling End-of-life Li-ion Batteries

Liurui Li

Dissertation submitted to the faculty of the Virginia Polytechnic Institute and State University

in partial fulfillment of the requirements for the degree of

Doctor of Philosophy

In

Mechanical Engineering

Zheng Li

Michael W Ellis

Rui Qiao

Alex O Aning

9/25/2020

Blacksburg, VA

Key words: Battery Recycling, Material Separation, Automated Disassembly, Design of Experiment

Copyright (2020)

The Material Separation Process for Recycling End-of-life Li-ion Batteries

Liurui Li

Abstract

End-of-life lithium-ion batteries retired from portable electronics, electric vehicles (EVs), and power grids need to be properly recycled to save rare earth metals and avoid any hazardous threats to the environment. The recycling process of a Lithium-ion Battery Cell/Module includes storage, transportation, deactivation, disassembly, and material recovery. This study focused on the disassembly step and proposed a systematic method to recover cathode active coating, which is considered the most valuable component of a LIB, from end-of-life LIB pouch cells. A semi-destructive disassembly sequence is developed according to the internal structure of the LIB cell. A fully automated disassembly line aiming at extracting cathode electrodes is designed, modeled, prototyped, and demonstrated based on the disassembly sequence. In order to further obtain the coating material, the extracted cathode electrodes are treated with the organic solvent method and the relationship between process parameters and cathode coating separation yield is numerically studied with the help of Design of Experiment (DOE). Regression models are then fitted from the DOE result to predict the cathode coating separation yield according to combinations of the process parameters. The single cell material separation methodology developed in this study plays an important role in the industrial application of the direct recycling method that may dominate the battery recycling market due to its environmental friendly technology and high recovery rate regardless of element type in the short future.

The Material Separation Process for Recycling End-of-life Li-ion Batteries

Liurui Li

General Audience Abstract

The bursting demand of lithium-ion batteries from portable electronics, electric vehicles, and power grids in the past few years not only facilitate the booming of the lithium-ion battery market, but also put forward serious global concerns: Where should these batteries go at their end-of life and how should they be treated in a safe and harmless manner. As a metal enriched “city mine”, end-of-life LIBs are expected to be properly stored, transported, deactivated, disassembled, and recovered with sufficient safety precautions to prevent fire, explosion or any hazardous emissions. This study focuses on the disassembly procedure and emphasized automated battery disassembly techniques and the improving of material separation efficiency. A disassembly sequence of the pouch cell is scheduled and optimized for the first time. To realize the scheduled sequence, a fully automated pouch cell disassembly system is designed to achieve semi-destructive disassembly of z-folded pouch cells. Fixtures, transporters and end-effectors were prototyped and assembled into the modularized disassembly line which extracts cathode electrodes as final product. Cathode electrodes as the most valuable component in a LIB then need to go through multiple chemical-mechanical treatments to future separate cathode coating and Al current collector. This study utilized DOEs to optimize the operating parameters of the material separation process for Lithium cobalt oxide (LCO) coating and Lithium iron phosphate (LFP) coating. Regression models are successfully established for yield prediction with certain levels of control factors.

Acknowledgement

Firstly, I would like to express my sincerest gratitude to my advisor, Dr. Zheng Li. Without his professional guidance on both theoretical and experimental aspects of my research, I could not have finished my Ph.D. study. His passion for research and creative research intuition has inspired me profoundly. I feel extremely lucky to have Dr. Zheng Li as my committee chair.

I also want to thank my committee members: Dr. Michael Ellis, Dr. Rui Qiao, and Dr. Alex Aning for their guidance and encouragement on my research work.

I must thank Yingqi Lu, Tairan Yang, Panni Zheng, and Dayang Ge who I cooperated with in the same research group during the past three years. They always spared no effort to help me whenever I'm in trouble with my research or daily life. I could not thank more for their selfless assistance.

Special thanks to my parents and my wife, Yuxian Ye. Having their company to share happiness and sorrow is the best thing that could happen to me in my life.

Table of Content

Chapter 1 Introduction	1
1.1 Lithium-ion Battery Technology.....	1
1.1.1 Lithium-ion Battery Electrochemical Mechanism	1
1.1.2 Lithium-ion Battery Manufacturing	4
1.1.3 Lithium-ion Battery Retirement.....	7
1.2 State-of-the-Art Pretreatment Process in End-of-Life (EoL) LIB Recycling	10
1.2.1 Recycling strategies overview	10
1.2.2 Module/Pack Disassembly.....	12
1.2.3 Material Separation.....	14
1.3 State-of-the-Art Material Recovery Process in EoL LIB Recycling.....	19
1.3.1 Pyrometallurgical Processes	19
1.3.2 Hydrometallurgical Processes	20
1.3.3 Direct Recycling Processes	24
1.3.4 Comparison of Three Major LIB Recycling Methods	26
1.5 Outline of this Dissertation	28
Chapter 2 Disassembly Automation for Pouch Cells	31
2.1 Disassembly Sequence Planning.....	33
2.1.1 Disassembly Mode Selection	33
2.1.2 Disassembly Precedence (DP) Confirmation	37
2.1.3 Modules Design	41
2.2 Modules Design and Prototype	43

2.2.1 Pouch Trimming Module	43
2.2.2 Housing Removal Module	46
2.2.3 Electrode Sorting Module	48
2.3 System Integration and Testify	51
2.3.1 Control Architecture	51
2.3.2 Concept Verification	53
2.4 Sorting Module Upgrade and Future Development	56
2.4.1 Sorting Module Upgrade.....	56
2.4.2 Cyber-physical Closed-loop Controller and Preliminary Experiments	60
2.5 Conclusion	66
Chapter 3 Cathode Coating Separation of Lithium Cobalt Oxide Battery	67
3.1 Experiment Setup.....	69
3.2 Placket-Burman Parameter Screening Experiment.....	71
3.2.2 Placket-Burman Parameter Screening Experiment Design	71
3.2.3 Parameter Screening Results.....	73
3.3 Taguchi DOE	76
3.3.1 Experiment Design.....	76
3.3.2 Taguchi DOE Results	79
3.3.4 Linear Regression Model for Yield Prediction	82
3.4 Conclusion	84
Chapter 4 Cathode Coating Separation of Lithium Iron Phosphate Battery	85
4.1 Full-Factorial Experiment Setup.....	85

4.2 Result and Discussion	89
4.2.1 Full-factorial DOE Separation Yield	89
4.3.2 Regression Analysis	92
4.3.3 Correlation Pre-confirm with Contour Plot and Latin Square.....	94
4.3 Conclusion	97
Chapter 5 LFP Direct Recycling.....	99
5.1 EoL LFP Direct Regeneration.....	99
5.2 Coin Cell Assembly	104
5.3 Electrochemical Performance of the Regenerated LFP	106
5.4 Conclusion and Future Development.....	108
Chapter 6 Summary and Future Work	109
6.1 Summary of Contributions.....	109
6.2 Future Work.....	110
REFERENCES.....	113

List of Figures

Figure 1-1 Schematic illustration of a typical lithium cobalt oxide battery ¹⁷	2
Figure 1-2 Three categories of ESCs differentiated by continuity of electrodes and separator ³³ ...	6
Figure 1-3 Solid-electrolyte interface development and aging on anode surface ⁴²	9
Figure 1-4 General flow sheet of EoL LIB recycling processes (modified from ⁸²)	12
Figure 1-5 (a) Hybrid disassembly workstation and (b) Robot flange with electric screwdriver ⁹⁰	14
Figure 1-6 Pretreatment processes summary for recycling EoL LIBs in industrial scale and lab scale ⁹⁹	15
Figure 1-7 Process steps of a typical destructive material separation process ¹⁰⁶	17
Figure 1-8 Experimental set-up for the ANVIL process ⁹⁷	18
Figure 1-9 Flow sheet for a typical hydrometallurgical process of LiCoO ₂ from spent LIB ¹²⁶ ..	21
Figure 1- 10 Material flow of the direct recycling process ¹⁵⁶	24
Figure 1- 11 Direct regeneration process flow diagram of cathode material mixture ⁸¹	25
Figure 1- 12 Comparison of different LIB recycling methods ⁸³	27
Figure 2-1 Configuration of the H605060 lithium-ion polymer rechargeable battery manufactured by MTI Corporation.....	35
Figure 2-2 Detailed 2D specification of the H605060 lithium-ion polymer rechargeable batteries from MTI Corporation.	36
Figure 2-3 Disassembly matrix of Z-folded pouch cells.	38
Figure 2- 4 Disassembly precedence graph and module function division.	41
Figure 2-5 Continuous process for recovery of cathode coating from end-of-life LIBs.	42
Figure 2-6 (a) CAD design and (b) Prototype of the pouch removal module.	44

Figure 2-7 Detailed design of the pinch roller conveyor set: (a) side view in CAD model, (b) top view in CAD model, (c) assembly overview in CAD model, and (d) top view of prototyped pinch rollers.	45
Figure 2- 8 (a) Schematic and (b) Prototype of the pouch removal module.....	46
Figure 2- 9 Design of the vacuum grip (a) front view and (b) side view	47
Figure 2-10 (a) Schematic and (b) Prototype of the electrode sorting module.....	49
Figure 2-11 Pneumatic securing unit for separator delivery.....	50
Figure 2-12 Control architecture of the prototyped automatic recycling system	52
Figure 2- 13 Prototyped H605060 LIB disassembly system overview.	53
Figure 2-14 Z-folded dummy cell assembly line following the size of a H605060 LIB: (a) Die cut machine, (b) Al laminated film stamping machine, (c) ESC folding machine, (d) Heat sealing machine, (e) Vacuum sealing machine, (f) Trimmed Al foils, (g) Stamped Al laminated film, (h) Folded dummy ESC, (i) Dummy cell with one side edge and the top edge heat sealed, and (j) Vacuum sealed dummy cell.	54
Figure 2- 15 12 key frames from system testing record corresponds to (a) handling scenario 2, 3, 4, and 5 of the trimming module, (b) handling scenario 1, 4, 8, and 11 of the housing removal module, and (c) handling scenario 1, 3, 4, and 5 of the electrode sorting module.	55
Figure 2-16 Vision-sensor network components: (a) FLIR S USB3 mono industrial cameras with 1.6MP resolution and 226 FPS, and (b) Tension sensor modified from strain gage based load cell.....	57
Figure 2-17 Schematic of the vision-sensor network integrated electrode sorting module.....	58

Figure 2-18 System operating with EoL H605060 LIB: (a) Upgraded sorting system overview, (b) Operating frame of industrial camera #2, (c) Operating frame of industrial camera #3, (d) Operating frame of industrial camera #1, and (e) Reading from the load cell.	59
Figure 2-19 LabVIEW control unit Front User Interface: (a) Image acquisition section, (b) Load cell reading section, and (c) Linear motion control section.....	59
Figure 2-20 Control architecture of the cyber-physical closed-loop process monitor for the electrode sorting module.....	60
Figure 2-21 Algorithm input (a) intact separator and (b) cracked separator.	61
Figure 2-22 Layered structure of CNN working principle ¹⁸³	62
Figure 2-23 Examples of image classification result and probability value.	63
Figure 2-24 (a) Structure of the confusion matrix and (b) Confusion matrix of the preliminary algorithm.	65
Figure 3-1 Battery modules disassembled for DOE.	69
Figure 3-2 Equipment requirement (a) Battery module discharger, (b) High temperature oven, and (c) Ultrasonic cleaner.	70
Figure 3-3 Experiment flow with single cathode electrodes.	71
Figure 3-4 Main effects plot for fitted means of screening experiment yield.	76
Figure 3-5 Main effects plot for S/N ratio.	81
Figure 4-1 (a)Tenergy 3.2V 2500mAh LFP (IFR26650P) power cell rechargeable battery and (b) Typical internal structure of a cylindrical LIB.	87
Figure 4-2 The appearance of (a) the original LFP cathode electrode and the appearance of the LFP cathode electrode soaked in NMP under 90°C after (b) 2h, (c) 3h, and (d) 4h.....	88
Figure 4-3 Main effect plot for separation yield.	90

Figure 4-4 Fully separated LFP cathode coating (a) naturally detached from the Al current collector during soaking, and (b) coating expansion comparison with the Al current collector. .	91
Figure 4-5 The contour plot plotted from the result of (a) the full factorial experiments and (b) the latin square sampling subset.	97
Figure 5-1 Process flow of the EoL LFP regeneration process.	101
Figure 5-2 The XRD patterns of as-purchased LFP from MSE Supplies, EOL cathode materials, and recycled cathode materials sintered under 550°C , 650°C, 750°C within Ar&H ₂ atmosphere, and recycled material sintered under 750°C in Ar atmosphere.....	102
Figure 5-3 The SEM images of (a) as-purchased LFP from MSE Supplies, (b) EOL LFP, regenerated LFP sintered under (c) 550°C , (d) 650°C, (e) 750°C within Ar&H ₂ atmosphere, and regenerated LFP sintered under (f) 750°C in Ar atmosphere.	103
Figure 5-4 Cathode electrodes preparation for coin cell assembly.....	105
Figure 5-5 (a) Coin cell assembly explosive view, (b) MSK-160E digital coin cell assembly crimper, (c) assembled CR2032, and (d) CT2001A classic battery tester.....	106
Figure 5-6 The charge/discharge voltage profiles at 0.1C (a) and rate performance (b) of cathode active material mixtures sintered under different conditions.....	107

List of Tables

Table 3-1 Screening experiment parameters and levels.	73
Table 3-2 Plackett-burman screening experiment design and result.	73
Table 3-3 Analysis of variance of screening experiment.....	75
Table 3-4 Taguchi experiment parameters and levels.	78
Table 3-5 Pre-set process parameters.	78
Table 3-6 Taguchi L16 orthogonal array and the corresponding separation yield.	79
Table 3-7 Response table for S/N ratio.....	81
Table 3-8 Taguchi experiment analysis of variance for S/N ratio.	82
Table 3- 9 Summary table of the regression model for LCO separation yield.	83
Table 3-10 Linear regression model for predicting LCO separation yield verification test result.	84
Table 4-1 Full-factorial experiment parameters and levels.	87
Table 4-2 Separation yield of the cathode coating in 2 factors, 4 level full-factorial experiment.	89
Table 4-3 Summary table of the regression model for LFP separation yield.	92
Table 4-4 ANOVA table for the regression analysis.	93
Table 4-5 Result of the non-linear regression model verification tests.	94
Table 4-6 A LSD of the 2 factors and 4 levels experiment.	95
Table 4-7 Latin square design of 2 factors and 4 levels full-factorial experiment.	95
Table 4- 8 LFP separation yield of the selected Latin Square sampling subset.	96

Chapter 1 Introduction

1.1 Lithium-ion Battery Technology

1.1.1 Lithium-ion Battery Electrochemical Mechanism

Lithium was first introduced into batteries by M. Stanley Whittingham in 1970s¹ at which time titanium sulfide and lithium metal were used as the electrodes. Unaffordable prices of titanium sulfide and insufficient voltage prevented the commercialization of such combinations. In 1980, John B. Goodenough demonstrated a lithium-ion secondary battery consisted of Lithium cobalt oxide (LCO) as positive electrode and lithium metal as negative electrode². The innovated combination enabled stable LCO to act as lithium donor, which allowed the negative electrode to be replaced by lithium holders other than lithium metal. The first generation of commercial lithium-ion battery that suits for industrial-scale mass production was invented by Akira Yoshino in 1985³. He introduced carbonaceous with a certain crystalline structure as the negative electrode after polyacetylene proved to be unstable and too low in density. Till present, lithium-ion batteries have been dominating the market of portable electronics and EVs and revolutionized our daily lifestyles. For this and so much more conveniences the technology has brought us, the 2019 Nobel Prize in chemistry was rewarded to John B. Goodenough, Stanley Whittingham, and Akira Yoshino for the development of lithium-ion batteries⁴.

A typical LIB consists of four essential components: positive electrode, negative electrode, electrolyte, and separator (Figure 1-1). A positive electrode typically consists of a metal oxide and conductive additives held onto an aluminum current collector by a binder. Positive materials can be layer structured (LiCoO_2), olivine structured (LiFePO_4), and spinel

structured (LiMn_2O_4)^{5,6}. Currently, negative electrodes on commercialized LIBs are mostly made from graphite and other carbon material coated onto a copper current collector by the same binder as the positive electrode. Ever since Rachid Yazami demonstrated the capability of the graphite in reversibly intercalating lithium-ion within a LIB cell⁷, graphite has been the dominant material for negative electrodes because of its low voltage, modest volume expansion, and high performance^{8,9}. Electrolytes can be liquid, gel, or dry polymer¹⁰⁻¹². As the most widely adopted type, the liquid electrolyte is usually a lithium salt such as lithium hexafluorophosphate (LiPF_6), lithium hexafluoroarsenate monohydrate (LiAsF_6), lithium perchlorate (LiClO_4), lithium tetrafluoroborate (LiBF_4), and lithium triflate (LiCF_3SO_3) dissolves into organic solvent blends of ethylene carbonate, dimethyl carbonate, or diethyl carbonate¹³. Additives such as vinylene carbonate (VC) and Lithium bis(oxalato) borate (LIBOB) are selectively added to help with the formation and stabilization of Solid-liquid Interface (SEI), improvement of overcharge tolerance, or capability of Li cycling¹⁴. Separators are critical components in LIB batteries that utilize liquid electrolyte. A separator is an ion-permeable porous membrane consisting of conventional polyolefin coated by ceramic particles under certain circumstances to improve thermal stability^{15,16}.

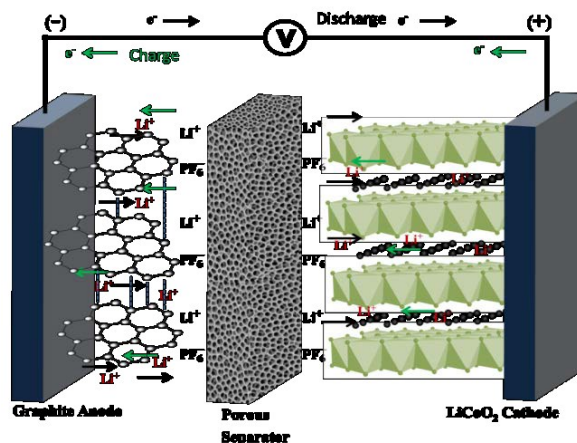


Figure 1-1 Schematic illustration of a typical lithium cobalt oxide battery¹⁷.

The term “rocking-chair battery” was invented to describe the working principle of a LIB: Lithium ions transporting back and forth by the electrolyte between cathode electrodes and anode electrodes through separators¹⁸. As demonstrated in Figure 1-1, both electrodes allow lithium ions to intercalate into and deintercalate out from their structures to form compounds containing lithium atoms. During charging process represented by green arrows, positively charged lithium ions deintercalate out from layered LCO (cathode) in an oxidation reaction when energy is provided from external circuit (Eq.1-1 left to right). They diffuse towards graphite (anode) in LiPF_6 solution (electrolyte) and migrate through separators that insulate cathode and anode electrodes. Simultaneously, electrons move from positive electrode to negative electrode through the external circuit and enable lithium ions to intercalate into layered graphite (anode) (Eq.1-2 left to right) to fulfill the energy storage process (Eq.1-3 left to right) during which liquid electrolyte and external circuit performed as conductive media for lithium ions and electrons accordingly. At this stage, LIBs are at high energy state and their open-circuit voltage (OCV) highly depends on electrochemical potentials of both positive electrodes (anode) and negative electrodes (cathode). When fully charged LIBs connected to external loads, the discharging process executes backward reactions and the majority of lithium ions would be transferred back to the positive electrode (cathode), thus lowering the potential and the energy state of the cell. Noticing that anode and cathode actually change positions during charge and discharge process. To avoid confusion for the rest of this dissertation, cathode will represent metal oxides that act as actually cathode electrode during discharging process at the positive terminal marked on the battery shell and anode will represent carbon based anode electrode during discharging process at the negative terminal. The transition metal, cobalt, in $\text{Li}_{1-x}\text{CoO}_2$ at cathode oxidized from Co^{3+} to Co^{4+} during charging and reduced from Co^{4+} to Co^{3+} during

discharging. The overall charging reaction and discharging reaction shown in Eq.1-3 was used in the first commercial LIB developed by Sony and Asahi Kasei in 1991.

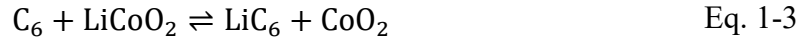
The cathode half reaction (left to right: charging, right to left: discharging):



The anode half reaction (left to right: charging, right to left: discharging):



The overall reaction (left to right: charging, right to left: discharging):



The success of commercial LIB utilizing liquid electrolyte has everything to do with the existence of a passive film namely solid-electrolyte interface (SEI) formed on anode surface. Since anodes operate at voltages that are much lower than the electrochemical stability window of electrolytes, a small amount of electrolytes tend to decompose and form this film during the first few cycles of a freshly assembled LIB at the cost of some irreversibly consumed lithium ions¹⁹. The formation of SEI not only prevents the further decomposition of electrolytes but maintains sufficient permeability for lithium ions²⁰. Changes of SEI throughout the life cycle of a LIB are considered as one of the major sources of LIB degradation at the anode^{21,22}.

1.1.2 Lithium-ion Battery Manufacturing

The manufacturing process of LIBs can be divided into three stages: electrode production, cell production, and cell conditioning. For LIB modules, an extra cell quality sorting and module assembly process is needed^{23,24}.

Most electrode production processes are based on wet coating and roll-to-roll technique^{25,26}. Active material, conductive additives, and polymer binder are firstly dry (optional) or wet mixed depending on whether the polymer binder is pre-dissolved in the

organic solvent (N-Methyl-2-Pyrrolidone, NMP). After degassing and filtering, the homogenous suspension is then continuously coated on both sides of the current collector sequentially by the slot die. The aluminum (cathode) and copper (anode) current collector should have high conductivity, tensile strength, and surface adhesion as well as low E-modulus and thickness variation²⁷. The coated current collector then goes through a dryer under a moisture-free environment. The organic solvent (NMP) evaporated from the wet coating during the drying process needs to be recovered and recycled for both cost and environmental concerns. Finally, the dried electrodes are compressed between two rollers separated by a certain distance to acquire desired electrode thickness. The compression step also enhances the energy density, conductivity, and adhesion as well as decreases the porosity of the coated active material^{28,29}.

The cell production stage firstly cuts the dried continuous electrodes and properly insulates cathode and anode by polymer separator to form the electrode-separator compound (ESC). Depending on the continuity of electrodes and separator, configuration of ESCs can be divided into three categories as shown in Figure 1-2: stacking, winding, and Z-folding³⁰. The stacked ESC consists of both discrete electrode sheets and discontinuous separator, which is suitable for relatively large format batteries. The uniformed mechanical load was applied throughout the entire sheet so that thicker electrodes could be involved to improve energy density. Nevertheless, discontinuous components raise the requirement for precision alignment and obviously decreases productivity. The second ESC configuration is winding, which can either be cylindrical or prismatic in shape³¹. Continuous electrodes and separator decrease the assembly time to seconds without introducing any misalignment concerns. But the bending nature of this ESC type and crack formation risk limit its energy density and electrode format, especially electrode thickness³². Compared to two designs above, Z-folding ESC is a more

balanced configuration between productivity and yield. The continuous separator is folded into zig-zag shape and discrete cathode and anode sheets are inserted in-between alternately. Since electrodes insulated by the separator are stacked in a plane, the advantage of the stacking ESC applies to Z-folding as well. The continuous separator also decreases the number of items for assembly and the difficulty for alignment.





		Electrodes	
		discrete	continuous
Separator	discrete	 stacking	
	continuous	 z-folding	 winding

Figure 1-2 Three categories of ESCs differentiated by continuity of electrodes and separator³³.

Cathode and anode electrodes in assembled ESCs are then welded to metal tabs for positive terminal and negative terminal correspondingly before being inserted to an open housing^{23,31}. The housing of LIBs can be divided into three main categories: cylindrical, prismatic hard case, and prismatic pouch cell. Cylindrical cells have the highest productivity but relatively low energy density when assembled into modules and packs due to insufficient usage of the space. Prismatic hard cases provide the best protection for ESCs against external mechanical impacts in trade of volumetric energy density and specific energy density. The prismatic pouch cell utilizes formed aluminum laminated film as case to provide sufficient

insulation and protection to ESC. After filling in the electrolyte, housings will be closed and sealed to finish the cell production stage.

The initial few cycles of charging and discharging of a newly assembled cell is called the formation process^{34,35}. SEI layers are expected to form due to decomposition of the electrolyte at the surface of electrodes, especially anode. During this process, gaseous electrolyte decomposition products such as ethylene (from ethylene carbonate), propylene (from ethylene carbonate), or CO_2 gas^{36,37} will accumulate inside sealed battery housings. Pre-designed pressure relief valves enable cylindrical cells and prismatic hard-case cells to naturally degas in the formation process while prismatic pouch cells rely on an additional pouch bag attached on one side edge to absorb the gas and eventually cut off from the cell³⁸. The aging process is the final step of the cell production which is also the most time consuming step (2-3 weeks³⁹). Cell aging performance will be used to identify short circuits and classify individual cells according to their capacity, impedance, efficiency, etc. The classification result is of vital importance to increase uniformity of battery modules, thus benefit equalization in battery management system (BMS)⁴⁰.

1.1.3 Lithium-ion Battery Retirement

Although unique advantages in power, energy density, self-discharge rate, and operating temperature window⁴¹ have helped LIBs widely adopted in EVs and energy storage plants in recent years, their lifespan studies are still catching much attention in both academia and industry. LIBs are expected to have a lifespan of 15 years for 42V battery systems and hybrid electrical vehicles (HEV's) and 10 years for electrical vehicles (EV's) or up to 1000 cycles at 80% depth-of-discharge (DOD) according to United States Advanced Battery Council (USABC)⁴². Apart from lithium intercalate/deintercalate reaction, massive side reactions such

as electrolyte decomposition, active substance dissolution, and lithium metal plating are simultaneously proceeding within each charging-discharging cycle⁴³⁻⁴⁵. Thus the degradation of a LIB is a complex process that may be caused by changes of anode, cathode, and electrolyte throughout the entire life-cycle^{42,46,47}.

At the anode side, the degradation mainly comes from changes at the SEI^{21,48-52}. The formation of SEI during the first few cycles of a newly assembled LIB decreases the total amount of free Lithium and increases the impedance of the cell for the greater good of the anode and electrolyte protection^{45,53}. However as LIB cycles, electrolyte reduction reactions by the anode continue at a low rate and gradually thicken the SEI thus causing further lithium loss and impedance rise³⁷. The growth of SEI also decreases the accessible surface area for lithium-ion to pass through SEI and further increases the impedance^{54,55}. Conditions such as high operation temperature and high SOC accelerate such processes^{56,57}. When LIB operates under low temperature or high cycling rate, metallic Lithium tends to plate on the anode surface and result in subsequent electrolyte decomposition by metallic Lithium. Consequently, capacity and power of the LIB will fade due to loss of lithium and electrolyte^{58,59}. As embedded Lithium further accumulates, lithium dendrites start to form as shown in Figure 1-3. The growth of lithium dendrites can pierce the porous separator and cause a short circuit that leads to thermal runaway^{60,61}. Meanwhile, the lithium intercalation and deintercalation processes are accompanied with volume change of electrode material (around 10% for graphite anode)⁶². High cycling rates (fast charging for example) and state of charge induces extra mechanical strain due to faster and larger volume change that may cause orientation of the graphite particle compared to the original state and accelerate the fade⁶³.

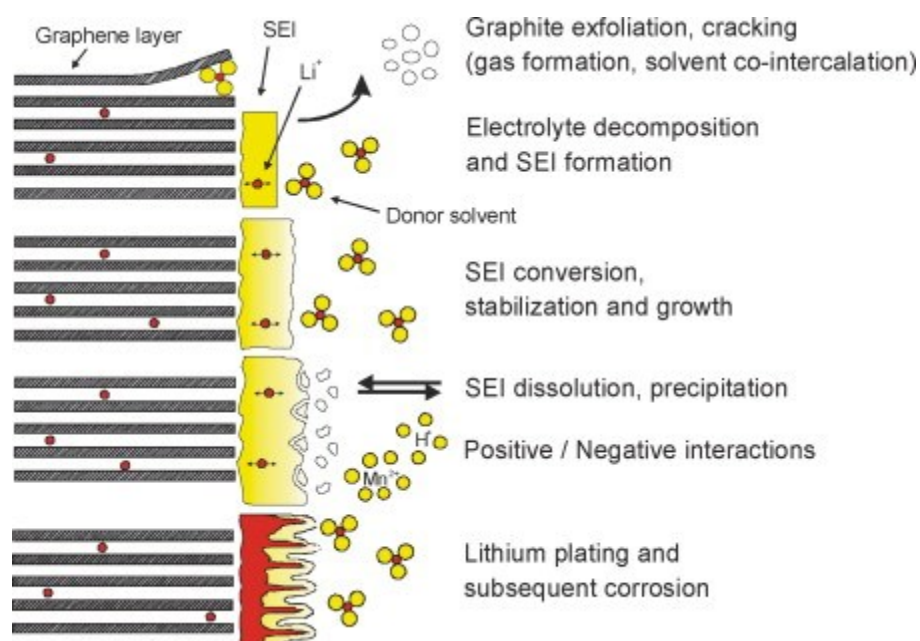


Figure 1-3 Solid-electrolyte interface development and aging on anode surface⁴².

Degradation from electrolyte mainly caused by electrolyte decomposition due to abusing operation conditions of battery cells⁶⁴. When overcharged to 4.5V or above (with respect to Li/Li⁺), the electrolyte will be oxidized at the cathode and form insoluble substances like Li₂CO₃ and LiF. For most commercial Li-ion, the degradation of the SEI layer will accelerate at a cell temperature of 75 – 90°C^{65,66}. The loss of SEI above such temperature will lead to continuous reduction reaction between electrolyte and Li metal enriched anode.

Similar to anode, lithium intercalate/deintercalate also lead to volume change of the cathode material, thus introducing mechanical stress and distortion of the crystal lattice⁴². Other cathode changes may reduce the lifespan of a LIB include but not restricted to: cathode SEI formation due to electrolyte oxidation^{67,68}, Mn dissolution^{47,69}, and high temperature decomposition^{40,70}.

1.2 State-of-the-Art Pretreatment Process in End-of-Life (EoL) LIB Recycling

As transition metals enriched city mines, EoL LIBs are of great value if treated properly. For example, cobalt enriched LCO batteries have the potential recycling value of \$8900 per ton which is the highest among all common cathode materials while Lithium manganese oxide (LiMn_2O_4 or LMO) batteries are lowest in recycling value at around \$860 per ton⁷¹. Currently, solid waste landfills, waste-to-energy facilities, and recycling facilities are three major destinations for EoL LIBs⁷². LIBs treated by solid waste landfill may bring severe contaminations to groundwater through leachates, thus can pose a threat to the environment and human health⁷³. Waste-to-energy is a commonly found waste management method especially in European countries. Though, energy can be generated out of combustion, hazardous gas emissions and metal concentrated ash are inevitable drawbacks of dealing EoL LIBs within waste-to-energy facilities. To maximize the value of each LIB components out of LIB waste streams, recycling methods that are able to properly disassemble, separate, and reuse/reenergize components of LIBs have drawn much attention in both industry and academia. This section will give a general overview of the existing major recycling strategies followed by detailed pretreatment process introduction.

1.2.1 Recycling strategies overview

For the convenience of interpretation, recycling procedures are divided into pretreatment processes (PTPs) and material recovery processes (MRPs) in this dissertation as this study mainly serves the development of PTPs. Generally, there are three major types of MRPs: pyrometallurgy, hydrometallurgy, and direct recycling⁷². Each MRPs raise unique requirements to PTPs at different levels of complexity.

The primary goal of recycling LIBs is to separate and collect each components in high purity so that they can be reintroduced into the production of new LIBs or other related products. Typically, a LIB consists of around 25-30 mass% cathode, 15-30 mass% anode, 10-15 mass% electrolyte, and 3-4 mass% separator^{74,75}, among which precious metals (Lithium (Li), Cobalt (Co), and Nickel (Ni)) enriched cathode material attract the most attention for LIB recycling pioneers. Thus the pyrolysis process that is aiming at burnout LIBs as a whole and only recover valuable metals from the slag, namely pyrometallurgy process, has been widely adopted in battery recycling companies such as Umicore, Accurec, Sony, Onto and Inmetco⁷⁶. The Pyrometallurgy processes merely require module discharging as the PTP which is the simplest among the three major MRPs. The hydrometallurgy process mainly includes steps of selective leaching, solvent extraction, and precipitation^{77,78}. Thus to increase the efficiency of the MRPs, destructive mechanical crushing and sieving PTPs are commonly found in hydrometallurgy recycling plants. Recent years, as a wide variety of cathode materials have been commercialized, hydrometallurgy processes can be restricted by lacking in adaptively to different battery types and elements⁷⁹. The direct recycling method re-energizes and reuses the cathode material separated from electrodes with minimum changes to the active material's crystal morphology⁸⁰. Cathode powders collected from PTPs go through simple solid-state synthesis with additional LiOH, which also raises the complexity of PTPs since cathode electrodes are expected to be separated from other components of LIBs with their integrity well preserved⁸¹. Figure 1-4 gives a brief overview of three aforementioned strategies.

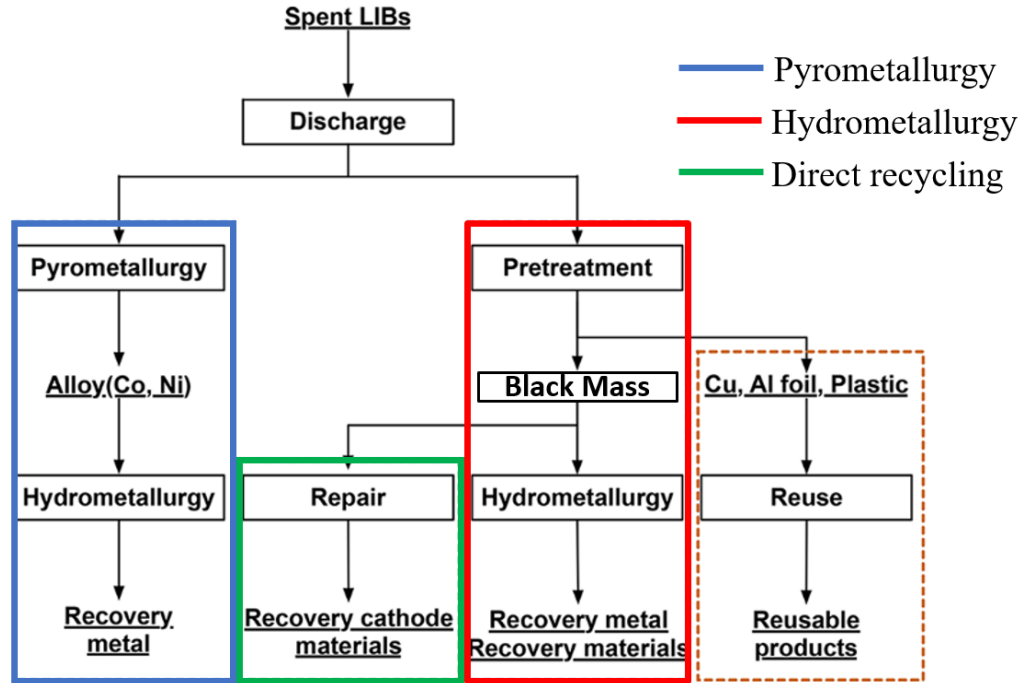


Figure 1-4 General flow sheet of EoL LIB recycling processes (modified from ⁸²)

1.2.2 Module/Pack Disassembly

Before the EV transformation in ground transporting vehicles, the majority of end-of-life LIBs came from portable electronics either in the form of individual cells or small packs. As the EV market grows rapidly, sales of electric vehicles in 2017 alone may lead to 250000 tones and half a million cubic meters of module/pack waste LIBs⁸³. Disassembling these modules/pack manually can be hazardous to human operators and time-consuming due to lacking in design for disassembly in the product design stage⁸⁴. Thus automating robotic battery module/pack disassembly systems aiming at eliminating safety risks for human workers and reducing production cost has been studied in a number of research works ⁸⁵⁻⁹⁰.

Jan Schmitt ⁸⁸ developed a robotic gripper system to rationalize the automated disassembly processes of large scale lithium ion battery packs. The hardware structure, PLC based control architecture, and the corresponding software were presented in detail. Other than

performing as a fixer and transporter of individual cells, the gripper system was also integrated with functionalities to characterize a battery cell's residual voltage and resistance which will be further used in status evaluation in the disassembly process. The gripper system was later introduced into a scenario-based disassembly system for automotive LIB systems as part of a hybrid disassembly system that can benefit the effectiveness and viability of the disassembly process⁸⁵.

Kathrin Wegener⁹⁰ proposed an EV battery module/pack disassembly sequence for recycling Audi Q5 hybrid system and introduced a KUKA robotic arm (Figure 1-5(b)) for unscrewing in a hybrid human robot workstation (Figure 1-5 (a)). The locating function of the robotic arm was investigated in two options: human demonstration and the camera-based auto detection. The human training method has been widely adopted for the robot arms in the industrial assembly tasks, which suits for situations with minimum uncertainties. As for the disassembly of a battery module, deformation or corrosion from years of service may compromise the human-robot collaboration. Previous research works⁹¹⁻⁹³ has demonstrated the success of machine vision and machine learning in assisting high-precision and flexible robotic assembly, thus Kathrin also proposed the automatic detection of bolts with machine vision system to increase the flexibility and assure the accuracy of the bolt removing process. Kathrin's research reveals the major challenge of applying robotics and automation equipment in EV battery module/pack recycling. The poorly structured operating environments caused by lacking in design standard for battery module/pack as well as the unexpected ware in years of service emphasized the importance of involving artificial intelligence (AI) for objects identification and uncertainty handling. Though automated disassembly of the wasted EV module/pack have been attempted in human-robot hybrid workstations, there is still a long way

to go before AI control algorithms and software take control of the battery module/pack disassembly tasks.

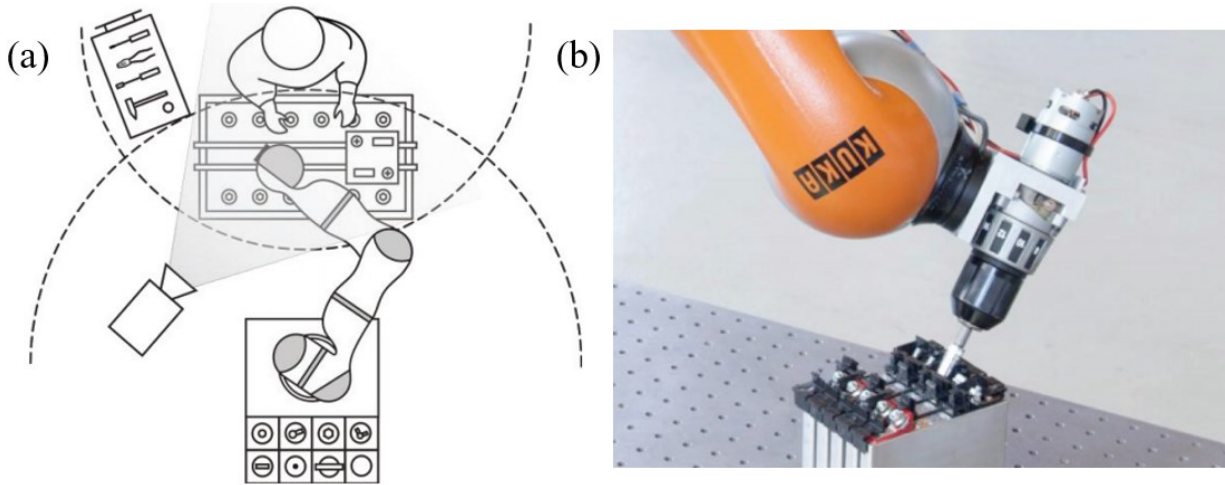


Figure 1-5 (a) Hybrid disassembly workstation and (b) Robot flange with electric screwdriver⁹⁰.

1.2.3 Material Separation

The material separation process aims at concentrating the valuable cathode components for the subsequent process. The major challenge in this step is to overcome the tight adhesion between cathode powders and Al current collector formed by PVDF binder⁹⁴. The material separation methods can be roughly categorized as destructive process or semi-destructive process depending on the integrity of the essential components introduced in section 1.1.1 after the separation. The destructive process mainly consists of steps of crushing, sieving, and classifying, which has been widely adopted in most researches and industrial production systems for further treatments of hydrometallurgical and pyrometallurgical processes^{79,95-98}. The semi-destructive process usually involves manual/semi-automated separation of the essential components (cases, electrodes, and separators), elimination of PVDF binder, and

subtraction of cathode active material. Such ‘delicate’ material separation strategy ensured the purity of the collected cathode powder which mainly benefited the uprising direct recycling strategy due to its process sensitivity to impurity metals ^{81,97}.

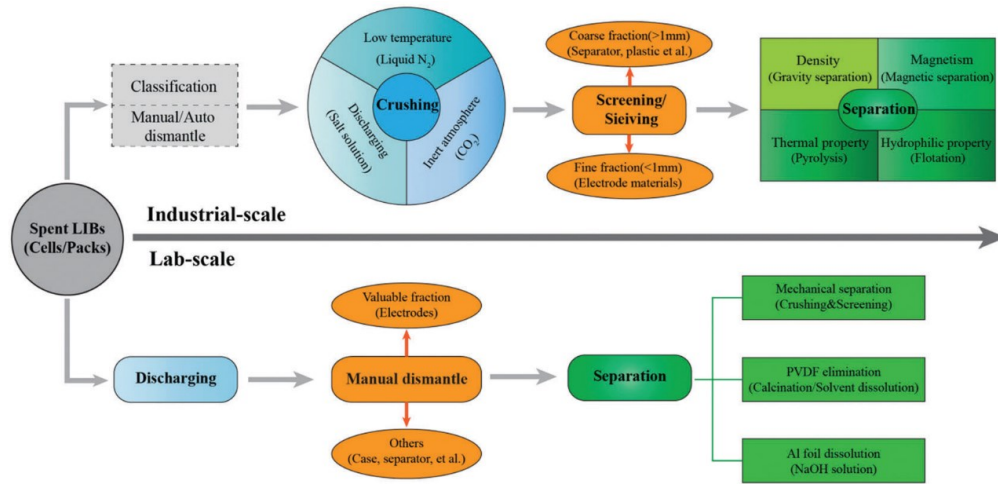
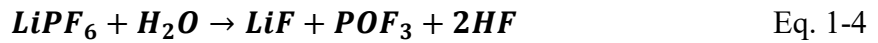


Figure 1-6 Pretreatment processes summary for recycling EoL LIBs in industrial scale and lab scale⁹⁹.

Controlling the hazard potentials during the material separation process is of vital importance to achieve truly ecological friendly recycling of retired batteries. The major hazard potentials of LIBs within the recycling process can be divided into two categories: fire/explosion hazard and chemical hazard. The contemporary applied carbonates of the electrolyte, such as dimethyl carbonate (DMC), ethyl methyl carbonate (EMC), and diethyl carbonate (DEC), are highly flammable and show flash points as low as room temperature (between 16 and 33°C)¹⁰⁰. Meanwhile, the residual energy tends to cause thermal runaway if batteries were accidentally shorted by the external circuit. The crushing step in the destructive process leads to micro-short circuiting between anode and cathode fragments and also contributes to temperature rising. Under this circumstance, LIBs can easily cause fires and

explosions with an additional oxidant ¹⁰¹. The chemical hazards are mainly toxic gaseous substances. With the presence of aerial humidity, LiPF_6 in the electrolyte decompose (Eq.1-4) and release hydrogen fluoride (HF) which can immediately convert to highly corrosive and toxic hydrofluoric acid upon contact with moisture.



Jan Diekmann ¹⁰² introduced a typical destructive material separation process as shown in Figure 1-5. The conducted mechanical process is part of the LithoRec process which combines electrical, mechanical, thermal, and, most importantly, hydrometallurgical treatments aiming at recovering nearly all valuable materials from a retired battery system ¹⁰³⁻¹⁰⁵. The process yield and separation efficiency was investigated by the process steps of first crushing, first air-classification, second crushing, sieving, and second air-classification. The discharged EV battery modules were first crushed in a rotary-shear machine with a 20 mm discharge screen. Within the zig-zag-sifting air classifier, heavy parts, such as module shells, electric conductors, and steel screws, were selectively separated from the mixed fragments according to the density. The second crushing was introduced to further decrease the fragment size so that black mass, which is a mixture of cathode active material, anode active material, and impurities, can be separated from the current collector foils and separator by a vibration sieve with a mesh size of 500 μm . Finally, a second air-classification extracted the current collector foil fragments from the valueless separator. The presented work demonstrate an industrial scalable mechanical separation strategy for retired battery modules or battery cells with a 75% material recycling rate.

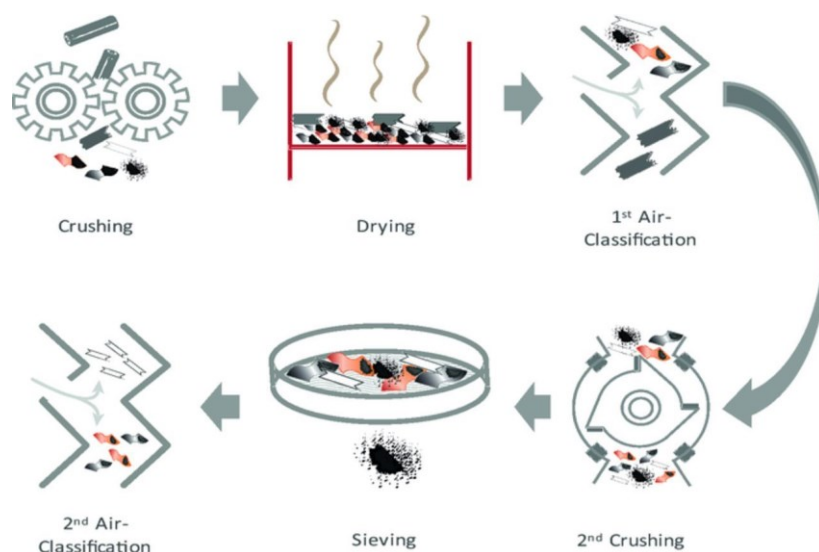


Figure 1-7 Process steps of a typical destructive material separation process¹⁰⁶.

The destructive mechanical separation process mainly relied on brutal force and density or magnetism difference of the components to assure the separation efficiency. Thanks to its high automation potential, such processes have been widely combined with hydrometallurgical processes. Meanwhile, the semi-destructive process that aims at breaking adhesion between active powders and current collector foils by dissolving the binder in a solvent¹⁰⁷⁻¹⁰⁹ or decomposing the binder^{97 110} under high temperatures has also caught attention in the lab scale research.

The binder dissolving method was first adopted by Contestabile M¹⁰⁷ who treated the crushed battery mix with NMP at 100°C for 1 h to separate LiCoO₂ from the support aluminum current collector. Soon after, the method of applying ultrasonic energy to facilitate the solvent separation of cathode active material and aluminum current collector was introduced by Jinhui Li¹¹¹. Such mechanical (ultrasonic)-chemical (organic solvent) combined method was widely adopted ever since¹¹²⁻¹¹⁴. The more detailed relationship between process parameters and the separation efficiency of the ultrasonic enhanced binder dissolving process was first studied by

Song X¹¹⁵ in 2017. Process parameters such as temperature, sonication time, solid-to-liquid ratio, and solvent type were studied by controlling a single variable at a time. The result indicated that temperature and sonication time have little impact on the separation efficiency of the selected spend LiFePO₄ LIBs and smaller solid-to-liquid ratio facilitates the coating separation. Meanwhile, in order to reduce the cost and pollution, C M Toma¹¹⁶ introduced acetic acid as the ultrasonic medium to replace organic solvent and the optimal value of molar concentration of acetic acid for coating separation was studied by the single variable controlling approach as well.

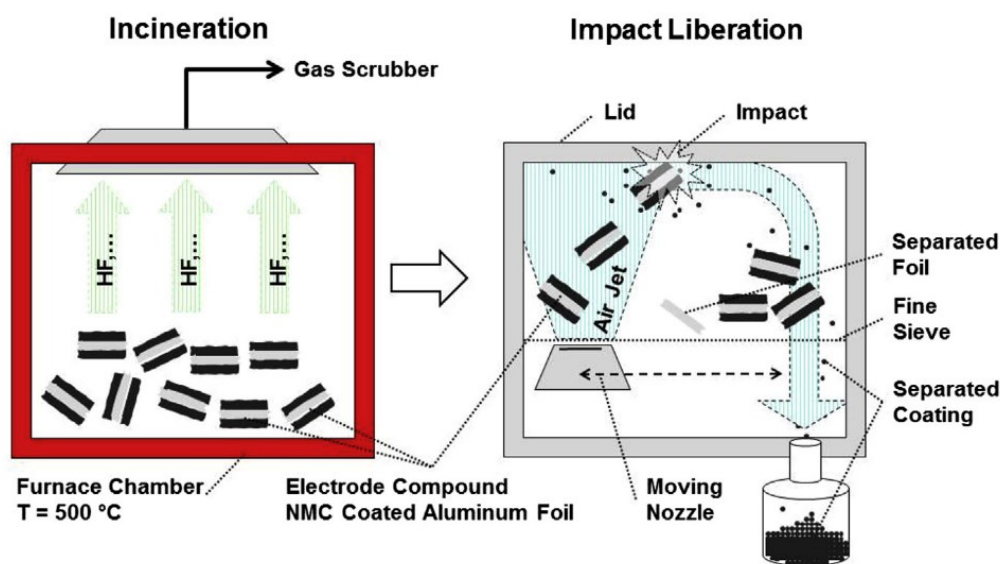


Figure 1-8 Experimental set-up for the ANVIL process⁹⁷.

The binder decomposing method takes the advantage of the lower decomposition temperature of the PVDF compared to graphite, carbon black, aluminum foils, and copper foils. Therefore, a heating step in the material separation process can be both convenient and effective to eliminate the adhesion. Based on this fact, Christian Hanisch⁹⁷ proposed the adhesion

neutralization via incineration and impact liberation (ANVILL) approach as shown in Figure 1-8. A high temperature of 500°C was adopted in the furnace chamber for PVDF decomposition. The newly designed air-jet separator then separated the coating powder and the current collector foils by lifting the electrodes towards the top lib with a high-speed air to create the impact stress on foils and agglomerates. The separated coating powder can then pass through the fine sieve with a mesh size of 50 µm and get collected for the follow-up procedures. The ANVILL approach was evaluated using $\text{LiCo}_{0.33}\text{Ni}_{0.33}\text{Mn}_{0.33}\text{O}_2$ cathode electrodes and the results compared to a destructive separation process indicate a higher yield and a significantly higher purity.

1.3 State-of-the-Art Material Recovery Process in EoL LIB Recycling

1.3.1 Pyrometallurgical Processes

The pyrometallurgical process usually uses a high-temperature furnace to decompose the metal oxides in a reducing atmosphere. There are three types of products generated from the pyrometallurgical process: metallic alloy, slag, and gases. The alloy, consisting of Co, Ni, Fe, and Cu, is the reduction product of the metal oxides from the cathode electrodes^{117,118}. The different elements in the alloy can be selectively extracted and reused through hydrometallurgical or bioleaching in the follow-up processes. The slag typically contains aluminum, manganese, and lithium^{119,120}, which can be used as construction materials such as cement¹²⁰. Gaseous products are produced from the electrolyte and binder decomposition at low temperature (<150°C) as well as burn off of the polymers at high temperature.

Without the need for module disassembly, pretreatment process, and passivation process, the furnace is able to handle individual LIBs from portable electronics or even LIB modules from EVs, which makes a great contribution for simplifying operations and reducing

production costs on a large-scale. In addition, the overall safety risk of the pyrometallurgical process is little since individual LIBs or LIB modules are treated in the extreme temperatures surrounded by the reducing atmosphere. However, the drawbacks of the pyrometallurgical process are equally obvious as its advantages. The energy consumption is extremely high due to high temperature operation. Even though the burning of the electrolytes and plastics (40-50% of the battery weight) compensate for energy consumption, extra instruments are needed to control toxic gases such as HF and CO generated from this process. Organic electrolytes, binders, lithium, and manganese are either burned off or trapped in the slag, thus unable to be reused for battery manufacturing. Despite the aforementioned disadvantages, the pyrometallurgical process still remains a frequently adopted approach in industries for its operation simplicity, safety, and high-yield for transition metals such as Co and Ni^{76,82}.

1.3.2 Hydrometallurgical Processes

The hydrometallurgical process consists of two major steps: leaching and extraction. Unlike the pyrometallurgical process, hydrometallurgical processes could not directly treat individual LIBs or LIB modules. Instead, the input of hydrometallurgical processes have to be either the smelting slag produced by the pyrometallurgical process¹²¹ or the black mass produced by material separation processes introduced in section 1.2.3. Compared to the pyrometallurgical process, the hydrometallurgical process holds many advantages such as higher metal recovery efficiency, lower energy consumption, minimal gas emission, and lower capital cost¹²²⁻¹²⁴. Thus, hydrometallurgical processes are better at recycling EoL LIBs on an industrial-scale in favor of both cost and environment.

Figure 1-9 shows a complete material flow of a hydrometallurgical process, which mainly included steps of passivation, material separation, leaching, extraction, and

remanufacture. What's worth mentioning in the material separation step is the application of the alkaline leaching method, which can be considered as a special semi-destructive material separation process. The manually extracted cathode electrodes were soaked in sodium hydroxide (NaOH) to dissolve Al current collector foils (see Eq.1-5). After water washing and filtration, cathode active could be effectively extracted ¹²⁵. The high-temperature calcination process was then needed to burn off the PVDF binders to further eliminate the adhesion between cathode powders.

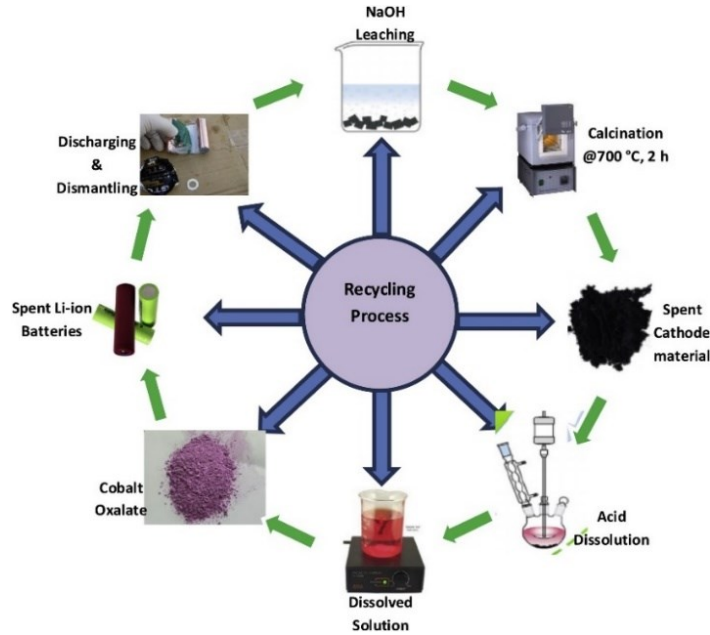
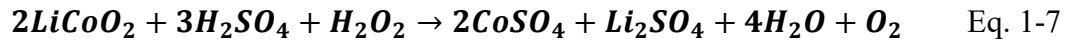
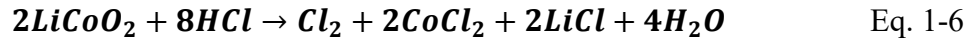


Figure 1-9 Flow sheet for a typical hydrometallurgical process of LiCoO₂ from spent LIB¹²⁶.

The leaching step is the major step for recovering valuable metals in the hydrometallurgical process. It converts the metals in spent cathode powders from solid state into solutions for further purification and separation processes by using inorganic acid, organic acid, alkali or bacteria solution. Several inorganic acids such as sulfuric acid (H₂SO₄)^{76,127-130}, hydrochloric acid (HCl)^{111,131-133}, and nitric acid (HNO₃)¹³⁴⁻¹³⁷ are commonly used as leaching

agents, among which HCl alone proved to have the best leaching efficiency. However, the oxidation of HCl would produce Cl_2 (see Eq. 1-6), which increased recycling cost due to the need of both antisepticising equipment and emission treatment equipment in the recycling plants. A reducing agent, such as hydrogen peroxide (H_2O_2)^{112,128,136,138}, sodium hydrogen sulfite ($NaHSO_3$)¹³⁹, or glucose ($C_6H_{12}O_6$)¹⁴⁰, was usually required for using H_2SO_4 or HNO_3 as leaching agent. Among all combinations of possible leaching acids and reducing agents studied^{111,141-143}, the most common combination by far is H_2SO_4/H_2O_2 ¹⁴⁴. The reducing agent H_2O_2 is able to convert transition metals contained in the black mass to their divalent states in order to gain better solubility in acid solutions. Thus the leaching of $LiCoO_2$ by H_2SO_4/H_2O_2 is able to convert the insoluble Co (III) into soluble Co (II) through reaction as shown in Eq. 1-7.



Although inorganic acids proved to have very high efficiencies in cathode active material leaching, especially Li (>99%) compared to pyrometallurgical processes, the considerable secondary pollutions limited the industrial application of inorganic acids. On the one hand, hazardous gas emissions such as Cl_2 , SO_3 , and NO_x are common products in the inorganic acid leaching process, which posed a threat to both environment and human operators. On the other hand, the waste acid solutions from the inorganic leaching process must be neutralized by NaOH or treated by other approaches before emission. Extra expenditure will be needed for further disposal of waste emissions if inorganic acids were used as leaching agents. Thus organic acid leaching has caught much attention in recent years for their greener practices. Some organic acids such as citric acid ($C_6H_8O_7$)¹⁴⁵ and oxalic acid ($C_2H_3O_4$)¹⁴⁶, showed great potential in LIB cathode material due to their recyclability, minimum secondary pollution, and

easy degradation properties. Weak acidity of organic acids and relatively slower reaction speed restricted the industrial application of such approach.

The dissolved solution after the leaching process contained valuable metals include Li, Co, Ni, Mn, Cu, and Al. The second essential step of the hydrometallurgical process is to selectively extract these metals out of the solution in ways of solvent extraction, chemical precipitation, or electrochemical deposition. Because of the complexity of the solution, two or more methods were commonly combined to separate metals from the solution^{82,96}.

Solvent extraction approach was widely adopted in hydrometallurgy processes and proved to be highly effective for different metal ions. Extractants including diethylhexyl phosphoric acid (DEHPA), di(2-ethylhexyl) phosphoric acid (D2EHPA), bis(2,4,4-trimethylpentyl) phosphinic acid (Cyanex 272), 2-ethylhexyl phosphoric acid mono-2-ethylhexyl ester (PC-88A), and diethylhexyl phosphoric acid (DEHPA) were used to separate metals from leaching solutions^{120,122,147}. Chemical precipitation approach was commonly combined with solvent extraction approach to gain a higher separation efficiency. The existence of anions such as $\text{C}_2\text{O}_4^{2-}$ from oxalic acid ($\text{H}_2\text{C}_2\text{O}_4$), PO_4^{3-} from phosphoric acid (H_3PO_4), OH^- from NaOH or ammonium hydroxide (NH_4OH), and CO_3^{2-} from sodium carbonate (Na_2CO_3) may combine with the valuable metals in the leaching solution and form precipitates¹⁴⁸⁻¹⁵².

Although destructive material separation processes were most commonly adopted pretreatment strategy for hydrometallurgical processes, the black mass containing both anode and cathode materials would complicate the follow-up processes. Thus, the semi-destructive material separation processes that separate anodes and cathodes prior to material segregation would greatly benefit the final yield and expenditure. Nevertheless, lacking in universal design standards for individual LIBs and LIB modules made it extremely difficult to achieve

automated pre-sorting of anodes and cathodes in large-scale production. Thus neither pyrometallurgical process nor hydrometallurgical process could provide a pure and simplified material stream to fulfil the closed-loop battery manufacturing.

1.3.3 Direct Recycling Processes

Both pyrometallurgical and hydrometallurgical processes aimed at producing pure metal as their final product, thus the compounds of cathode materials were first broken down to element level before being selectively extracted from the mixture. However, the lithium deficient cathode active powders can be reincorporated into new cathode product with the presence of Lithium sources (lithium hydroxide (LiOH) or lithium carbonate (LiCO_3)) through a simple thermal treatment^{81,115,153-155}, thus minimum crystal morphology changes of metal oxides are expected. This step was usually named regeneration or re-litigation while the process adopted this step was categorized to direct recycling process. Within the step, lithium sources would compensate the lithium loss of the cathode material caused by SEI layer formation, material degradation, and insufficient discharging (over discharging may lead to copper contamination on cathode electrodes).

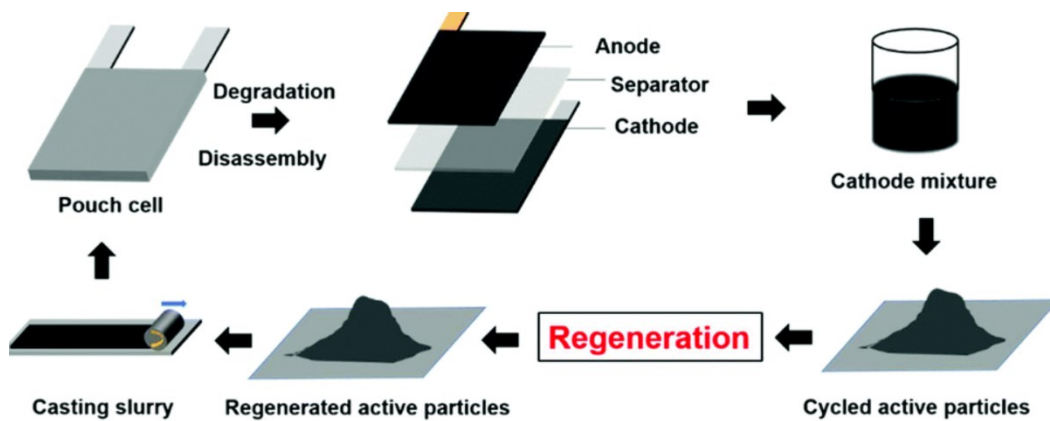


Figure 1- 10 Material flow of the direct recycling process¹⁵⁶.

A simplified material flow of the direct recycling process is shown in Figure 1- 10. Cathode electrodes need to be extracted as a whole within the pretreatment process to avoid cross contamination with other material, especially copper foil. The adhesion between Al current collector foil and cathode coating could be eliminated by either dissolving Al in NaOH solution or eliminating the PVDF binders. The recycled active powders such as LCO could then get “repaired” by LiOH under high-temperature calcination as show in Eq. 1- 8 where x is equal to the average percentage of lithium losses in cycled material. The direct recycling processes could directly produce high-value new cathode powder out of recycled black mass, which avoided complexed leaching and separation processes. Thus, this approach had great potential in decreasing the production cost as well as total energy consumption for the LIB cathode material production cycle^{157,158}. Meanwhile, all components of LIBs (except separators) could potentially be recycled and reused if treated by this approach (See Figure 1- 11), which further increased the economic return in industrial application.

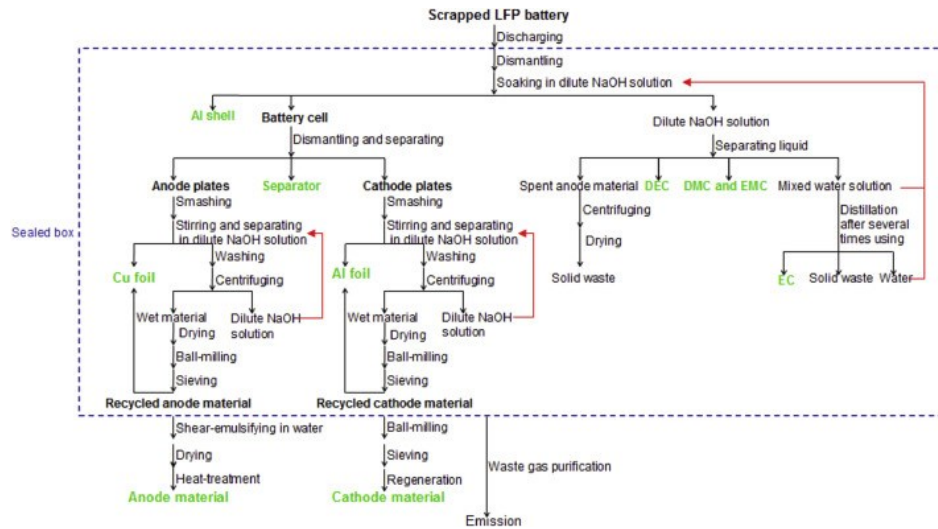
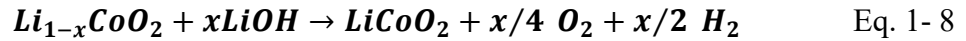


Figure 1- 11 Direct regeneration process flow diagram of cathode material mixture⁸¹.

Nevertheless, huge obstacles prevent the practical application of the direct recycling processes in recycling plants, for the drawbacks of direct recycling process were as obvious as its advantages mentioned above. Firstly, directly repairing cycled cathode material put forward a much higher requirement to pretreatment processes, especially automated module disassembly and cathode electrode extraction. Previous research mainly focused on industrial application of the destructive material separation process^{94,159} and automation potential of LIB module disassembly¹⁶⁰⁻¹⁶². How to effectively achieve semi-destructive cathode electrode extraction within an automated production environment remained a blank. Secondly, simple solid-state calcination process suited cathode materials with simple composition (LCO and LFP). For cathode materials consists of multiple metal oxides like NCM and NCA, sol-gel method or co-precipitation were needed to resynthesize cathode materials¹⁶³. The lithium deficiency would be compensated into a molecularly homogeneous level in solutions instead of solid-phase from these two approaches. Thus, precision presorting of individual batteries according to material type prior to pretreatment process was required especially for EoL LIBs from portable electronics^{164,165}. Thirdly, the success of regeneration step was extremely sensitive to metal impurities in cycled cathode coating material. The existence of fine Al or Cu particles would compromise the electrochemical performance of the regenerated cathode powder. Thus, apart from resynthesized cathodes, other high-value-added products consisting of transition metals utilized in LIBs have also been widely studied^{141,166-171}.

1.3.4 Comparison of Three Major LIB Recycling Methods

Although the advantages and disadvantages of three major LIB recycling methods have been mentioned above correspondingly, it is still beneficial to compare their technology readiness in a more intuitive way as shown in Figure 1-12. Pyrometallurgical process is by far

the most mature recycling strategy for practical application. The capability of smelting large amounts of individual LIBs and LIB modules without involving any pretreatment process for material separation significantly decreases the process complexity and production cost. However, obvious drawbacks such as high energy consumption, severe second waste generation, low yield, and lacking in lithium recovery ability urged both recycling industries and researchers to search for its replacement with equal simplicity and productivity. Hydrometallurgical processes hold the intermediate position of all three approaches in almost every aspect. It has shown great potential in decreasing secondary waste generation and maximizing recycling rate of Co and Ni while keeping the process complexity at a reasonable level. Thus the hydrometallurgical process will most likely dominate the recycling industries in the foreseeable future. Meanwhile, the direct recycling process is prevailing in a wide range of lab-scale researches and barely started industrial application. The highest material recovery rate and lowest secondary waste generation makes it the seemingly the most profitable recycling process. Nevertheless, lacking in the design standard of individual LIB and LIB modules and sensitivity to metal contamination weakened its attraction to large-scale production where automation could not be emphasized more.

Comparison of different LiB recycling methods								
Best ***** **** *** ** * Worst								
	Technology readiness	Complexity	Quality of recovered material	Quantity of recovered material	Waste generation	Energy usage	Capital cost	Production cost
Pyrometallurgy	*****	*****	*	***	**	*	*	*****
Hydrometallurgy	****	***	***	****	***	***	***	***
Direct recycling	**	*	**	*****	****	***	***	*

	Presorting of batteries required	Cathode morphology preserved	Material suitable for direct re-use	Cobalt recovered	Nickel recovered	Copper recovered	Manganese recovered	Aluminium recovered	Lithium recovered
Pyrometallurgy	*****	No	No	*****	*****	*****	**	No	*
Hydrometallurgy	****	No	No	*****	*****	****	***	*****	***
Direct recycling	*	*****	****	*****	*****	*****	*****	*****	*****

Figure 1- 12 Comparison of different LIB recycling methods⁸³.

As important energy storage devices, LIBs play a more important role in solving energy and environmental issues than ever before. Consequently, the LIB production volume rapidly increases year by year. With limited service time, massive amounts of LIBs need to be properly treated at their EoL. However, rapid iteration of the cathode materials and lack of structure design standards have posed huge pressure to the recycling end of the full product cycle. Although there is little hope to find a certain recycling process that can treat all types of LIBs with different elements and configurations simultaneously in a profitable way, substantial efforts from research lab and related LIB manufactures are expected to treat as many LIBs as possible at their end-of-life state not only for maximizing the commercial profit but also for eliminating severe environmental hazards that EoL LIBs might lead to.

1.4 Outline of this Dissertation

This dissertation focuses on the semi-destructive pretreatment process development that serves the direct recycling strategy. To make up the blank of material separation method for large-scale direct recycling of LIB cells as introduced in section 1.2, the concept of an automated disassembly system for the individual LIB cells is designed, prototyped, and investigated for the first time. The following cathode coating extraction process is developed and improved on both lab-scale and intermediate-scale production with the help of a series of carefully designed experiments. The central line of our effort is to develop a systematic approach to enhance the adaptively of the direct recycling process toward the large-scale production. The goal of this research work is to facilitate the industrial application of the direct recycling strategy since it has the great potential to become the most eco-friendly and economically beneficial approach by far as introduced in section 1.3. The detailed structure of this dissertation is as follows.

Chapter 2 introduces the design and prototype of an automated disassembly system aiming at separating cell case, metal tab, cathode electrodes, anode electrodes, and separators of a LIB pouch cell with minimum human intervention. The disassembly sequence plan indicates that the entire disassembly line to be divided into three modules connected with conveyors. The prototyped modular disassembly system was then testified by manually assembled dummy pouch cells.

Chapter 3 takes a step forward and focuses on cathode coating material separation of cathode electrodes utilizing organic solvent approach. High power LCO battery packs are selected as research subjects. General process input operating parameters are first differentiated by Plackett-Burman parameter screening experiments. The parameters proved to be significant to final yield are then studied in detail by Taguchi experiments to generate a regression model for yield prediction under different input parameter combinations.

Chapter 4 studies the cathode coating material separation process of cathode electrodes from LFP cylindrical secondary batteries. The organic solvent soaking process is able to completely separate the coating materials and the Al current collector foil without involving any mechanical energy assistance. Theoretically, this innovative approach is able to achieve a 100% pure cathode coating material recollection. The process yield is studied by full-factorial experiments in order to provide guidance for process parameters selection for further lab-scale or even industrial scale production.

Chapter 5 initiates the regeneration study of EoL LFP cathode coating reclaimed from Chapter 4. The property of the EoL LFP is first characterized by Inductively Coupled Plasma Atomic Emission Spectrometer (ICP-AES), X-ray Diffraction Spectrometry (XRD) and Scanning Electron Microscopy (SEM). The electrochemical performance of samples

regenerated under various sintering conditions are then conducted to identify the optimum process parameters.

Chapter 6 summarizes the major contributions of this dissertation. Possible future developments are also enclosed.

Chapter 2 Disassembly Automation for Pouch Cells

As governments have begun to set timetables for banning the production of internal combustion engine vehicles globally, the estimated annual demand for lithium-ion batteries (LIBs) from electric vehicles (EVs) in 2025 reaches 408GWh, while this number was merely 20GWh in 2016.¹⁷² Previous studies on cycling performance degradation of battery packs in hybrid electric vehicles (HEVs) indicate a battery pack lifetime of only 4.5 to 14.5 years depending on their operating conditions.^{173,174} The rapid growth of discarded LIB packs from HEVs and EVs along with an increasing number of end-of-life LIBs generated by portable electronics and energy storage plants will cause severe environmental and safety problems if not treated properly.⁸² Meanwhile, the end-of-life LIBs is a potential resource of valuable metals (e.g. Ni, Mn, Li or Co) while pressures have been imposed on the supply chain of these materials already.¹⁷⁵ Therefore, it is of vital importance to develop recycling methodologies that are ecologically friendly and economically feasible for end-of-life LIBs in present time and future.

The state-of-the-art of end-of-life LIB recycling methods mainly combines mechanical pretreatments and metallurgy processes.¹⁴⁴ Mechanical pretreatments comprises steps of discharging battery packs, dismantling packs into cells, and separating materials of single cells. Metallurgy processes that consist of pyro-, hydro-, bio-metallurgy are generally downstream procedures of mechanical pretreatments.⁸² Despite the dominating role of metallurgical processes in the industry, their hazardous gas emissions, acid waste, and high energy consumption issues have always been barriers toward a truly sustainable closed-loop recycling.¹⁷⁶ In recent years, a direct regeneration approach that resynthesizes recycled cathode powder with heat treatment proves to be feasible in lab scale research.^{81,115,177} Although such

approach claims to be more ecologically friendly and energy conserving, it also brings up much higher requirement to the material separation technique toward mass production.

Material separation step, the most critical process in mechanical pretreatments, mainly refers to multi-level crushing, sorting, and sieving techniques in the industry because of their high automation potential. The total coating material recovery rate following this destructive crushing strategy is only 75% even in lab scale research.¹⁰² However, if electrode sheets can be separated and extracted with their integrity well preserved, the coating material recovery rate reaches as high as 97.4% utilizing an ANVIL process.⁹⁷ Meanwhile, the black mass yielded from the destructive crushing strategy is a mixture of anode coating, cathode coating, and metal impurities. For metallurgical processes that mostly break down the compound of cathode active materials, metals can be recycled or discarded by the following melting or leaching processes. Nevertheless, for direct regeneration processes, the existence of anode powders and mixed metals in cathode powder increases the complexity of downstream recycling processes and may even decrease the electrochemical performance of the final product.¹⁷⁸

Hence, an automatic disassembly system is designed and prototyped specifically for dismantling and separating cathode sheets, anode sheets, separators, and Al laminated film housing from lithium-ion pouch cells in this paper. Compared to the destructive crushing strategy that has been widely adopted in industry, this proposed system has a great potential to achieve higher coating material recovery rate as well as yield purer cathode powder for mechanical pretreatment processes in mass production. The material separation strategy and mechanism design of this project are patented within¹⁷⁹.

2.1 Disassembly Sequence Planning

Disassembly sequence planning (DSP) is always the first step of any EoL product recycling processes. Just as the solutions of a product assembly problem may not be exclusive, one can disassemble a product with multiple choices of precedence on particular parts and components. A better-designed DSP benefits the disassembly efficiency as well as the expenditure, thus helps with making actual profits out of the recycling activities which is the practical problem that most recycling researches and enterprises are struggling on. The DSP for individual LIBs are divided into three steps: disassembly mode (DM) selection, disassembly precedence (DP) confirmation, and disassembly objective planning. In the mode selection step, the suitable disassembly mode needs to be selected based on detailed target structures and requests of subsequent processes. Then, the disassembly precedence relationships between each components are confirmed by the disassembly matrix and the disassembly precedence graph. Finally, a rough modular allocation of disassembly objectives are determined prior to detailed mechanism design.

2.1.1 Disassembly Mode Selection

Choosing a proper DM is the first step of starting the recycling of a product at its EoL. Generally, there are two categories of DMs on which decisions have to be made: complete/fractional disassembly and sequential/parallel disassembly. The complete disassembly usually takes apart the assembly into the fundamental compositions, thus each component can be properly reused or recycled. The fractional disassembly only targets the high-value added parts of the assembly and the complexity of the total disassembly process as well as the total cost can be minimized compared to the complete disassembly. As for the sequential disassembly, components are disconnected with the main assembly one after another. On the

contrary, the parallel disassembly removes multiple parts within one step, which is usually applied to assemblies with relatively more parts and easy-to-access connections.

Before selecting disassembly mode, designers need to have a thorough understanding of the shape and internal structure of the target EoL LIB. The shape of lithium-ion secondary cells can be divided into three main groups: cylindrical, pouch, and prismatic. Their differences in housing material and ESC design lead to certain advantages and disadvantages in manufacturing processes and applications. Relatively low production cost and highly simplified packaging processes allow pouch cells being extensively deployed on EVs and portable electronics.

The typical internal structure of pouch LIBs is an ESC sealed by stamped Al laminated film (Figure 2-1). Anodes and cathodes are alternately stacked and electrically isolated by the separator to form the ESC. Depending on the continuity of electrode sheets and the separator, ESCs are classified into three styles: single sheet stacking, winding, and Z-folding. The single sheet stacking style is commonly used in laboratory cell assembly while the winding style proved to be the most productive design in industrial applications due to its continuous electrodes and separators feeding strategy. In recent years, efforts to decrease the cycle time of Z-folding process utilizing robots and customized mechanisms have been carried out,^{39,180} which result in its rapid technology transition to mass production scale. Meanwhile, Z-folded ESCs with discrete electrodes and continuous separators require more complicated mechanisms to disassemble than the other two types. Thus, this dissertation mainly focuses on the recycling of end-of-life pouch LIBs with z-folded ESCs.

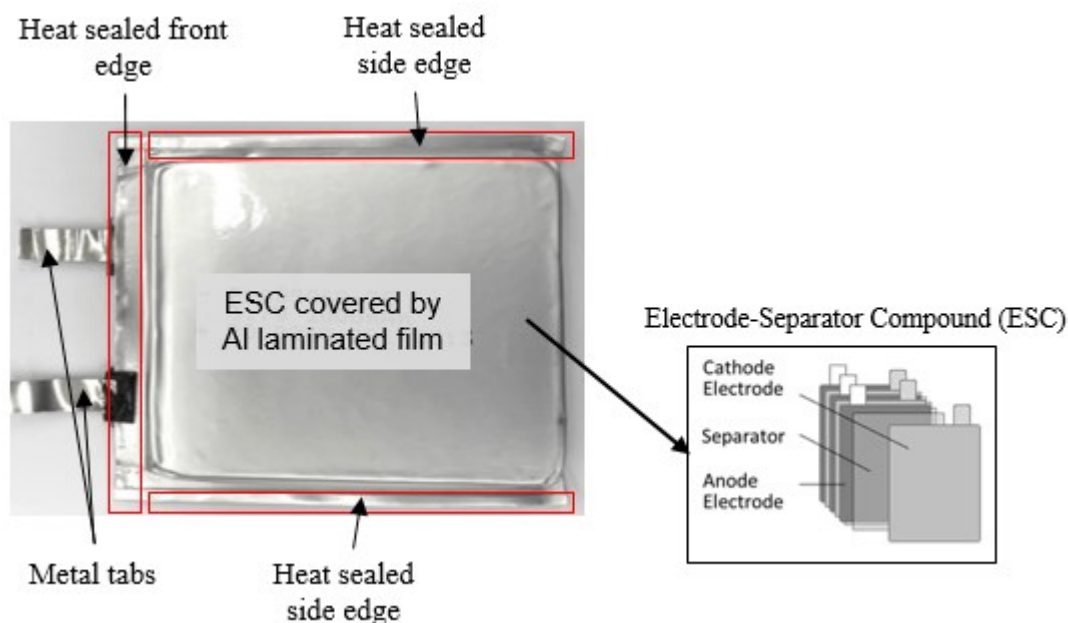


Figure 2-1 Configuration of the H605060 lithium-ion polymer rechargeable battery manufactured by MTI Corporation.

Based on aforementioned requirements, H605060 lithium-ion polymer rechargeable batteries manufactured by MTI Corporation are chosen as the study subject for the research work shown in this chapter. These cells have a nominal capacity of 2000 mAh at 300th cycle with 0.2C discharge rate. The C-rate measures the rate that a battery is discharged according to its maximum capacity. A 0.2C rate means that the discharge current can discharge the fully-charged battery in 5 hour. Thus, for the H605060 LIB with a capacity of 2000 mAh, 0.2C requires a discharge current of 400 mA. The concept of the C-rate will be repeatedly mentioned throughout this dissertation, particularly within Chapter 5. The outer dimensions of the H605060 LIB are: 5.8 ± 0.5 mm (Thickness) , 50.0 ± 0.5 mm (Width) , and 60.0 ± 0.5 mm (Length) as shown in Figure 2-2. The customized fixtures, transporters, and end-effectors are designed to accommodate the dimensions and the clearance of the H605060 LIB.

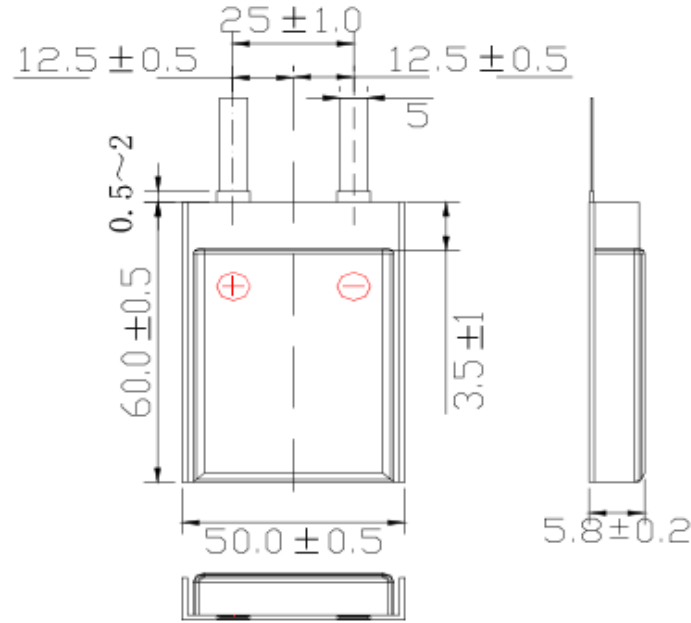


Figure 2-2 Detailed 2D specification of the H605060 lithium-ion polymer rechargeable batteries from MTI Corporation.

From Figure 2-1, it is clear that both side edges of the Al laminated film are folded tightly towards the center and the heat sealing of the Al laminated film is irreversible. Certain part of the Al Laminated film need to be cut off from the main body to reveal the ESC sealed inside of it. Meanwhile two metal tabs on the positive and negative terminal are welded together with all cathode electrodes and anode electrodes correspondingly by resistance welding machines or ultrasonic welding machines. It is both not practical to unweld the metal tabs and not profitable to spend extra expenditure on equipment and processes to recycle two metal strips. Thus the concept of the fractional disassembly is applied to the disassembly of the H605060 LIB. As for the second category of the disassembly mode, parallel disassembly is not necessary for H605060 individual LIB because of the relatively simple internal structure and the small part number. Such disassembly mode can be extremely helpful in LIB module disassembly where large amounts of subassemblies and connectors are involved and the operating space is

sufficient for multiple end-effectors to work simultaneously. Thus the components of H605060 LIB are to be removed sequentially in the order of Al laminated case and the ESC.

2.1.2 Disassembly Precedence (DP) Confirmation

After determining the DM as partial disassembly and sequential disassembly, the DP has to be confirmed by developing disassembly models. A proper DP helps the developer to better understand the inter connection between parts and components and make decisions on disassembly sequence accordingly. Two most commonly utilized tools in disassembly model development are the disassembly matrix and the disassembly precedence graph, which will be applied to H605060 LIB disassembly in this section.

A complete disassembly matrix describes the interference between each component in the direction of the x, y, and z-axes within a 3D space independently, which is commonly adopted in complete disassembly mode since all connections have to be properly removed so that each component can be isolated. Here, we have chosen to adopt the partial disassembly mode according to aforementioned reasons, thus a unified disassembly matrix is developed regardless of the direction of the interference between components. Within a disassembly matrix, if the component A in the i_{th} row does not have any connections with the component B in the j_{th} column, the A can be removed from B freely. Meanwhile, B can also be removed from A without any constraints. If this is the case, the location (i, j) in the disassembly matrix will be marked as 0. On the contrary, if external forces are required to separate certain components, then the corresponding location in the disassembly matrix will be marked as 1.

		1	2	3	4	5	6
		Cathodes	Anodes	Separator	Al laminated film	Positive metal tab	Negative metal tab
1	Cathodes	1					
2	Anodes	0	1				
3	Separator	1	1	1			
4	Al laminated film	1	1	1	1		
5	Positive metal tab	1	0	0	1	0	
6	Negative metal tab	0	1	0	1	0	0

Figure 2-3 Disassembly matrix of Z-folded pouch cells.

To better illustrate the property of the connections, a 3-axes space is defined for the H605060 LIB. Assume the width (50.0 ± 0.5 mm) of the H605060 LIB is the x-axis, the length (60.0 ± 0.5 mm) is the y-axis, and the thickness (5.8 ± 0.5 mm) is the z-axis. The Al current collector foil tabs on cathode electrodes are welded together onto the positive metal tab along the z-axis to form a unified positive terminal for all cathode electrode sheets. Thus location (1, 1) and (5, 1) in the disassembly matrix as shown in Figure 2-3 are marked as 1. Similarly, Cu current collector foil tabs on anode electrodes are welded onto the negative metal tab along the z-axis as well, which marks location (2, 2) and (6, 2) as 1. The separator is the most complicated component to define and remove connections in H605060 LIB. It is Z-folded by itself, thus restricting its own free movement along the z-axis. As cathode electrodes and anode electrodes are alternatively inserted into the folded structure of the separator, their mobility in the x-axis is restricted unless the separator is unfolded. Hence, location (3, 1), (3,

2), and (3, 3) are marked as 1. The Al laminated film is a critical component for successful pouch cell sealing and packaging processes. It consists of Nylon (ON) outer layer, Al middle layer, polypropylene (CPP) inner layer, and two binding layers in-between them. The fantastic stamping formability allows the Al laminated film to perfectly accommodate different sizes of the ESCs. The stamped Al laminated housing not only provides protection to ESCs but also restricts the mobility of all components of ESCs in the x-y plane, thus location (4, 1), (4, 2), and (4, 3) are marked as 1. Meanwhile, the CPP inner layer, acting as the heating sealing layer, seals two side edges and the top edges of H605060 LIB when two contacting CPP inner layers are pressed by the heating bar along z-axis, thus location (4, 4) is marked as 1. As for the positive metal tab, it is welded with the Al current collector foil of every single cathode electrode, thus location (5, 1) is marked as 1. The top edge of the H605060 LIB also seals positive metal tabs with the assistance of the hot melt adhesive polymer tape that came with the metal tabs. Thus, location (5, 4) is marked as 1. Same connections and restrictions apply to negative metal tabs as well hence location (6, 2) and (6, 4) are also marked as 1. So far, all existing position restrictions caused by connection have been identified and recorded in the simplified DM as shown in Figure 2-3. The next step is to generate the DP graph to eliminate or remove all connections marked in DM by properly allocate them in DP.

Partial disassembly mode enables us to bypass complex steps of the traditional DP generation process and make parts or components removal decisions with more freedom especially when the integrity of some components do not need to be preserved. Here, the designed material flow is presented in the tree graph as shown in Figure 2- 4. The original EoL H605060 LIB is placed at the very top of the precedence graph as a whole. Branches stretch out from assemblies or sub-assemblies at higher level and point to the isolated parts/components or

subassemblies at the next level. Prior to the exposure of the ESC, the connections that seal the ESC inside the stamped Al laminated film housing need to be removed. As discussed in section 2.2.1, it is neither practical nor profitable to open up three sealed edges and unweld the metal tab. Thus the first step is to trim them off from the main body of the H605060 LIB and leave the Al film housing covered ESC as the subassembly for the next level. The trimming line of the side edges will be located between edges of the Al film housing covered ESC and the sealing strip, thus connection (4, 4) in the disassembly matrix can be removed within this step. The trimming line of the top edge will be located between the welding point on the metal tab and the Al/Cu current collector foils that are covered by active material coating. That says the uncoated tabs on the Al/Cu current collector foils will be trimmed as well as the unsealed part of the double layered Al laminated films same as the side edges. Hence, the connections held by the welding point between cathode electrodes and similar connections held between anode electrodes are eliminated including the connection between Al laminated films formed by heat sealing. Meanwhile, since the metal tabs are abandoned along with the front edge, all connections related to metal tabs are eliminated during the front edge trimming. Thus the front edge trimming will remove connection (1, 1), (2, 2), (5, 1), (5, 4), (6, 2), and (6, 4). The Al film housing covered ESC will be further taken apart in the next step to completely free the ESC from the constraint of Al laminated films. The housing will be opened and exposed ESC can be extracted for key material separation step, which result in elimination of connections (4, 1), (4, 2), and (4, 3) in x-y plane. Finally the z-folded separator of the ESC subassembly will be stretched into a continuous strip, so that cathode electrodes and anode electrodes attached to the opposite sides of the separator can be collected by two sets of customized end-effectors. Thus in this level, position restriction applied to cathode electrodes and anode electrodes from the

separator are eliminated. Along with the stretching of the separator, connection (4, 1), (4, 2), and (4, 3) are removed from the disassembly matrix. At this point, the major functionality of the automated disassembly system has been identified and defined for each precedence level and all connections existing in the disassembly matrix have been properly allocated in the disassembly precedence graph. Further separation of active material from the cathode electrodes will be covered in Chapter 3 and Chapter 4.

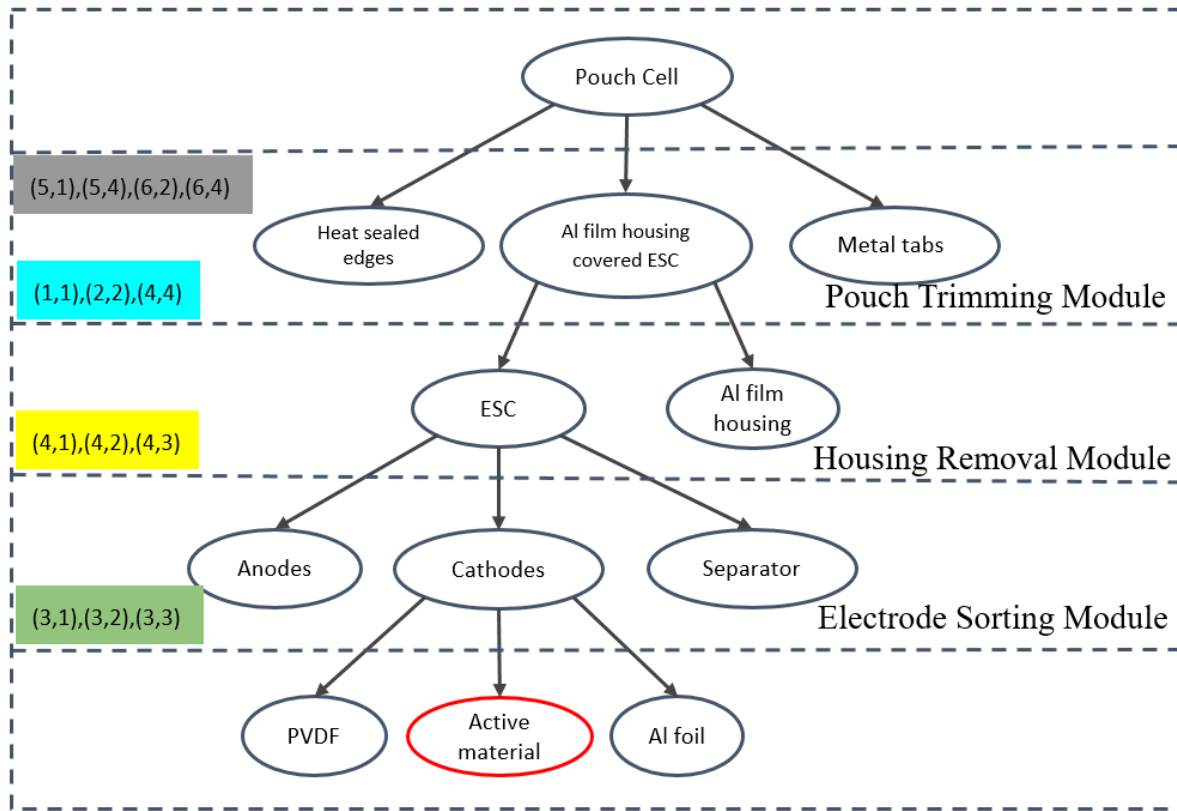


Figure 2- 4 Disassembly precedence graph and module function division.

2.1.3 Modules Design

Figure 2-5 shows the continuous process for direct regeneration of cathode materials recycled from end-of-life LIBs in our lab scale production line. As part of this direct regeneration strategy, our proposed single battery disassembly system has a great potential to

ensure the automatic separation of Al laminated films, separators, cathode sheets, and anode sheets with their integrity well preserved. Before being fed into the disassembly system, end-of-life LIBs need to be fully discharged in salt water to avoid any explosions or fire hazards. Then, three sealed edges along with metal tabs are to cut off from the core area sequentially. The remaining folded Al laminated housing film needs to be stretched from both sides by external forces in order to extract the ESC. Separators need to be unfolded and continuously fed forward. For end-of-life LIBs, electrode sheets tend to attach on the separator due to the surface tension of the electrolyte or the nature bound due to aging. Thus, specialized skiving tools are needed to scrape cathode and anode sheets off from opposite sides of the separator.

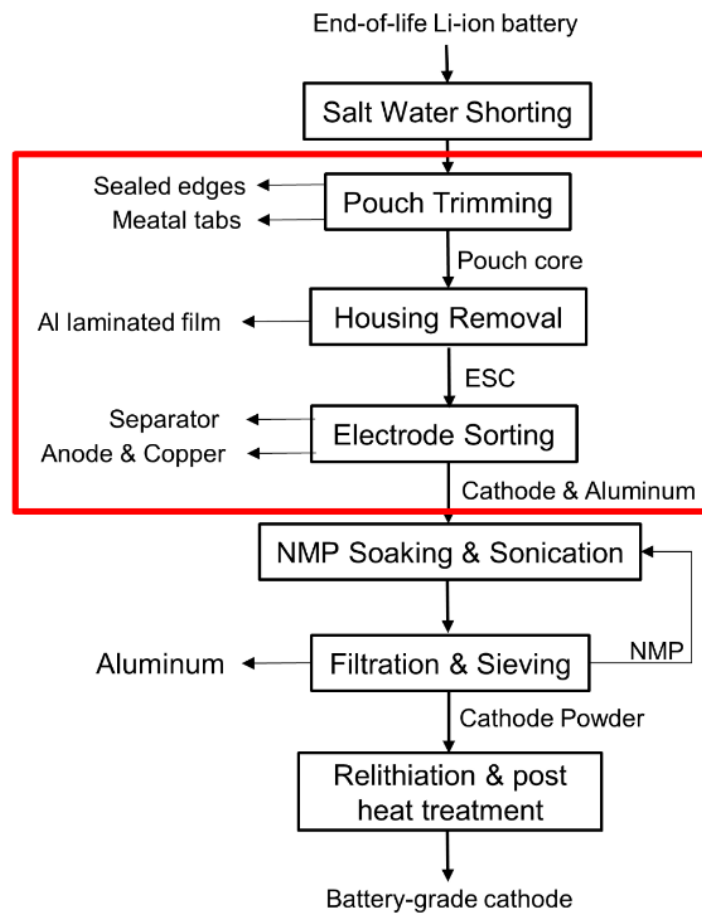


Figure 2-5 Continuous process for recovery of cathode coating from end-of-life LIBs.

Modularization design is adopted to increase flexibility of the disassembly system. The system is physically designed and built into three modules as shown in Figure 2-4 and Figure 2-5: pouch trimming module, housing removal module, and electrode sorting module. These modules should achieve the automated disassembly of H605060 LIB in the precedence designed in Figure 2-4 and finish three key steps encircled in Figure 2-5 correspondingly. All mechanisms or toolsets involved in these three modules can be divided into three categories: end-effectors, fixtures, and transporters. Each module contains several customized key apparatuses to achieve the designed connection removing plan. These apparatuses are usually called end-effectors. Special fixtures are also needed to hold the position of targeted assemblies or subassemblies while end-effectors operate. Between each module, the remaining subassemblies such as Al film housing covered ESC and ESC itself need to be transported between fixtures located in adjacent modules. These apparatuses are defined as transporters. The cooperating of end-effectors, fixtures, and transporters assure the success of connections removing as well as material separation in the automated disassembly line. Detailed design of these key apparatuses are introduced in the next section.

2.2 Modules Design and Prototype

2.2.1 Pouch Trimming Module

In this module, the front edge of the pouch that carries electrode tabs is cut off thus separating each of the electrode layers from the current collecting structure. The opposing side edge seals are also removed so that the Al laminated film housing can be fully separated from the compound.

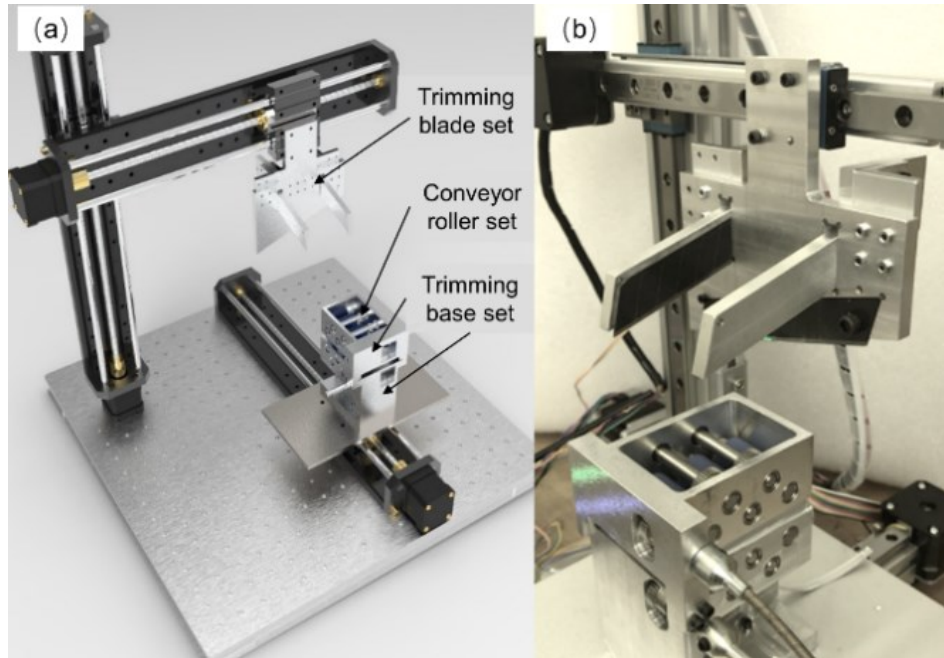


Figure 2-6 (a) CAD design and (b) Prototype of the pouch removal module.

As shown in Figure 2-6, the pouch trimming module consists of three main components: the trimming blade set, the trimming base set, and the conveyor roller set. The trimming blade set is a triple-way aluminum frame with heavy duty breakaway blades fixed in their grooves correspondingly. Each blade is 25-degree tilted from the horizontal direction to decrease the cutting resistance force as well as maintain the cutting speed. The lower trimming base cooperates with the trimming toolset in the trimming process by providing solid support to double-layered Al laminated film. The clearance between trimming blades and edges of the lower trimming base is controlled under 0.3mm while edges of the upper trimming base keep a 0.5mm distance from trimming blades to protect ESCs and avoid unnecessary cutting resistance force. Two conveyor roller sets, each consisting of five powertrain gears and three 25A polyurethane rollers as shown in Figure 2-7, are assembled inside both lower and upper trimming base along with rotary shafts and ball bearings. These rollers with rough surface

texture can hold the pouch cell in position as well as transport the pouch without slippery. Thus within this module, the triple-way trimming blade set and the trimming base set act as end-effectors and the pinch roller sets take the responsibility of both fixture for the trimming process and transporter to deliver the pouch cell into the trimming position as well as move the trimmed subassembly towards the next module.

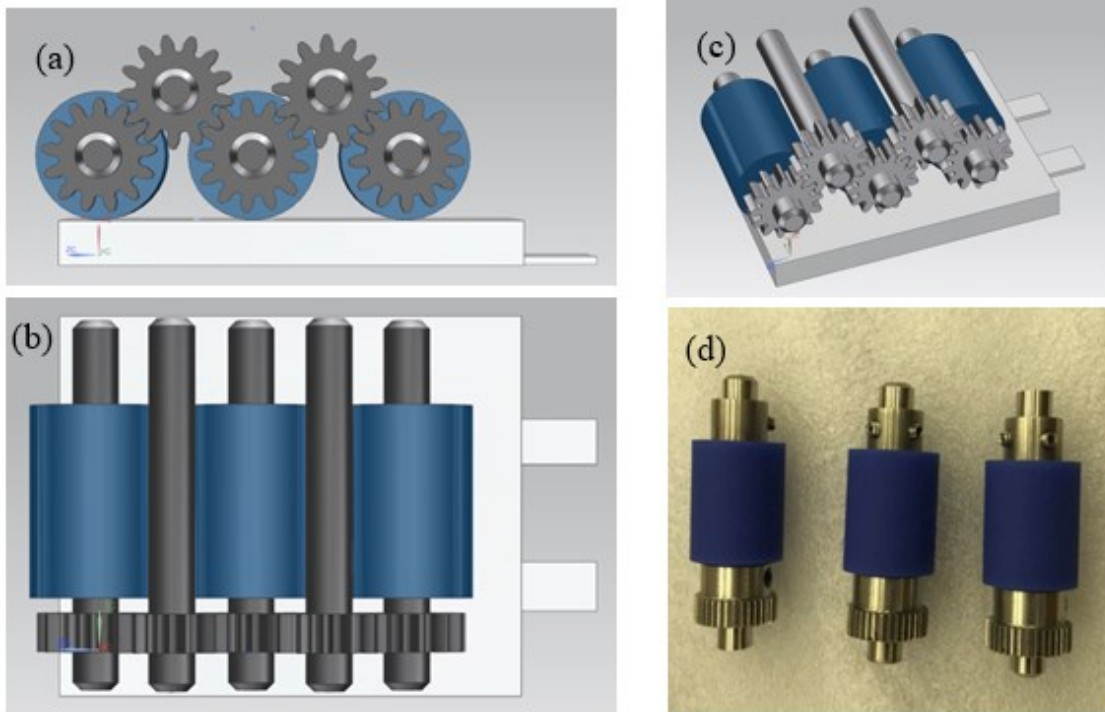


Figure 2-7 Detailed design of the pinch roller conveyor set: (a) side view in CAD model, (b) top view in CAD model, (c) assembly overview in CAD model, and (d) top view of prototyped pinch rollers.

The handling scenario of the pouch trimming process is as follows:

1. Feed fully discharged H605060 pouch cell into the trimming base.
2. Conveyor roller sets transport the pouch into the trimming position.

3. The trimming toolset moves down towards the trimming base and cut off three edges of the housing.
4. Linear motion stage transport the trimming base forward.
5. Conveyor rollers deliver the trimmed pouch towards the next module.

2.2.2 Housing Removal Module

In this module, the remaining Al laminated film housing is to get peeled off from the trimmed pouch. Hence, the recovery of Al laminated film from the end-of-life LIBs is accomplished in this module. Figure 2-8 (a) demonstrates key procedures to stretch the housing and extract the ESC while Figure 2-8 (b) shows the prototype of this module.

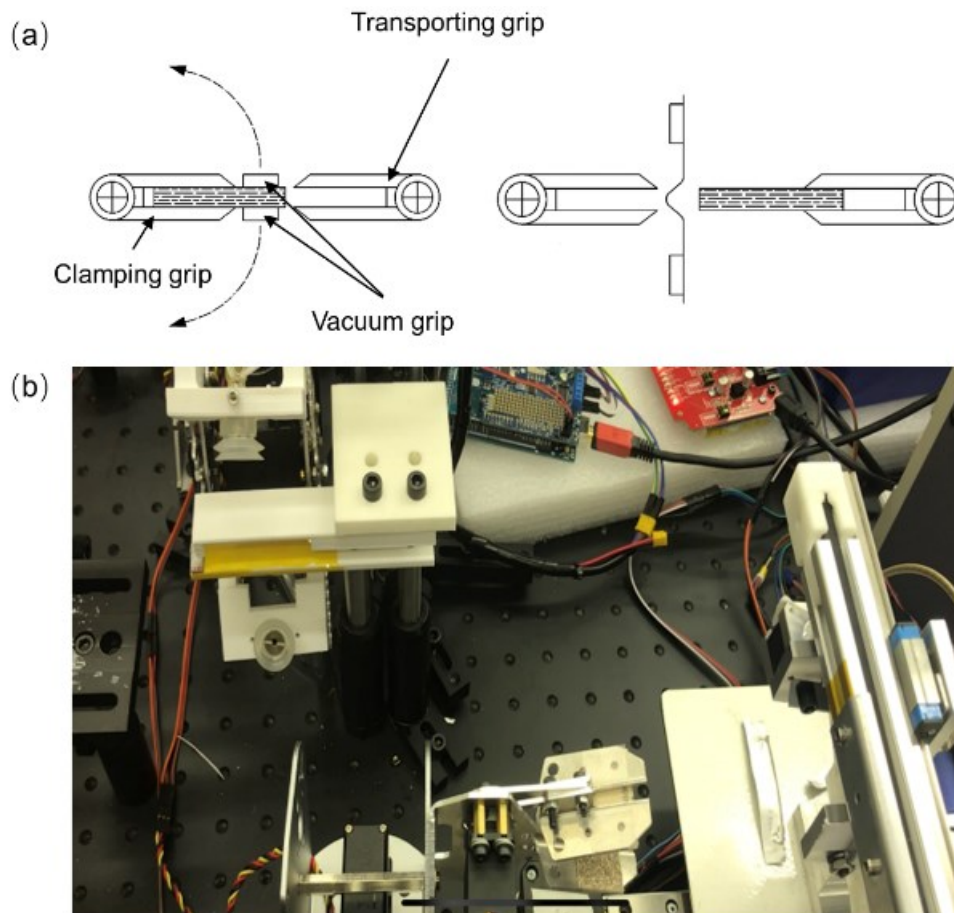


Figure 2- 8 (a) Schematic and (b) Prototype of the pouch removal module.

The housing removal module consists of three gripping apparatuses with specialized functionalities: the transporting grip, the vacuum grip, and the clamping grip. The transporting grip installed on a rotary base is designed to hold and transport the trimmed pouch and the ESC. Distance between two flat arms at their parallel position equals the thickness of the targeted pouch core. As shown in Figure 2-9, the vacuum grip is equipped with a height-adjusting vacuum cup on each arm driven by 12V DC air pumps. These bellows suction cups are made of translucent silicone, which provide sufficient adaptability to the uneven surface of Al laminated film housing. The clamping grip is a fixture with a stationary flat base and vertically movable top clamp. The width and the depth of the groove on the movable top clamp are compatible with the size of targeted pouch cells in order to support and guide the ESC while the vacuum grip peeling off the trimmed housing.

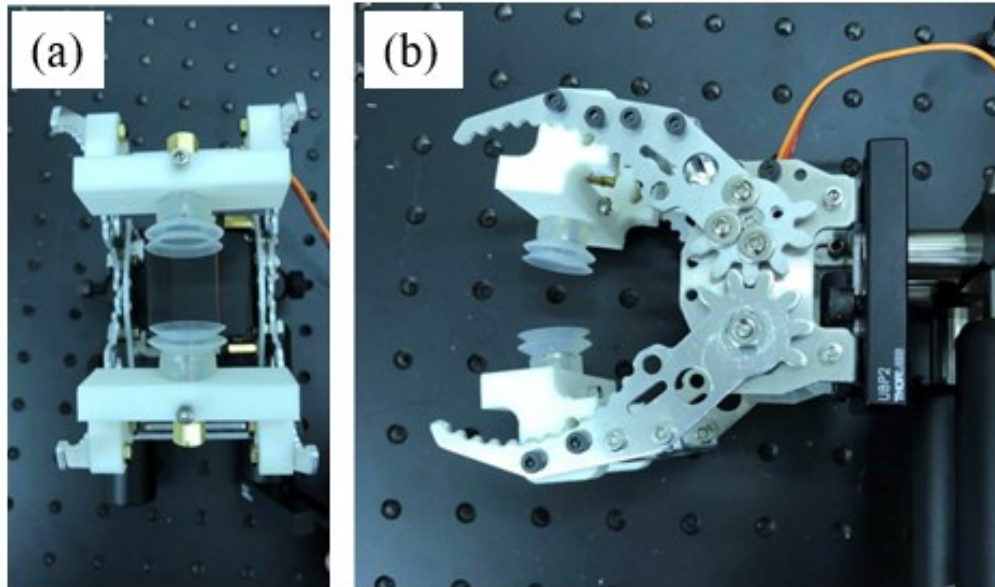


Figure 2- 9 Design of the vacuum grip (a) front view and (b) side view

The handling scenario of the pouch removal process is as follows:

1. The transporting grip extracts the trimmed pouch out of the trimming base.
2. Rotary base spin 90 degrees to feed the trimmed pouch into the clamping grip.
3. The clamping grip clamps the untrimmed side of the pouch core.
4. Rotary base spin 45 degrees to move the clamping grip away from the operation path of the vacuum grip.
5. The vacuum grip closes the jaw and vacuum cups secure the upper and lower side of the Al laminated film housing.
6. Jaws of the vacuum grip peel back upper and lower side of the Al laminated film housing until the front edge of ESC fully exposed.
7. Rotary base spin back 45 degrees.
8. The transporting grip grasps the ESC.
9. Jaws of the vacuum grip further open the Al laminated film housing to its 180-degree configuration while the untrimmed side of the housing pushes the electrode-separator compound into the transporting grip.
10. The Al laminated film housing fell to the waste-recycling stream after the 12V DC pump shut down.
11. The transporting grip delivers the ESC into the next module.

2.2.3 Electrode Sorting Module

The separation of cathodes, anodes, and separators is a critical process for any lithium-ion LIBs recycling processes. It directly influences the purity and recovery rate of the black mass. Our proposed electrode sorting strategy extracts cathode sheets and anode sheets respectively without applying destructive forces. By automatically stretching and feeding the

Z-folded separator, cathode sheets and anode sheets attached on opposite sides of the separator are scraped off by specialized tool sets as the schematic shown in Figure 2-10 (a). Since commonly used PVDF binder can be removed by either dissolving in organic solvents or decomposing at temperatures above 400°C¹⁰², multiple combinations of chemical, thermal and mechanical treatments are then available for breaking the adhesion between Al foil and cathode coating. The prototype of this module is shown in Figure 2-10 (b).

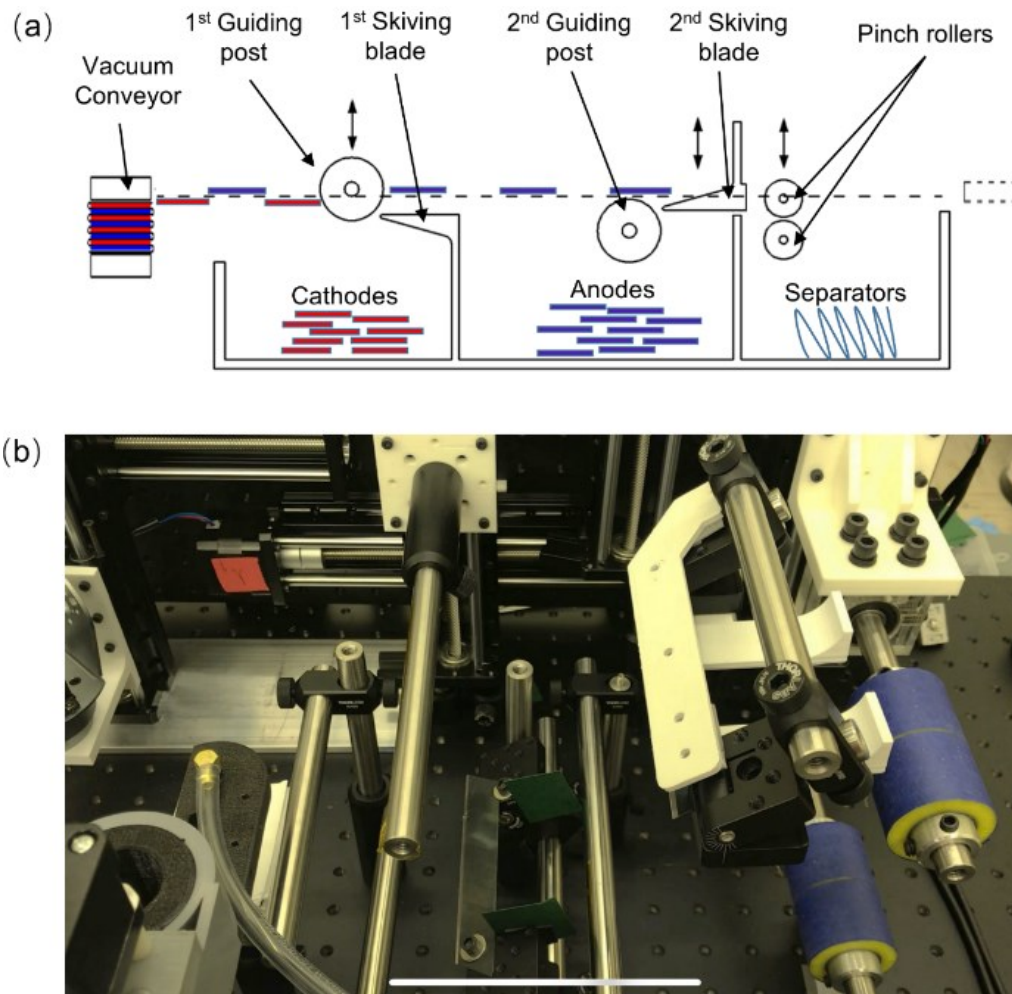


Figure 2-10 (a) Schematic and (b) Prototype of the electrode sorting module

The electrode sorting module consists of four apparatus: the vacuum conveyor, the guiding posts, the skiving blades, and the pinch roller set. The vacuum conveyor is a height-adjusting vacuum cup integrated on the X-Y motion platform. The 12V DC air pump enables the vacuum cup to carry the top layer of the separator longitudinally to pinch rollers. Similar pneumatic securing units as shown in Figure 2-11 are also applied to the vacuum grip prototyped for the housing removal module. These urethane pinch rollers with 35A durometer are able to feed the separator forward continuously while stainless steel guiding posts and break-away skiving blades work as pairs to scrape electrodes off from the separator. After the 1st guiding post pressing down on the soft separator, the front edge of the electrode sheets will detach from the separator because of cathode sheets' lower compliance to deformation. As the separator is still rolling forward, the 1st skiving blade can seek its way through the gap between the front edge of cathode sheets and the separator. Cathode sheets will then fall into the collecting bin due to gravity. Anode sheets attached on the upper surface of the separator are scraped off by the 2nd guiding post and skiving blade in a similar sequence.



Figure 2-11 Pneumatic securing unit for separator delivery.

The handling scenario of the pouch removal process is as follows:

1. The vacuum conveyor secures the top layer of the Z-folded separator and delivers it through the pinch roller set.
2. The pinch roller set squeeze the top layer of the separator as vacuum conveyor release vacuum.
3. The 1st guiding post and the 2nd skiving blade drops vertically to press down the separator.
4. The pinch roller set continuously feeds the separator forward until the separator film is fully paid off.
5. Components of the electrode-separator compound got separated into three collecting bins correspondingly for further treatments.

2.3 System Integration and Testify

2.3.1 Control Architecture

A total of 11 stepper motors, 22 limit switches, 3 servo motors, and 3 pumps are installed in the prototyped disassembly system. The realization of the designed handling scenario for all three modules highly depends on an integrated control architecture. Therefore, a LabVIEW platform is chosen to automate stepper motors, limit switches, servo motors, and vacuum systems. This system-design platform offers great flexibility for design modification, which will benefit the future optimization of this project. The derived control architecture of the prototyped automatic disassembly system is as shown in Figure 2-12.

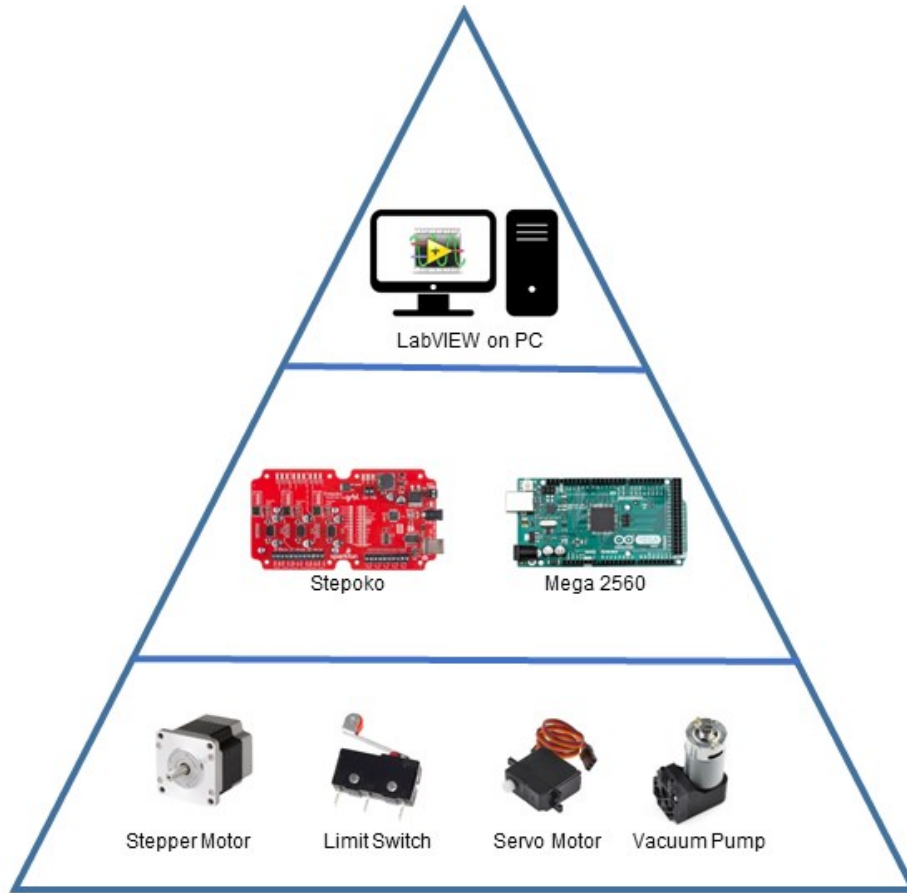


Figure 2-12 Control architecture of the prototyped automatic recycling system

Stepoko motion control boards (MCD) with GRBL firmware are used as local controllers for stepper motors and limit switches. Each module is equipped with one to two MCDs to achieve designed linear motion as well as relocate toolsets to their initial position. Meanwhile, all 3 server motors and 3 DC vacuum pumps are controlled by one Arduino Mega 2560 R3 board. The LabVIEW program which served as a system controller for the ensemble shown in Figure 2-13 is able to supervise the hand-off functions between modules and to indicate event timing for serial operation of end-effectors, fixtures, and transporters.

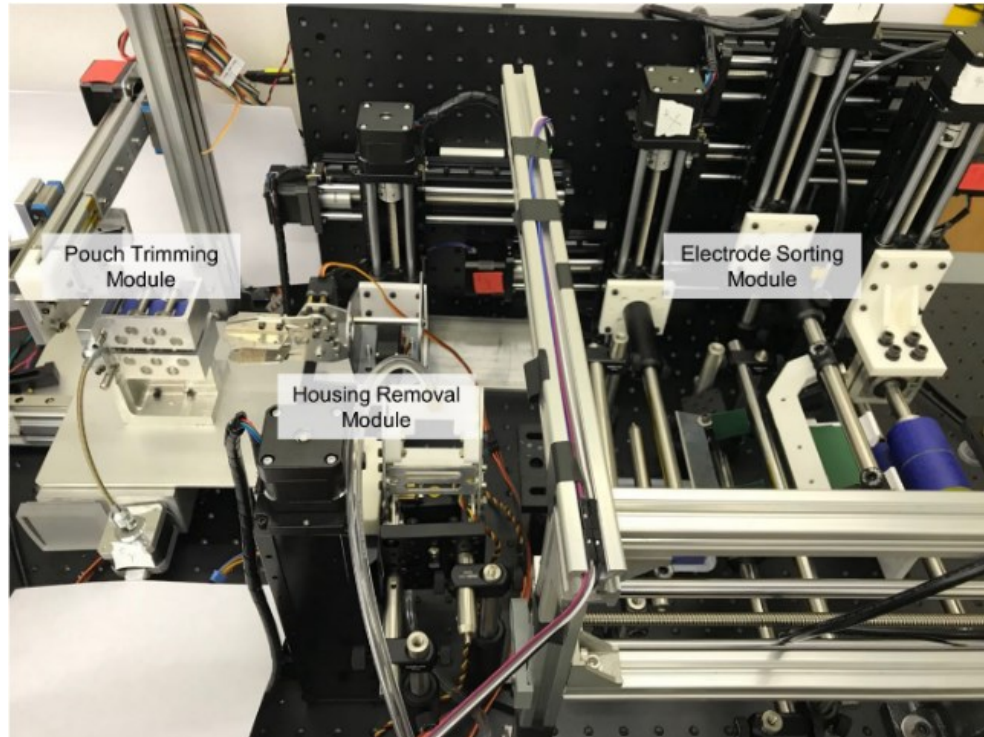


Figure 2- 13 Prototyped H605060 LIB disassembly system overview.

2.3.2 Concept Verification

To assure the safety of the operators at the current prototyping stage, dummy pouch cells are treated to verify the feasibility of the designed disassembly system. In dummy pouch cells, non-toxic materials replaces key components of functional LIBs with similar physical properties. The outer dimension of the dummy pouch cells is 50.0mm*60.0mm*5.8mm with the tolerance of +/- 0.5mm. These values followed the size of H605060 LIB which will be tested for the future development of this system.

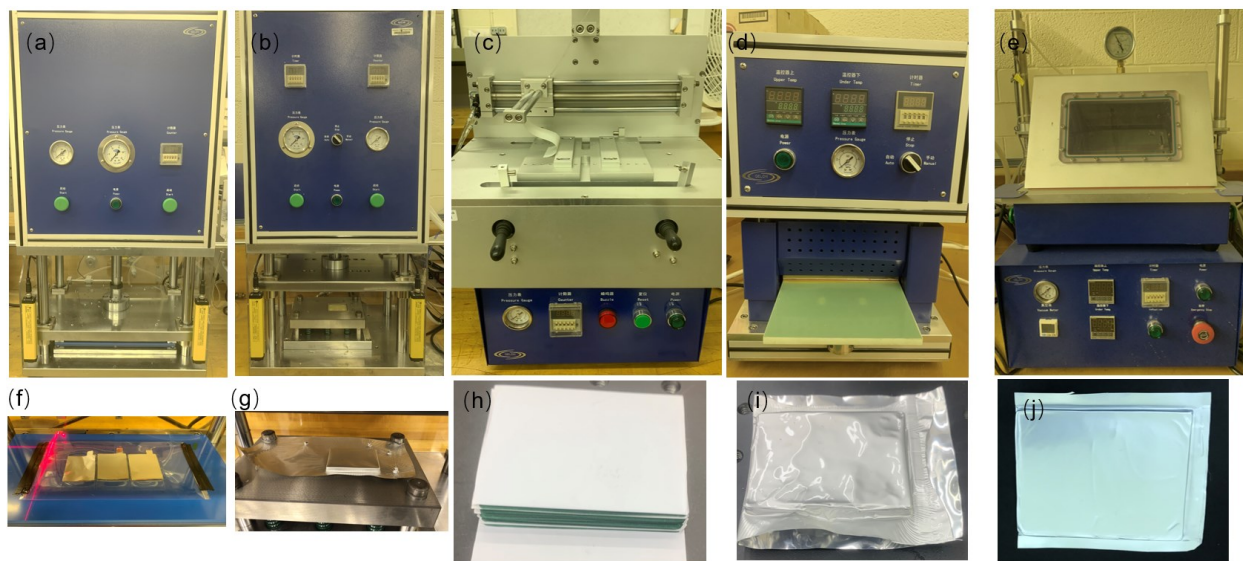


Figure 2-14 Z-folded dummy cell assembly line following the size of a H605060 LIB: (a) Die cut machine, (b) Al laminated film stamping machine, (c) ESC folding machine, (d) Heat sealing machine, (e) Vacuum sealing machine, (f) Trimmed Al foils, (g) Stamped Al laminated film, (h) Folded dummy ESC, (i) Dummy cell with one side edge and the top edge heat sealed, and (j) Vacuum sealed dummy cell.

A pneumatic semi-automated Z-folded LIBs assembly line utilized to assemble dummy cells is as shown in Figure 2-14. 300 micron thick paper cardboards are first trimmed by the die cut machine. Along with an Al/Cu foil tab attached to the right position, these cardboards act as the replacement of double-coated current collectors. For the Al laminated film stamping machine, the depth of the stamping mode is adjusted to 5.6mm so that the overall thickness of the dummy cell can be assured with the 0.1mm thick Al laminated film. An example the Al laminated film stamping process is as shown in Figure 2-14 (g). The ESC folding machine allows us to precisely assemble the dummy ESC by alternatively stacking cathode dummy electrodes and anode dummy electrodes between the Z-folded separator. The dummy ESC will then be placed into the stamped Al laminated film housing and have its side edge and top edge

sealed by the regular heat sealing machine as shown in Figure 2-14 (i). Diluted 3M liquid glue is then filled inside the dummy cells from the open side edge to mimic the adhesion between electrodes and the separator. The metal tab welding process is skipped for the dummy cell manufacturing process since the trimming line at the front edge is located on top of Al current collector foils and the welding points will be abandoned along with the trimmed front edge. Finally, the dummy cell is placed inside the vacuum chamber of the vacuum sealing machine (Figure 2-14 (e)) to drain the air out of the housing and heat seal the remaining side edge.

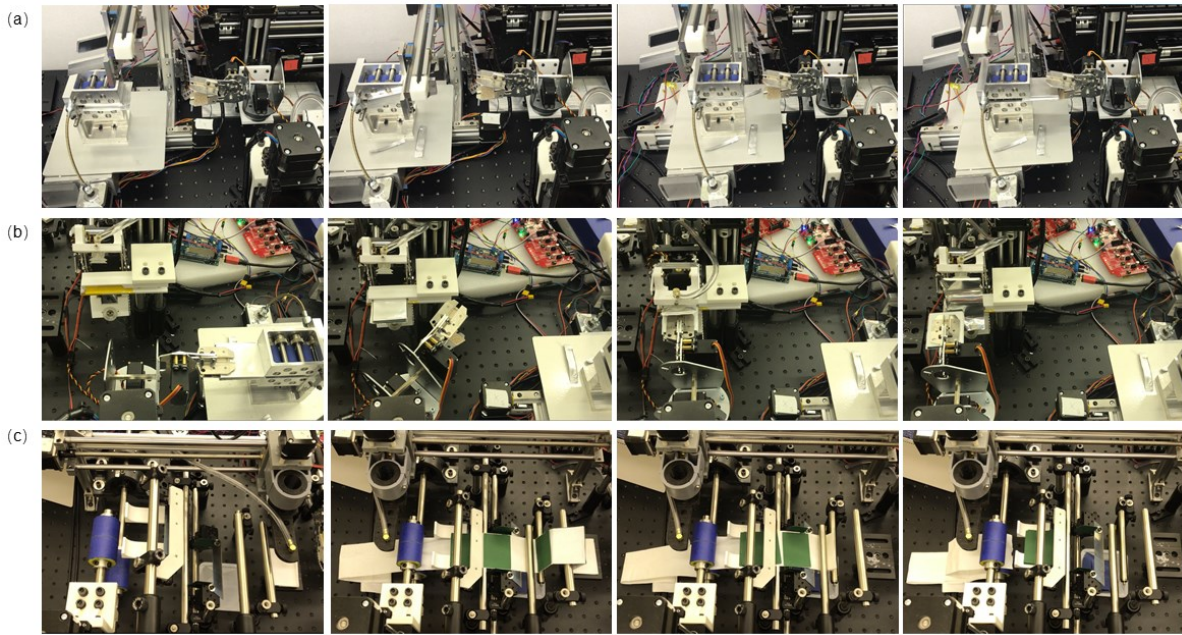


Figure 2- 15 12 key frames from system testing record corresponds to (a) handling scenario 2, 3, 4, and 5 of the trimming module, (b) handling scenario 1, 4, 8, and 11 of the housing removal module, and (c) handling scenario 1, 3, 4, and 5 of the electrode sorting module.

Sealed dummy cells are then disassembled by the prototyped automatic disassembly system. Figure 2-15 shows four key frames from the testing records of each module. Handling scenario 2, 3, 4, and 5 of the trimming module are sequentially shown in Figure 2-15 (a). The

material flow of the single frame in Figure 2-15(b) and Figure 2-15(c) is from the right-hand side to the left-hand side for clearer interpretation. Four frames in Figure 2-15 (b) correspond to handling scenario 1, 4, 8, and 11 of the housing removal module. Recycling of the Al laminated film is accomplished in the fourth frame of Figure 2-15 (b). The Al film housing would fall off from the bellows cup after the DC pump release vacuum. Four frames in Figure 2-15 (c) correspond to handling scenario 1, 3, 4, and 5 of the electrode sorting module. As shown in the fourth frame of Figure 2-15 (c), it is clear that the blue cardboards representing cathode sheets, the green cardboards representing anode sheets, and the separator have been successfully separated and stored in three locations.

The success in testing dummy cells manufactured following the assembly process of a functionally H605060 LIB indicates the design rationality of the disassembly precedence and customized apparatus. To be able to automatically disassemble the EoL H605060 LIB with the prototyped disassembly system, a glove box with the ability to treat hazardous gas emission is needed to keep the entire recycling process under inert atmosphere. This part of the work will be covered in the project future development restricted by glove box hardware availability. Instead, I take a step further in upgrading the prototyped system with industrial vision cameras and sensors to monitor the disassembly process, thus allowing the control system to be more intelligent in detecting system failures and act correspondingly. Some preliminary works on sorting module upgrades are covered in the next section.

2.4 Sorting Module Upgrade and Future Development

2.4.1 Sorting Module Upgrade

The sorting module is rebuilt and upgraded within a fume hood so that the electrode sorting process of a real ESC from H605060 LIB could be recorded and analyzed accordingly.

Apart from the original mechanism assembled in the prototyped disassembly line, three Blackfly S USB 3 mono industrial cameras with 1.6MP resolution and 226 FPS as shown in Figure 2-16 (a) are integrated. These cameras integrate the industry's most advanced sensors within a 29mm*29mm*30mm ice-cube. Both automatic and precise manual control modes over image capture and on-camera pre-processing are available, thus enabling us to record videos and capture images with trigger signals from LABVIEW. A load cell, which is a transducer that measures force and outputs the force signal as an electrical signal, is also integrated into the sorting module. The selected load cell as shown in Figure 2-16 (b) uses strain gauge to detect load changes and hydraulic or pneumatic load cells are also favorable choices. The strain gage type load cell usually integrates four strain gauges in a Wheatstone bridge. Such bridge circuits originally have two balanced legs. When external load deforms the strain gauge, the electrical signal changes can be captured by HX711 24bit precision ADC module that is connected to LABVIEW via Arduino Mega 2560 R3 board.

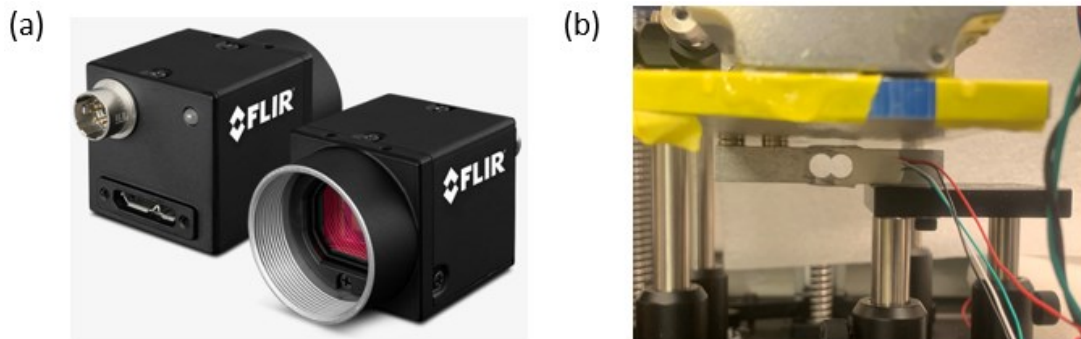


Figure 2-16 Vision-sensor network components: (a) FLIR S USB3 mono industrial cameras with 1.6MP resolution and 226 FPS, and (b) Tension sensor modified from strain gage based load cell.

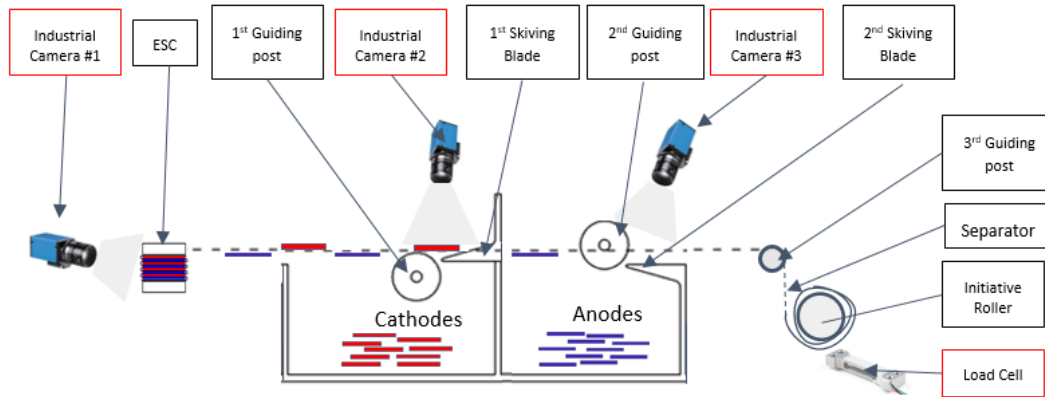


Figure 2-17 Schematic of the vision-sensor network integrated electrode sorting module.

Figure 2-17 shows the schematic of the vision-sensor network integrated electrode sorting module with minimum changes on the separator feeding mechanism. The original pinch roller toolset is replaced by an initiative roller for the convenience of recording the load change on the roller which equals the resistance force applied to the separator from guiding posts and skiving blades. The overview of the upgraded sorting module is as shown in Figure 2-17. The first industrial camera focuses on the ESC unfolding area as indicated in Figure 2-18 (d). The second industrial camera monitors the first guiding post and the first skiving blade from the above so that the separation process of the electrodes positioned on top of the separator can be monitored as shown in Figure 2-18 (b). Ideally, the third industrial camera should focus on the separation process of the electrodes attached to the bottom of the separator. However due to the space restriction, the camera is set to 45° tilted from the horizontal direction and from Figure 2-18 (c). Any electrodes failed to be skived off from the separator can be identified through the semi-transparent wet separator. The output of the load cell is as shown in Figure 2-18 (e), the negative value between 5s and 10s at the very beginning indicates a calibration step by applying a standard 100g weight to the load cell.

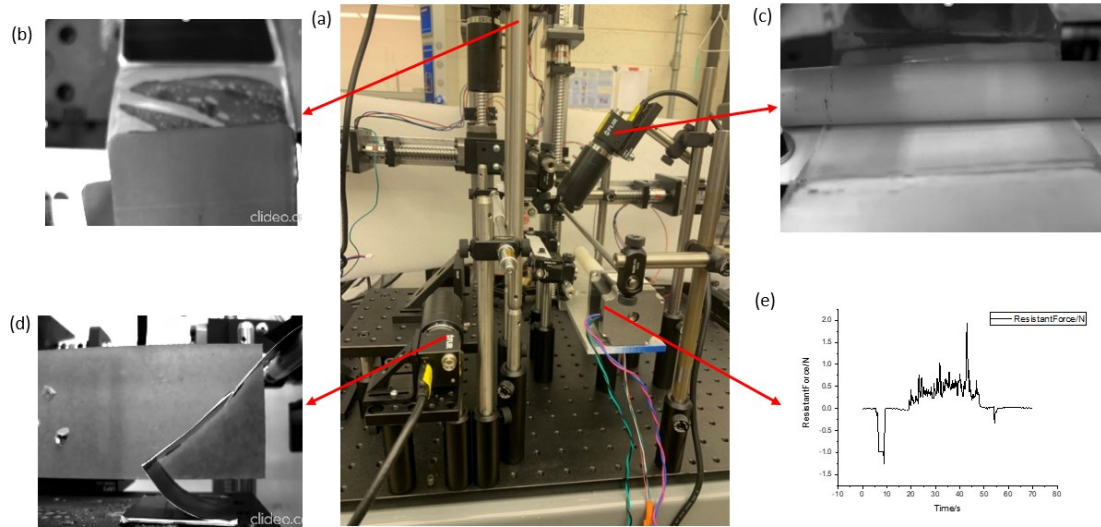


Figure 2-18 System operating with EoL H605060 LIB: (a) Upgraded sorting system overview, (b) Operating frame of industrial camera #2, (c) Operating frame of industrial camera #3, (d) Operating frame of industrial camera #1, and (e) Reading from the load cell.

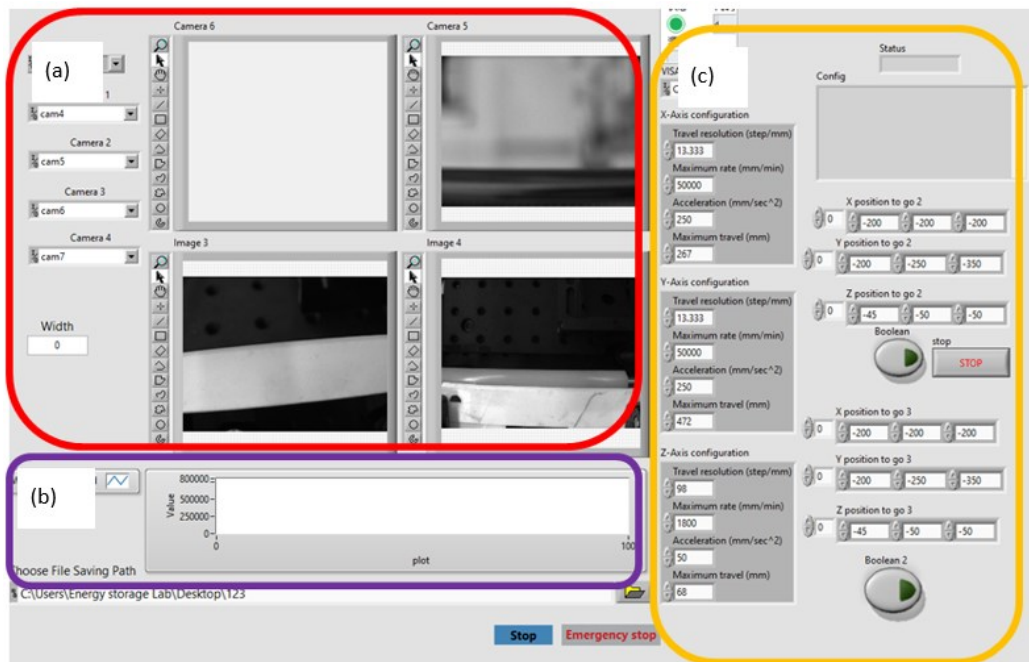


Figure 2-19 LabVIEW control unit Front User Interface: (a) Image acquisition section, (b) Load cell reading section, and (c) Linear motion control section.

The control UI constructed within LabVIEW is as shown in Figure 2-19. The image acquisition section as encircled in Figure 2-19 (a) allows me to integrate as many industrial cameras as needed into the control software, so that future upgrades on the entire prototyped disassembly system can be convenient. Figure 2-19 (b) displays the real time reading from the load cell with the auto scale adjusting function. Figure 2-19 (c) is the linear motion control section integrated with functions of the position restoration, precise linear positioning, and arbitrary speed adjustment. The upgrade of the vision-sensor network for the electrode sorting module initiates the study of the cyber-physical closed-loop LIB disassembly system. The cyber-physical concept and some related preliminary works are introduced in the next section.

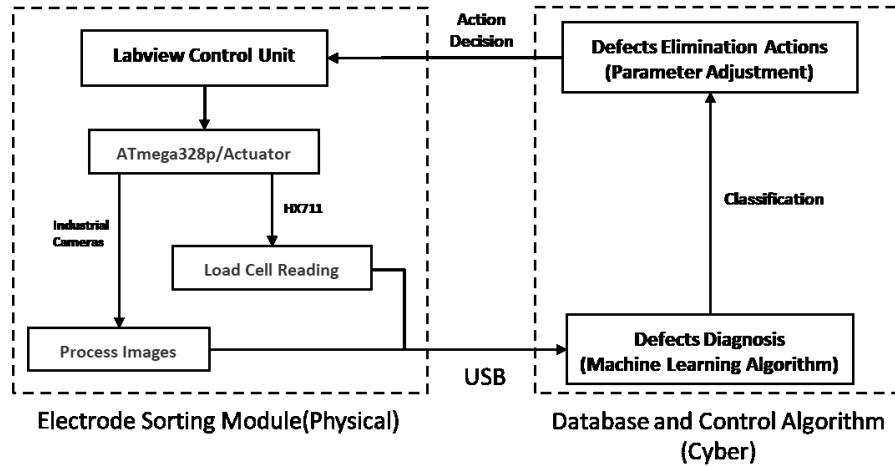


Figure 2-20 Control architecture of the cyber-physical closed-loop process monitor for the electrode sorting module.

2.4.2 Cyber-physical Closed-loop Controller and Preliminary Experiments

The major purpose to design and implement a cyber-physical closed-loop controller in EoL LIB disassembly system is to deal with the uncertain condition of the EoL LIBs. Even LIBs with the exact same dimensions and electrochemical parameters, their conditions at EoL

can be very different due to their unique cycling conditions. Thus, a closed-loop supervision & online machine parameter adjustment system will be needed. Figure 2-20 gives the overall architecture of the cyber-physical closed-loop controller that consists of the physical part and the cyber part. The physical part can be directly transferred from the prototyped disassembly system introduced in the previous sections with an integrated vision-sensor network. The cyber part which will mainly be established within Matlab or Python environments include two steps: defects diagnosis and defects elimination actions. Take the electrode sorting module as an example, the separator from an EoL LIB can be fragile and minimum cracks as shown in Figure 2-21 will lead to the breakage of the separator and eventually compromise the sorting process. If such cracks can be recorded by the industrial cameras once they appear, machine learning algorithms will be able to identify them by classifying the captured images. With the proper physical model or complete experiment design, corresponding parameters can be adjusted to either decrease the pulling force applied to the separator or simply shut down the operation and call for human intervention. Thus, the implementation of this cyber-physical closed-loop monitor will enable the machine to cognize the possible uncertainty and apply necessary parameter adjustment correspondingly in real time. An example of detecting defects as shown in Figure 2-21 and adjusting machine parameters according to the physical model of the apparatus is demonstrated in the rest of this section.

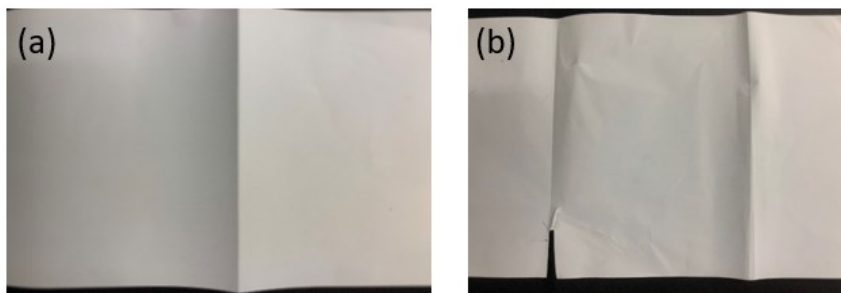


Figure 2-21 Algorithm input (a) intact separator and (b) cracked separator.

Convolutional neural network (CNN) is used to identify the defects by continuously classifying images captured with industrial cameras integrated during the electrode sorting process for it provides promising results in image classification tasks by automatically discovering the interconnections existed between disordered input¹⁸¹. Thus CNN, as a type of deep neural networks, is quite often utilized in computer vision related analysis¹⁸². Figure 2-22 demonstrated the layered structure of CNN working principle. Input images, held as raw pixel values, first go through the feature learning process where features of the images are identified. The feature learning process usually consists of three types of layers: convolution layers, RELu layers, and pooling layers. These layers will compute the output of neurons connected to local regions from the original input images, apply elementwise activation functions, and down sample the volume along the spatial dimensions. The classification process will further down sample the volume of the output within the flatten layer. The fully connected layer is applied to connect all features learned, hence all neurons are now connected. A softmax function is then involved to calculate the probability of each label. The label with maximum probability value will be the final classified category of the input image. In this way, CNN successfully transform the input image layer by layer from pixel values to the final classified category.

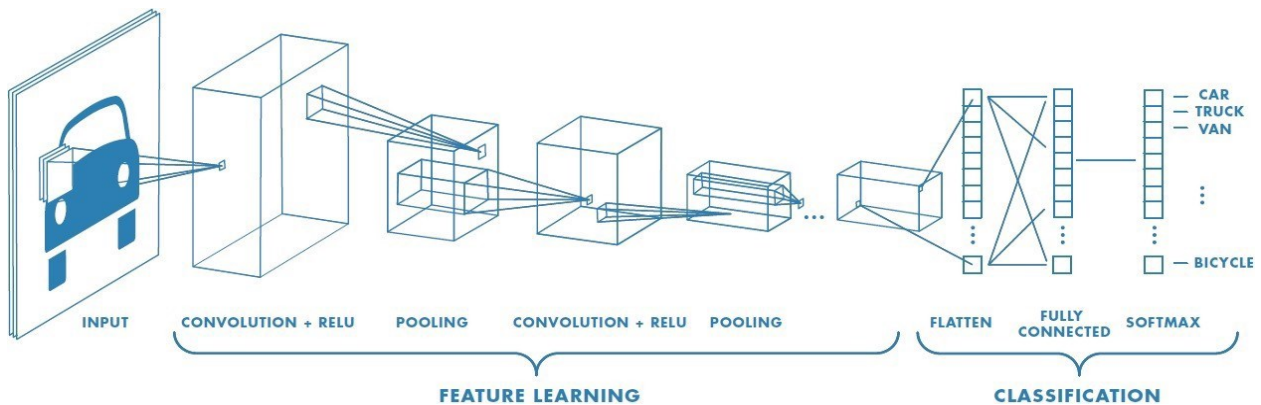


Figure 2-22 Layered structure of CNN working principle¹⁸³.

Two image labels for the cracking defect are defined as “new” and “crack” in the preliminary CNN classification algorithm development. Around 750 images for each label are used as the training data set and 350 images for each label are used as the validation set. Images are downsized from the resolution of 4032*3024 to 200*150 to minimize the model training time. Hyperparameters in a CNN model, such as learning speed, depth of the neuron network, and batch size, determines the neuron network structure and setting. These parameters need to be tuned to the best possible condition based on the classification accuracy of the validation set before initiating the model training utilizing the training set. Here the Bayesian hyperparameter tuning method is adopted. As shown in Figure 2-23, the trained CNN model will label each image with the highest probability value as the classification result.

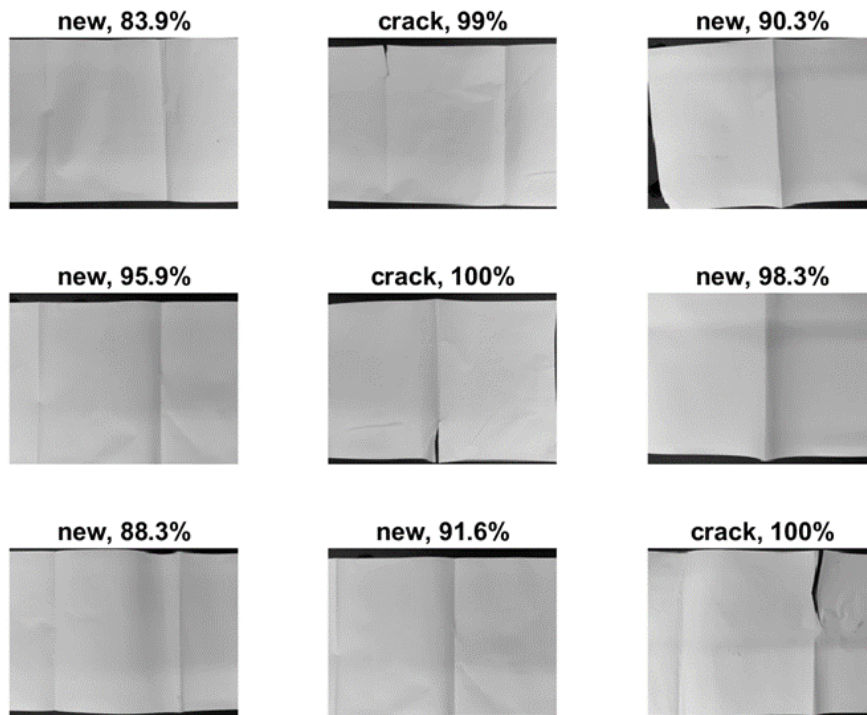


Figure 2-23 Examples of image classification result and probability value.

The trained CNN model is then testified by an 1120 mixed image pool containing images from both categories. A confusion matrix is utilized to demonstrate the effectiveness of trained CNN models. The matrix is a summary of prediction results on the classification problem by giving us an insight of the errors being made by the CNN model. Figure 2-24 (a) gives the basic structure of a 2*2 confusion matrix which is also the matrix size for cracking defect detection since only two labels are involved. P in predicted class and actual class represent that the observation is positive and N represent the negative observation. Here in the cracking defect detection task, P represents the “crack” separator and N represents the “new” separator. True Positive (TP) represents a positive observation and a positive prediction. True Negative (TN) represents a negative observation and a negative prediction. Both TP and TN are favorable results for the observation that agrees with the prediction. False Negative (FN) represents a positive observation but predicted as negative and False Positive (FP) represent a negative observation but predicted as a positive. Thus, FN and FP are major sources of inaccuracy and should be avoided as much as possible. With TP, TN, FN, and FP available, the accuracy of the CNN classification model can be calculated by Eq.2-1. With the confusion matrix of the preliminary algorithm as indicated in Figure 2-24 (b), the accuracy of the trained CNN model proved to be 98.12%, which is a satisfying result.

$$\textbf{Accuracy} = (\textbf{TP} + \textbf{TN})/(\textbf{TP} + \textbf{TN} + \textbf{FN} + \textbf{FP}) = (\textbf{TP} + \textbf{TN})/(\textbf{P} + \textbf{N}) \quad \text{Eq.2-1}$$

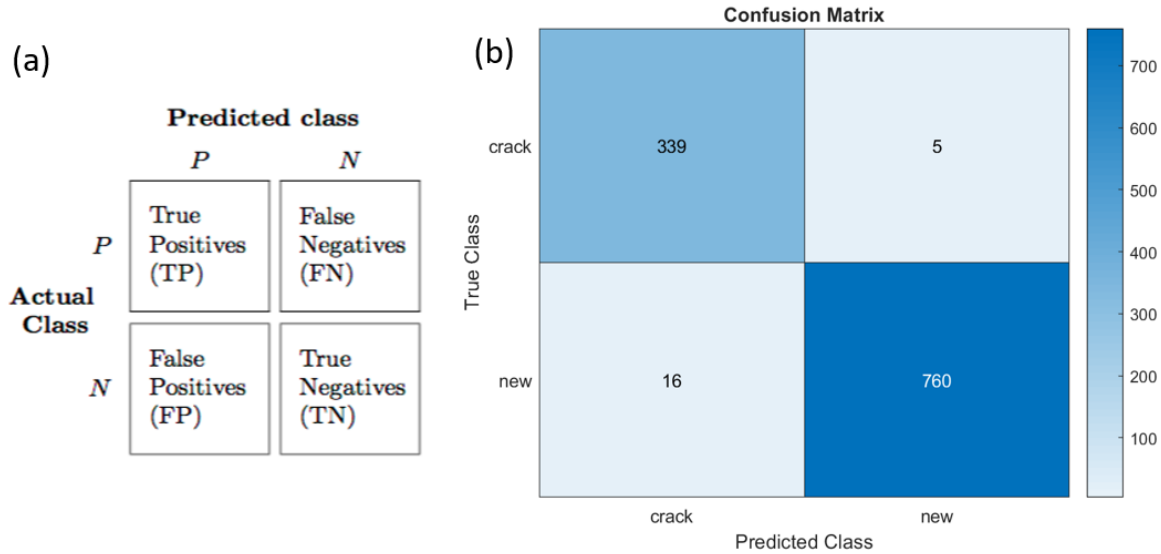


Figure 2-24 (a) Structure of the confusion matrix and (b) Confusion matrix of the preliminary algorithm.

The last step to fulfill the cyber-physical closed control loop is to enable the real time machine parameter adjustment based on the physical model of the mechanism so that detected defects can be contained or even eliminated. After detecting the “crack” defect, a series actions can be taken to decrease the tension applied to the separator along its feeding direction. These actions may include decreasing the separator tilting angle, decreasing feeding speed of the separator, and increasing the blade tilting angle, which need to be further verified by the physical model of the mechanism and series of DOEs. The commands for machine parameter adjustment will be sent from Matlab or Python to LabVIEW, thus the continuous feeding of the separator can be assured by this cyber-physical control loop. The sensor network upgrade and the cyber-physical closed control loop for the entire LIB disassembly system will be completed in the future development of this project.

2.5 Conclusion

An automated disassembly system for recycling end-of-life Z-folded pouch LIBs has been introduced and prototypically realized. Customized tool sets aiming for automatic material handling are designed in each module. Success in treating dummy cells proved the effectiveness of the proposed disassembly strategy. Within this automated disassembly system, cathode sheets, anode sheets, separators, and Al laminated film housing are automatically separated. The integrity of cathode sheets can be well preserved. Compared to the destructive crashing strategy, such improvement will greatly benefit downstream recycling processes, especially for the direct regeneration strategy. Further research activities will focus on upgrading the vision-sensor network and the cyber-physical closed loop control system through the entire prototyped disassembly system so that the reliability and flexibility of the prototyped system can be assured.

Chapter 3 Cathode Coating Separation of Lithium Cobalt Oxide Battery

Recycling EoL LIBs is not only necessary but also urgently needed in recent years. EoL LIBs are metal enriched city “mine” for lithium, cobalt, manganese and nickel. Generally 1 ton of lithium can be recycled out of 28 tons of EoL lithium ion battery^{184,185} which takes 250 tons of mineral ore spodumene along with 1900 tons of water to extract same amount of lithium¹⁸⁶. Meanwhile, discarded LIBs are serious environmental hazards. Residual electrical capacity tends to cause explosions or fire accidents. Commonly used LIB electrolyte salt (e.g., Lithium hexafluorophosphate) reacts with water and release harmful hydrofluoric acid vapor. In terms of the urgency, the increasing demand of LIBs in EV market since 2010¹⁸⁷ indicates there will be a heavy burden on OEMs and governments in the foreseen futures since merely 4 to 15 years’ battery module lifetime^{173,174} are expected. At the same time, the bursting demand of LIBs will also impose great pressure on the supply chain of critical raw materials such as cobalt. The price of cobalt rose by more than 80% over 2017¹⁸⁸.

Currently, there are three main recycling methods in industry: pyrometallurgical recycling (PR), hydrometallurgical recycling (HR), and direct recycling (DR)^{99,176,189}. Both PR and HR methods break the cathode compound down to elemental constituents and selectively extract metal elements from the mix⁷⁴. The simplicity of the overall metallurgical process comes with high energy consumption, large waste generation, and low capability in recovering Lithium and Manganese⁸³, which is challenging for enterprises to make profit out of the battery recycling business. In contrast, DR has the highest material recovery rate and least waste generation among all three recycling methods, and has been actively developing in research

labs towards industrial scale applications^{80,81,115,177,190}. Since the cathode morphology is well-preserved during the entire direct recycling process, the cathode materials instead of elemental constituents can be recycled and reused.⁸³

Commonly used materials extraction processes in LIB recycling involve some types of physical or chemical separation process, such as shredding¹⁰⁶, thermal treatment⁹⁷, and organic solvent methods. Shredding method, which involves multilevel crushing, fine sieving and air-classification¹⁰², introduces a tremendous amount of impurities that are hard to purify in subsequent processes. Thermal treatment method easily leads to change in cathode materials structure, composition and morphology. In our DR, we have developed a novel pre-sorting process to separate cathode sheet, anode sheet and separator¹⁹¹ and an organic solvent extraction process to retrieve active cathode powder by dissolving the binder (e.g., Polyvinylidene Fluoride, PVDF) with the sonication assisted solvent soaking method.

This chapter focuses on the organic solvent method and studies the relationship between the processing parameters and the cathode materials retrieval yield in the organic solvent method using Taguchi DoE methods and Regression Analysis. Processing parameters that have minor influences on the materials retrieval yield from a single cathode sheet are first identified by Plackett-Burman parameter screening method and set to a level that would benefit the yield the most. The remaining parameters along with essential parameters for the potential mass production process are evaluated by Taguchi DoE. Finally, the results of Taguchi DoE are used to generate a regression model that is able to predict the yield under different input parameter combinations.

3.1 Experiment Setup

EoL battery cells (Figure 3-1) used in this work are randomly selected from a pool of waste drone battery modules provided by a third-party battery recycler. In order to minimize the residual energy, the battery modules are discharged by the BD200 battery discharger (Figure 3-2 (a)) to an average cell voltage of below 2V/battery. Discharged modules are then manually disassembled into individual cells.



Figure 3-1 Battery modules disassembled for DOE.

Voltage of each single pouch cell needs to be double checked before being cut open for extracting the electrode-separator compound (ESC). Z-folded ESC structures are found on all selected modules, which results in 60 to 70 single sheet electrodes from each battery. Our previous research¹⁹¹ indicated that fully automated cathodes and anodes separation of Z-folded Li-ion batteries is feasible for automation, thus we only focus on process parameters that influence the yield of cathode powder extraction from the cathode sheets. Separated cathode electrode sheets are then collected for the subsequent soaking and sonicating process as shown in Figure 3-3. The cathode active materials are retrieved by breaking particle-to-particle and

particle-to-Al current collector bonding forces formed by binders. The most commonly found binder type on a LIB is PVDF which dissolves in organic solvents such as NMP, DMAC, DMF, DMSO, and acetone. X. Song⁸¹ indicated DMAC and DMF outperform the other solvents on dissolving effectiveness and cost efficiency. Thus DMAC and DMF are used as soaking and sonication media in our experiments. The high temperature soaking and sonicating process are conducted in a convection oven (Figure 3-2 (b)) and ultrasonic cleaner (Figure 3-2 (c)).



Figure 3-2 Equipment requirement (a) Battery module discharger, (b) High temperature oven, and (c) Ultrasonic cleaner.

The cathode materials yield of the materials retrieval process is estimated by weight difference of the cathode electrodes before and after the soaking and sonicating process. On average, the weight of cathode electrodes ($W_{initial}$) consists of 28% Al current collector and 72% cathode coating. After the cathode separation process, residual cathode electrodes are dried in oven and weighted (W_{post}) again. The final yield of the cathode separation process can then be estimated by Eq.3-1, which is referred to as response Y and yield in this section.

$$\text{Separation Yield}\% = (W_{initial} - W_{post}) / (W_{initial} * 0.72) \quad \text{Eq.3-1}$$

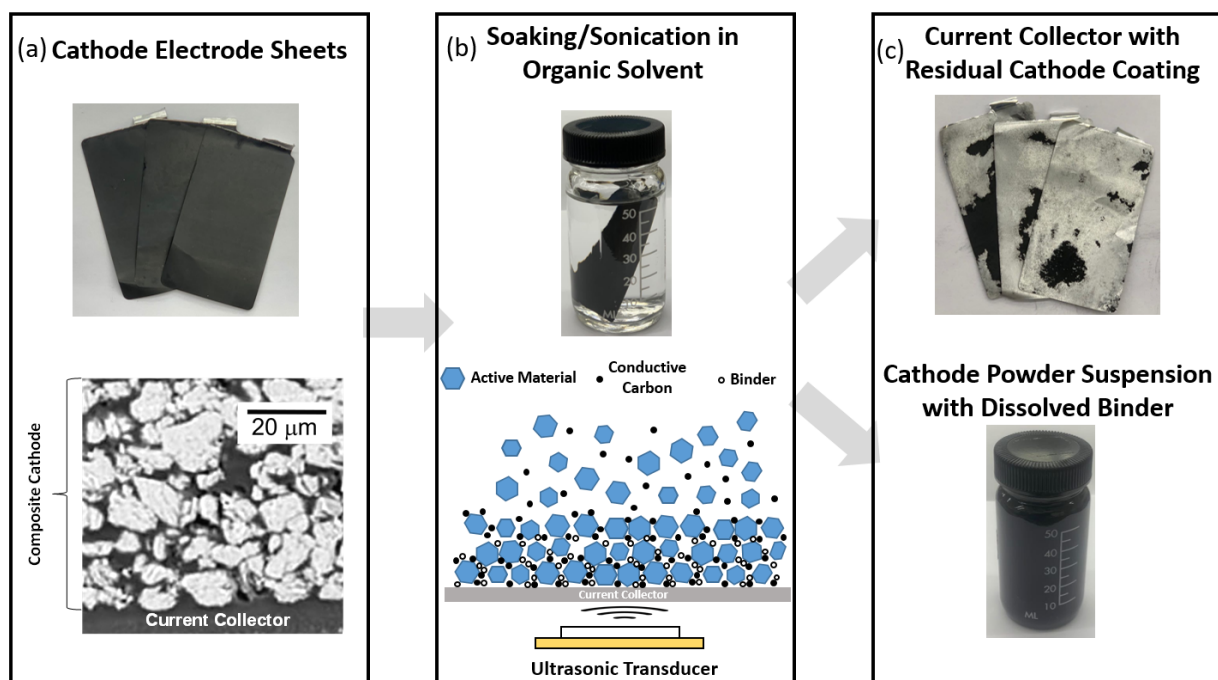


Figure 3-3 Experiment flow with single cathode electrodes.

3.2 Plackett-Burman Parameter Screening Experiment

3.2.1 Plackett-Burman Parameter Screening Experiment Design

A 5 factor 2 level Plackett-Burman parameter screening experiment is constructed to identify the control factors that would influence the yield when dealing with a single cathode sheet. The idea of Plackett-Burman experiment design is to ensure each combination of levels for any pairs of factors are studied for the same number of times, similar to a complete factorial design but with smaller number of runs. Interactions between the factors are considered negligible in the Plackett-Burman experiment. Other than the aforementioned soaking media, the soaking process prior to the sonication process also introduces two potential major quantitative factors: soaking time and soaking temperature. Soaking times are set to be 2h and 6h and soaking temperatures are set to be 60°C and 90°C. Meanwhile, the sonication process

also introduces time and temperature as potential major quantitative factors. In the Plackett-Burman experiment, a single electrode sheet is treated one at a time to prevent interactions between electrode sheets from influencing the PVDF dissolving and cathode powder escaping. Thus the sonication time required is relatively short compared to the following Taguchi experiments and 2 levels of the sonication time are set to 10s and 20s. Two levels of the sonication temperature are set to 40°C and 60°C, which is assured by the heating unit integrated inside the ultrasonic equipment. The ultrasonic equipment available is equipped with a transducer with a fixed frequency of 40 kHz at 120W power level. Thus a total of 5 factors are available for the Plackett-Burman experiment design.

For factors and levels given in Table 3-1, a complete factorial design will require 32 runs while Plackett-Burman design only needs 12 runs (Table 3-2). Each run is repeated 5 times with a single cathode sheet randomly picked from a shuffled electrode pool and responses are averaged and recorded in the last column of Table 3-2. The averaged responses are further tested with analysis of variance (ANOVA) to determine the significance of each factor. ANOVA is an analysis tool used in statistic research that categories input variables inside an experiment data into two categories: systematic factors and random factors. The systematic factors have a statistical significant influence on response or the output, while the random factors will be identified and factored out. The working principle of the ANOVA analysis will be further explained with the Plackett-Burman experiment data in the following section. Meanwhile, the ANOVA test is also helpful in a regression study to determine how independent variables influence the response, which will be demonstrated in the Taguchi experiment later on.

Factor	Soaking Media(A)	Soaking Time(B)	Soaking Temperature(C)	Sonicate Time(D)	Sonicate Temperature(E)
Unit	Type	Hour	°C	Second	°C
Level 1	DMAC	2	60	10	40
Level 2	DMF	6	90	20	60

Table 3-1 Screening experiment parameters and levels.

RunOrder	Soaking Media(A)	Soaking Time (B)	Soaking Temperature (C)	Sonicate Time (D)	Sonicate Temperature (E)	LCO Separation Yield (Y)
1	DMAC	3	60	10	40	63.7
2	DMF	1	90	10	40	50.4
3	DMAC	3	90	10	60	70.2
4	DMF	1	60	10	60	52.6
5	DMAC	1	60	10	40	49.5
6	DMF	3	60	20	60	61.7
7	DMF	1	90	20	40	75.2
8	DMAC	3	90	20	40	95.1
9	DMF	3	90	10	60	64.9
10	DMF	3	60	20	40	80.3
11	DMAC	1	60	20	60	93.4
12	DMAC	1	90	20	60	90.2

Table 3-2 Plackett-burman screening experiment design and result.

3.2.2 Parameter Screening Results

The ANOVA analysis result constructed at 95% confidence interval (CI) from Minitab 19 is as shown in Table 3-3. CI is a range of values calculated by statistical methods which includes the desired true mean with a probability defined in advance. That says, if confidence intervals are developed with a given CI from an infinite number of independent sample data,

the frequency of these intervals containing the true mean equals to the given CI^{192,193}. For example a 95% CI is a range of values that you can be 95% certain contains the true mean of the population (or other population parameters). CI is designated before examining the experiment data and 90% and 99% CIs are also frequently used in analysis. P-value in the last column of Table 3-3 is a probability that reflects the measure of evidence against the null hypothesis between the corresponding independent input parameters and the dependent output response. A smaller p-values correspond to stronger evidence. If the p-value is below $(1 - CI)$, which equals 0.05 in this study, then the null hypothesis is rejected and the corresponding independent input parameter is designated as “statistically significant”^{194,195}. Columns of the ANOVA table for the Plackett-Burman experiments are source, degree of freedom (DF), adjusted sums of squares (Adj SS), adjusted mean squares (Adj MS), F-value, and P-value from left to right. The DF represents the number of information in the data. The ANOVA analysis uses this information to figure out the values of unknown population parameters. An independent variable with k level will always have $k - 1$ DF in order to get the number of values/levels that are free to vary in a data set. The Adj SS are measures of variation for different variables of the model. In the ANOVA table, Adj SS is divided into Term, Error, and Total. Minitab uses the Adj SS for term to calculate the P-value for a variable. Adj MS measures how much variation a variable or a source explains, thus DF of a term is taken into consideration. F-value is the test statistic used to determine whether the independent variable is associated with the response. A sufficiently large F-value indicates that the independent variable is significant. P-value can then be calculated from DF of the specific input variable, DF of the Error, Adj SS, Adj MS, and F-value within an F-distribution form at a CI of 95%.

As aforementioned, input variables with P-values less than 0.05 proved to have enough evidence against the null hypothesis, thus considered to have statistically significant contribution to the response which is the material separation rate in this case. The sonicating time with P-value in 0.003 proved to be a decisive factor towards the material separation rate and will be factored in for the following Taguchi experiment design. Figure 3-4 is the main effect plot of each input variable at different levels. It displays the means for each level within a variable and connects these points with a broken line. If the line is parallel to the x-axis, there is no main effect present. The response mean remains the same across all factor levels. If the line is not horizontal, the steeper the slope of the line, the greater the magnitude of the main effect. As a quantitative factor, the soaking media have the p-value of 0.046 and the main effect plot in Figure 3-4 shows DMAC outperforms DMF, thus DMAC is chosen to be the organic solvent media to be applied in Taguchi experiment design. The P-value of other factors from Table 3-1 are higher than 0.05, thus resulting in much flat main effect plots. These factors agree with the null hypothesis and are taken out of the factor list for the following Taguchi experiment design and their pre-set levels are listed in Table 3-5 along with other essential pre-set process parameters.

Source	DF	Adj SS	Adj MS	F-Value	P-Value
A	1	494.08	494.08	6.27	0.046
B	1	50.43	50.43	0.64	0.454
C	1	167.25	167.25	2.12	0.195
D	1	1742.43	1742.43	22.12	0.003
E	1	29.45	29.45	0.37	0.563
Error	6	472.57	78.76		
Total	11	2956.22			

Table 3-3 Analysis of variance of screening experiment.

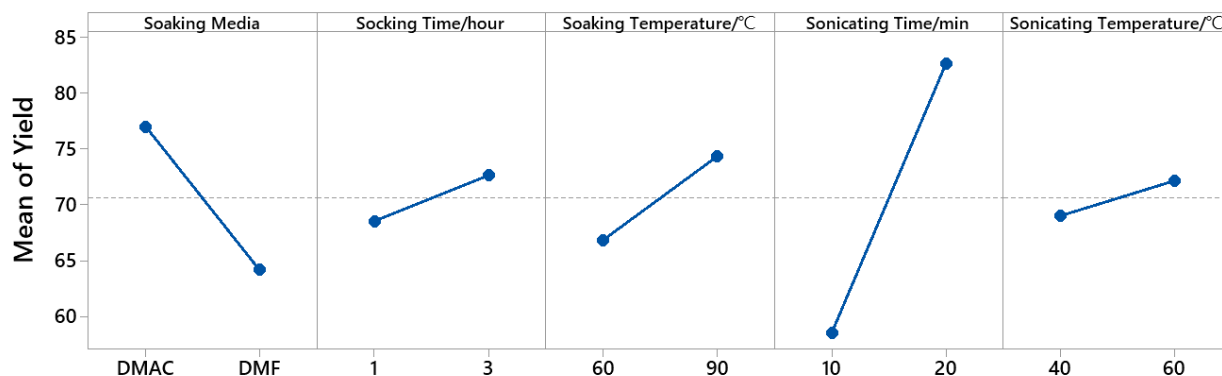


Figure 3-4 Main effects plot for fitted means of screening experiment yield.

3.3 Taguchi DOE

Studying one single electrode at a time can be done at lab-scale to better understand the relationship between processing parameters and materials retrieval yield in organic solvent extraction process. In an industrial relevant environment, however, mass production requires much higher process throughput and introduces more process parameters that need to be systematically studied. Thus to simulate the industrial materials retrieval process, shuffled cathode electrodes are cut into smaller pieces with a controlled size and treated at a much higher solid-to-liquid weight ratio in the following study.

3.3.1 Experiment Design

3 factors with 4 levels from each factor are selected as the independent variables for the Taguchi experiment. Sonication time has been proved to be statistically significant to influence the cathode coating separation efficiency when dealing with the single electrode in the Plackett-Burman experiment. Preliminary experiment indicates that a sonication time on minute scale instead of seconds is required for getting a satisfactory separation yield when dealing with interactions between cathode electrodes and at least tripled solid-to-liquid ratio. Hence, 4 levels

of the sonication time are set to 1 min, 3 min, 5 min, and 7 min accordingly. The other independent variable introduced by cutting the cathode electrode into smaller pieces is the sheet size. The largest sheet size involved in the Taguchi DOE is 4.18cm^2 , which is a quarter of the original intact sheet size. The rest three levels of the sheet sizes are downsized in the order of 0.5 time. The final independent variable is the solid-to-liquid weight ratio. The lowest solid-to-liquid weight ratio introduced in the Taguchi DOE is 5mg/ml, which is already three times of the initial solid-to-liquid weight ratio in the Plackett-Burman experiment. The rest three levels are sequentially doubled and the solid-to-liquid weight ratio reaches 20mg/ml at level 4.

Taguchi DOE is utilized to identify the significance of each control factor chosen in Table 3-4. A regression model is also developed based on Taguchi DOE to predict the response according to levels of independent variables. The Taguchi DoE method is an effective statistical off-line quality control methodology aiming at increasing the robustness of a product or process facing variations over which we have minimum control in the design stage. It is capable of studying both control factors that are controllable during the production, and noise factors that we cannot control when the process is in use. Experiment designed by Taguchi method is able to identify controllable factors (independent variables) that minimize the effect of the noise factors. In a complete Taguchi experiment, noise factors are manipulated so that variability occur on purpose. The optimal control factor (independent variables) can then be determined to improve the robustness of the production process or the product itself by increasing the system resistance to variations from the noise factors. Here in this study, the Taguchi DOE is applied mainly due to its superior capability of dealing with multi-level variables with its unique Orthogonal Array in variable combination subset selection. For a complete n factors and m levels factorial design, a total number of m^n times of repeating

experiments are needed. In the case of 3 factors and 4 levels, the original 64 times repeating experiments can be decreased to 16 times with minimum information loss. The efficiency will dramatically increase as the number of factors and levels increase. Details about Orthogonal Array selection have been explained in many publications¹⁹⁶⁻¹⁹⁸.

Table 3-4 lists all 3 factors and 4 levels to be studied in Taguchi DoE, which enables us to develop a more precise regression model compared to the 2 level Plackett-Burman parameter screening experiment. In this study, the L16 Taguchi orthogonal array is applied to select subsets from combinations of 3 control factors at 4 levels. The Taguchi orthogonal arrays are well balanced to independently evaluate all levels and factors thus each factors and levels can be equally considered. The detailed subset combinations are as listed in Table 3-6. Each subset combination in L16 Taguchi experiment design is repeated for 5 times and yields are averaged and recorded in the last column of Table 3-6 Taguchi L16 orthogonal array. The statistical analysis of yields utilizing ANOVA are carried out using MINITAB.

Factor	Sonicating Time(A)	Sheet Size(B)	Solid-liquid Weight Ratio(C)
Unit	min	cm ²	mg/ml
Level 1	1	0.52	5
Level 2	3	1.04	10
Level 3	5	2.09	15
Level 4	7	4.18	20

Table 3-4 Taguchi experiment parameters and levels.

Parameters	Soaking Media	Soaking Time	Soaking Temperature	Sonicating Temperature	Sonicating Frequency
Unit	NA	Hour	°C	°C	kHz
Level	DMAC	5	90	60	40

Table 3-5 Pre-set process parameters.

RunOrder	Sonication time(A)	Sheet Size(B)	Solid-liquid Ratio(C)	Separation Yield(Y)
1	1	0.52312	5	25.4
2	1	1.04625	10	23.5
3	1	2.09250	15	21.9
4	1	4.18500	20	23.0
5	3	0.52312	10	30.8
6	3	1.04625	5	36.4
7	3	2.09250	20	31.2
8	3	4.18500	15	39.7
9	5	0.52312	15	37.8
10	5	1.04625	20	34.2
11	5	2.09250	5	57.9
12	5	4.18500	10	51.7
13	7	0.52312	50	52.3
14	7	1.04625	15	60.9
15	7	2.09250	10	69.8
16	7	4.18500	5	79.9

Table 3-6 Taguchi L16 orthogonal array and the corresponding separation yield.

3.3.2 Taguchi DOE Results

A continuous quality loss function is used to evaluate the performance characteristics of the Taguchi DoE. This loss function calculates the deviation of a design parameter from the desired value. Value of this loss function is called the signal-to-noise (S/N) ratio. Three categories of S/N ratios are available depending on the goal of experiments:

If the response is to be maximized, that is the larger is better, then:

$$S/N = -10 * \log(\sum(1/y_i^2)/n)$$

If the response is better to be an intermediate value, then:

$$S/N = -10 * \log(\sum(\bar{y}^2/\sigma^2))$$

If the response is to be minimized, that is the smaller is better, then:

$$S/N = -10 * \log(\sum(y_i^2)/n)$$

where y_i is the response of the i_{th} run, \bar{y} is the average response of all runs, σ is the standard deviation of the response, and n is the total number of runs.

Here in our case, to study the yield of the cathode material retrieval, we expect the response to be the higher the better. Thus S/N ratios for yield are calculated from the larger is better S/N calculation equation. For the next phase of the study, the aluminum impurity will be introduced as the second response. S/N ratios for this response will be calculated by “the smaller is better” principle as aluminum debris from the current collector is an unwanted element in the cathode materials retrieved.

The processing parameters rank towards their influence on the yield as well as how parameters influence the yield are shown in the response table for S/N ratio (Table 3-7) and main effect plot (Figure 3-5). The parameters that influence the cathode yield from high to low are sonication time (A), solid-liquid weight ratio(C), and sheet size (B). Both sonication time and sheet size have positive impact on the yield as their level increases, while the solid-liquid weight ratio shows negative influence on the yield as more electrodes being added into certain amount of organic solvent.

Level	Sonication time(A)	Sheet Size(B)	Solid-liquid Ratio(C)
1	27.39	30.95	33.16
2	30.71	31.25	32.08
3	32.94	32.21	31.51
4	36.25	32.88	30.54
Delta	8.86	1.94	2.61
Rank	1	3	2

Table 3-7 Response table for S/N ratio.

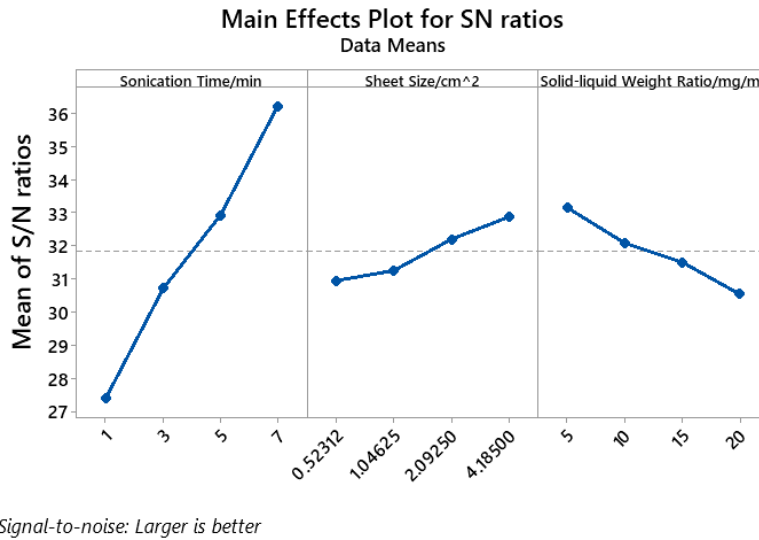


Figure 3-5 Main effects plot for S/N ratio.

To quantify the importance of each control factors and their specific contribution towards the yield, an analysis of variance of the S/N ratio is carried out with a confidence interval of 95%. This means that as long as the P-value of a factor shown in Table 3-4 is less than 0.05, this control factor can be considered to have statistically significant influence on the cathode yield. Individual contribution($P\%$) of the i_{th} factor towards the cathode yield is calculated by Eq.3-2 and recorded in the last column of Table 3-8.

$$P_i\% = Seq SS_i / Seq SS_{total} \quad \text{Eq.3-2}$$

The P-value of the sonication time (A), the sheet size(B), and the solid-liquid weight ratio(C) proved to be well below 0.05 and the P-value rank agrees with the rank indicated by the response table for S/N ratio. The calculated individual contribution ($P\%$) in Table 3-8 indicate that the sonication time has the highest contribution of 86.55% as followed by solid-liquid weight ratio at 7.44% and sheet size at 4.90%.

Source	DF	Seq SS	Adj SS	Adj MS	F-Value	P-Value	P% Contribution
A	3	166.807	166.807	55.6023	155.43	0.000	86.55
B	3	9.443	9.443	3.1478	8.8	0.013	4.90
C	3	14.343	14.343	4.7810	13.36	0.005	7.44
Error	6	2.146	2.146	0.3577			1.11
Total	15	192.74					100

Table 3-8 Taguchi experiment analysis of variance for S/N ratio.

3.3.3 Linear Regression Model for Yield Prediction

As all three factors proved to be statistically significant toward the cathode separation rate, the following linear regression model is established to predict the yield from levels of all factors by analyzing results of Taguchi experiments. Linear regression model is an equation that minimizes the distance between the fitted line and all experiment data. Generally speaking a linear regression model fits the experiment data well if the distances between the predicted value and the observed values are unbiased. To statistically determine how well the model fits the original data, three goodness-of-fit statistics need to be examined in the summary below the developed linear model: S, R-squared (R-sq), and R-sq (adj). S is used to assess how well the linear model describes the response. It represents how far the true value falls from the value predicted by the linear model. The lower the value of S, the better the model describes the

response. R-sq also measures how close the experiment data points are to the regression line, but it is defined by the percentage of the response variable variation that is explained. R-sq is always between 0% and 100% and the higher the R-sq, the better the linear model fits the experiment result. However, R-sq always increases when more terms are added to the model, even if no actual improvement has been added. Thus R-sq (adj) is introduced to compare models that have different numbers or terms. It can incorporate the number of terms to help us choose the best fit model. From the summary table, both R-sq and R-sq(adj) are at a level higher than 95%, which indicate the developed linear regression model is a good fit to the Taguchi experiment result.

$$\text{LCO Separation Yield} = 20.3 + 6.89 * \text{Sonicating Time} + 3.28 * \text{Sheet Size} - 0.96 * \text{Solid/Liquid Ratio} \quad \text{Eq.3-3}$$

Term	S	R-sq	R-sq(adj)
Value	3.71270	96.52%	95.65%

Table 3- 9 Summary table of the regression model for LCO separation yield.

To validate the accuracy of the linear regression model, confirmation tests are requested to compare the predicted cathode separation rate and the experiment value. As shown in Table 3-10, three additional runs are randomly picked from the factor combination pool of the full factorial design. The averaged error of three validation experiments is 3.35%, which is within an acceptable range.

Experiment No.	Sonication Time	Sheet Size	Solid-liquid Ratio	Predicted Value (%)	Experiment Value (%)	Error (%)
1	3	0.523	15	28.26	26.75	5.36
2	5	1.485	10	58.58	58.99	0.22
3	7	2.092	5	70.56	73.73	4.49

Table 3-10 Linear regression model for predicting LCO separation yield verification test result.

3.4 Conclusion

In summary, this study has identified sonicating time, sheet size, and solid-liquid weight ratio as three essential control factors towards the efficiency of the pre-treatment process, especially the organic solvent step. DMAC outperformed DMF and proved to be the most cost effective organic solvent with the highest efficiency for the task. The S/N ratio analysis in Taguchi DOE revealed the contribution of sonicating time (86.55%), sheet size (7.44%), and sheet size (4.90%) towards the final yield. The mathematical relationship between the yield and control factors were successfully established with the result of Taguchi DOE and proved accurate by confirmation tests. The developed linear regression model provide a reference in choosing the proper control factors/independent variables with satisfying accuracy for the future industrial scale production. The success in the yield prediction enables us to study aluminum impurity introduced by sonicating process as the second response for the next step.

Chapter 4 Cathode Coating Separation of Lithium Iron Phosphate Battery

Previous study on predicting the organic solvent approach separation yield utilizing DOE and regression analysis has revealed that a precision linear regression model is able to link the yield with multiple independent input process parameters for EoL LCO cells. However, LFP cell is also a strong competitor in the LIB market, especially the EV market in China. Among the 15.7 GWh sales volume of power batteries in China from 2015, LFP rechargeable batteries accounted for 69%¹⁹⁹. Though the energy density and operating voltage of LFP are lower than that of LCO chemistry, LFP cells hold inherent advantages in low cost, long-term stability, low toxicity, and well-defined performance. It can be foreseen that, in the short future, EoL LFP EV battery packs will rapidly accumulate and pose a pressure on the full product cycle fulfillment. Hence, the yield of treating EoL LFP utilizing organic solvent approach is studied with, again, the DOE method, but with full-factorial experiment design. Since the preliminary study for this Chapter reveals that the organic solvent approach might as well avoid introducing the sonication bath to facilitate the separation of cathode coating and the Al current collector, the number of the parameter drops to a scale where full-factorial experiment is practical. Similar to the LCO study conducted in Chapter 3, a regression model is built to predict the newly defined process yield from levels of independent input variables. An additional yield prediction approaching applying Latin square with the limited number of experiments needed is also introduced at the end of this Chapter.

4.1 Full-Factorial Experiment Setup

Tenergy 3.2V 2500mAh LFP (IFR26650P) rechargeable batteries as shown in Figure 4-1(a) are chosen as the test subject for this study. 26650 in their configuration code represent

a shape standard of 26.5 mm in diameter and 65.4mm in length similar to the popular cylindrical 18650 and 21700 cells. The cylindrical cell is one of the most widely adopted packing styles for secondary batteries. The simple structured ESC that produced from the circular winding process allows the cylindrical cells to better fit the automation environment, thus achieving higher production throughput and a lower cost-per-kWh. The fact that continuous electrodes and separators do not need any cutting step in the ESC production process also contribute to the minimization of production cost by creating a better product consistency. The cases of cylindrical cells are formed from either steel plate or aluminum plate, which provide solid protection to the ESC against the external impact as well as helping with the heat dissipation. Though the uniquely designed gas releasing vent as shown in Figure 4-1(b) increases the assembly difficulty, it provides the incomparable advantage in gas venting and pressure releasing. Thus the housing of the cylindrical cell is finally sealed directly after the electrolyte filling process, without needing an extra gas releasing step in the formation process as the prismatic pouch cells.

To imitate the condition of EoL, IFR26650P LFP cells are cycled on a battery cycler under 2C rate between a voltage range from 2.8V to 3.6V until their capacity falls below 85% of their nominal capacity. The continuous cathode electrodes adopted in IFR26650P are measured to be 52mm in width and 0.8m in length. Manually extracted electrodes are then evenly cut into smaller pieces along the length, which result in 52mm*40mm size cathode electrodes for each experiment. NMP is chosen to be the soaking media as preliminary experiments have revealed an exceedingly higher efficiency of NMP compared to the other organic solvent candidates such as DMAC, DMF, or DMSO in this proposed organic solvent approach.

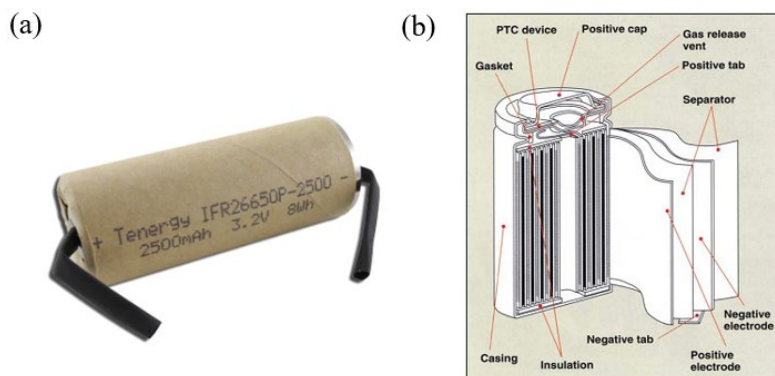


Figure 4-1 (a)Tenergy 3.2V 2500mAh LFP (IFR26650P) power cell rechargeable battery and (b) Typical internal structure of a cylindrical LIB.

Two independent input variables are soaking time and soaking temperature, which proved to be sufficient for developing a precision regression model. Each variable is studied at four levels as shown in Table 4-1. Soaking time is studied at 1h, 2h, 3h, and 4h and soaking temperature is studied at 80°C, 85°C, 90°C, and 95°C. Thus this 2 factors and 4 levels full factorial experiment results in 16 combinations in total.

	Factors		Response
	A	B	Y
Name	Soaking Time	Soaking Temperature	Separation Yield
Unit	Hour	°C	%
Level 1	1	80	NA
Level 2	2	85	NA
Level 3	3	90	NA
Level 4	4	95	NA

Table 4-1 Full-factorial experiment parameters and levels.

The original weight of a 52mm*40mm cathode electrodes is around 680mg among which around 550mg is cathode LFP coating and the rest 130mg is the Al current collector. After being soaked in NMP under high temperature for hours, a unique winkle structure will

appear as the adhesion between the cathode coating and the current collector gets partially destroyed as shown in Figure 4-2. As the soaking time gets longer, the wrinkle area will expand as shown in Figure 4-2 (b), (c), and (d) sequentially. The wrinkled cathode coating can then be easily peeled off almost naturally from the cathode electrodes. The net weight of the remaining cathode electrode (W_{remain}) will be measured again after being sufficiently dried in the oven. The final separation yield that represents the percentage of cathode coating that is “soaked off” from the cathode electrode can then be calculated with the following equation.

$$\text{Saparation Yield \%} = (680 - W_{remain})/550 \quad \text{Eq.4-1}$$

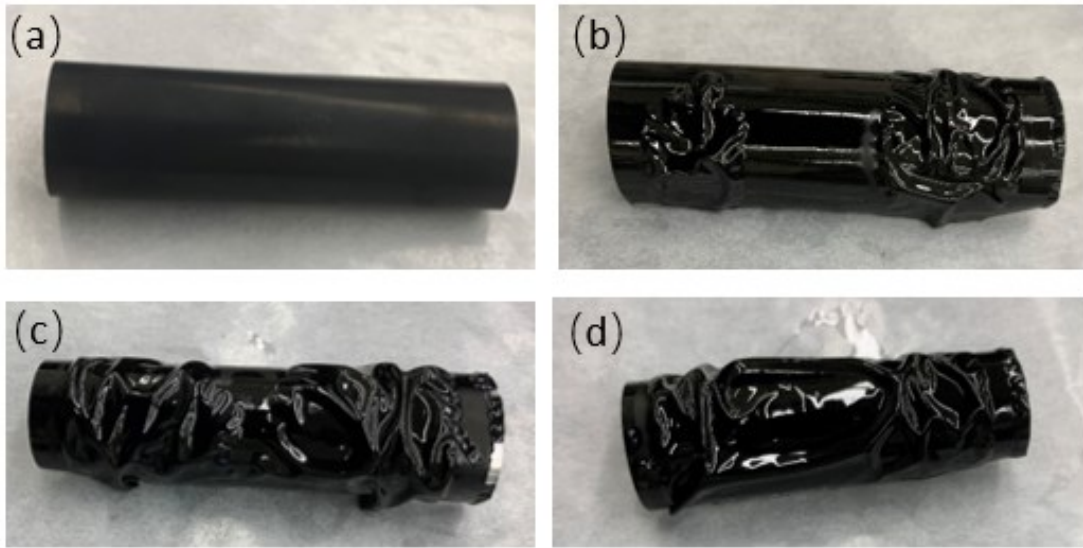


Figure 4-2 The appearance of (a) the original LFP cathode electrode and the appearance of the LFP cathode electrode soaked in NMP under 90°C after (b) 2h, (c) 3h, and (d) 4h.

4.2 Result and Discussion

4.2.1 Full-factorial DOE Separation Yield

The separation yield of each variable combination is calculated with the aforementioned approach and yield of each combination is averaged between three repeated experiments. Thus a total of 48 pieces of 52mm*40mm cathode electrodes are needed, which requires continuous cathode electrodes from 3 EoL IFR26650P LFP cells. After manually dismantle these cells, continuous cathode electrodes are evenly cut into 52mm*40mm pieces. These cathode electrode pieces are then fully shuffled and randomly picked cathode electrode pieces from this pool are to be assigned to each experiment later on. Such precaution minimizes the influence of possible noise factors introduced from inconsistency between different cells and electrode pieces. The averaged separation yield of all 16 combinations are as shown in Table 4-2. From Table 4-2, it is obvious that both independent variables are positively correlated with separation yield. The main effect plot as shown in Figure 4-3 indicates a similar rising trend between sonication time and sonication temperature in the selected range, which confirms the positive correlation between the separation yield and both independent variables.

		Soaking Temperature			
Soaking Time		Level 1	Level 2	Level 3	Level 4
	Level 1	0	0	1%	8%
	Level 2	0	1.2%	14%	30%
	Level 3	2.0%	6.7%	56.5%	90%
	Level 4	5.6%	33.6%	83.9%	95%

Table 4-2 Separation yield of the cathode coating in 2 factors, 4 level full-factorial experiment.

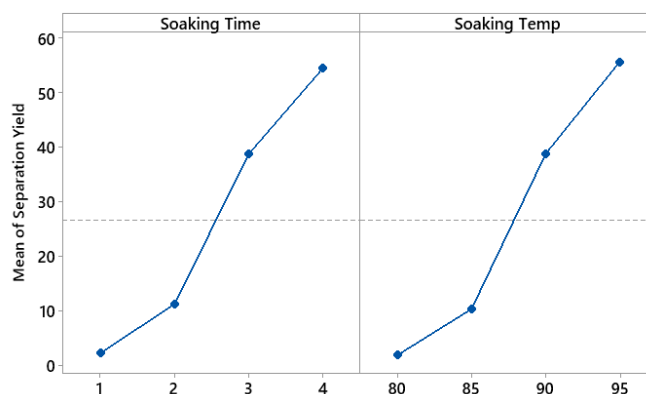


Figure 4-3 Main effect plot for separation yield.

From the post analysis of this experiment series, a unique discovery worth mentioning is the great potential that the organic solvent approach shows in recovering LFP cathode coating without introducing any brutal vibration or mechanical forces to separate cathode coating and the electrode. The sample as shown in Figure 4-4 (a) is soaked in NMP for 4.5h under 95°C, which is slightly longer compared to the sample soaked for 4h under 95°C that achieved 95% separation yield. It is clear that LFP cathode coating material originally adhered on both sides of the current collector naturally detached as whole pieces, which leaves a smooth Al current collector separated from the cathode coating without involving any extra actions other than high-temperature soaking. Though adhesion between particles on cathode coating sheets is considerably weak after NMP dissolves the majority of PVDF, the intact cathode coating sheets are extracted from NMP solvent with caution. The extracted cathode coating sheets are then tiled on a weighing paper with the 52mm*40mm Al current collector covered on top as shown in Figure 4-4 (b). The surface area of the cathode coating sheet is apparently larger than the Al current collector that it is originally coated on, which indicates that the volume of the cathode coating sheet is expanded during the NMP soaking process. The volume expansion might as well be the explanation to the appearance of winked structures on the electrode surface shown

in Figure 4-2. In order to quantify the volume expansion of the cathode coating sheet, 10 LFP cathode electrode pieces randomly picked from the aforementioned pool are soaked inside the NMP under high temperature until cathode coating sheets fully detach from the Al current collector. The averaged surface area of the cathode coating sheets is 23.96cm^2 , which is a 15.2% increase compared to the $52\text{mm} \times 40\text{mm}$ cathode electrode pieces with 20.80cm^2 surface area. Since the thickness of the cathode coating sheet remains at around $150\mu\text{m}$ before and after the NMP soaking process, the total volume expansion of the cathode coating sheet can be considered the same as the surface area expansion. Though the true mechanism for the volume expansion phenomenon requires further investigation, the proposed NMP soaking process indicates a great potential in separating and recollecting the cathode coating from EoL LFP cells with a 100% purity even for industrial-scale production.

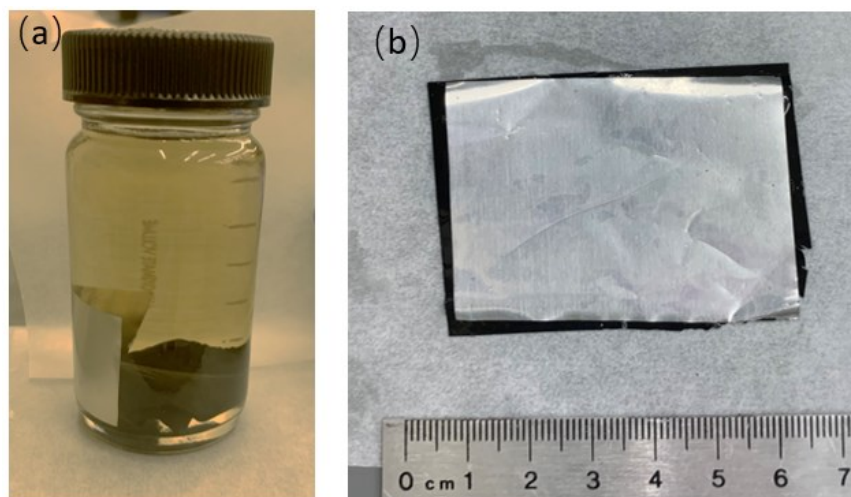


Figure 4-4 Fully separated LFP cathode coating (a) naturally detached from the Al current collector during soaking, and (b) coating expansion comparison with the Al current collector.

4.2.2 Regression Analysis

The regression model developed based on the separation yield from Table 4-2 is as shown in Eq.4-2. A total of four terms are included in the model. Other than the expected terms of constant, soaking time, and soaking temperature, the fourth term proved to be Soaking Time * Soaking Temp, which indicate a nonlinear relationship between two independent variables and the separation yield. The R-sq and R-sq(adj) from the summary table of the regression model are both above 90%, which indicate a fair fit of the model to the experiment observations.

$$\text{LFP Separation Yield} = 126 - 172.6 * \text{Soaking Time} - 1.66 \text{ Soacking Temp} + 2.183 \text{ Soaking Time} * \text{Soaking Temp} \quad \text{Eq.4-2}$$

Term	S	R-sq	R-sq(adj)
Value	10.4498	92.84%	91.05%

Table 4-3 Summary table of the regression model for LFP separation yield.

The ANOVA table for the regression model analysis the significant level of each term appears in Eq.4-2. Noticing that the DF of each term is considered as 1 no matter how many levels the term originally possesses. The total DF equals the total number of observations minus 1, thus in this case equals to 15. The DF of the error then equals the total DF minus the total number of terms involved in the model. The P-value of the soaking time term equals 0.001, which is way less than 0.05. Thus the soaking time term proved to be statistically significant to the LFP separation yield. The P-value of the soaking temperature term equals 0.173, which indicates that the soaking temperature term alone has a much less significant influence towards the separation yield compared to the soaking time term. However, the multiplication of the soaking time and the soaking temperature, which is the only nonlinear term in the regression model, proved to be the most statistically important term to the LFP separation yield with a P-

value even less than 0.001. Next, the accuracy of the developed model is testified by three supplementary experiments.

Source	DF	Adj SS	Adj MS	F-Value	P-Value
A	1	2421.5	2421.5	22.17	0.001
B	1	228.8	228.8	2.10	0.173
A*B	1	2978.4	2978.4	27.08	0.000
Error	12	1310.4	109.2		
Total	15	18305.8			

Table 4-4 ANOVA table for the regression analysis.

The verification of the linear regression model developed in Chapter 3 randomly picked three supplementary experiments from the factor combination pool of the full factorial design and calculated the error of the LCO separation yield from input variables. However, the ultimate goal of the discovered LFP soaking process is to achieve the 100% separation efficiency with the minimum energy consumption and the highest time efficiency. Thus a better approach to testify the accuracy of the developed nonlinear regression model is to predict the minimum soaking time needed to achieve 100% LFP separation yield under preselected levels of the soaking temperatures. Three levels of temperature, 85°C, 100°C, and 110°C, are selected as shown in Table 4-5. Status of the soaked samples are checked every 15min for confirming whether the 100% separation yield has been achieved or not. The averaged error between predicted minimum soaking time and the observed soaking time for three temperature levels are around 6.8%, which is within an acceptable range.

Experiment No.	Soaking Temperature/°C	Separation Yield	Predicted Soaking Time /h	Observed Soaking Time/h	Error (%)
1	85	100%	8.88	9.75	9.7
2	100	100%	3.01	3.25	7.9
3	110	100%	2.32	2.25	3.0

Table 4-5 Result of the non-linear regression model verification tests.

4.2.3 Correlation Pre-confirm with Contour Plot and Latin Square

As proved in section 4.3.2, utilizing a full factorial experiment design for regression model training can achieve a decent accuracy towards the prediction of the LFP separation yield. A total of 16 combinations of the input variables are expected out of the 2 factors and 4 levels full-factorial experiment. With each combination repeated for 3 times to minimize the noise variation, a total of 48 observations are conducted and it would have been a total waste of time and effort if the LFP separation yield does not have anything to do with the two selected input variables in the first place. Thus in order to pre-confirm the correlation between the selected input variables and the LFP separation yield with minimum efforts, an approach combining the Latin Square Design (LSD) and the contour plot visualization approach is conducted prior to the full factorial experiments designed in section 4.3.1.

The LSD is a very efficient experiment design method when only two input variables are involved regardless of how many levels they have. In other words, the LSD is usually used to simultaneously control two sources of variability just as what is needed in the LFP separation yield study. The LSD gets the name due to the fact that it can be written as a square with Latin letters to correspond to observing sampling subsets. The number of rows and columns corresponds to the number of levels of each input variable. Thus, for the 2 factors and 4 levels

situation in this study, the Latin Square consists of 4 rows and 4 columns with 4 choices of sampling subsets, A, B, C, and D, as shown in Table 4-6. Noticing that Table 4-6 is not the only option for dividing the sampling subsets from a 4 by 4 LSD. The sampling subset design is considered as a proper LSD as long as each sampling subset only appears once in each row and in each column. Also because of this restriction, the sampling subsets are orthogonal. Here the sampling subset “A” as encircled in Table 4-6 is selected as the correlation pre-confirm experiment and detailed combination is as shown in Table 4-7.

	Level 1	Level 2	Level 3	Level 4
Level 1	C	A	D	B
Level 2	D	B	A	C
Level 3	A	C	B	D
Level 4	B	D	C	A

Table 4-6 A LSD of the 2 factors and 4 levels experiment.

		Soaking Temperature			
Soaking Time		Level 1	Level 2	Level 3	Level 4
	Level 1		●		
	Level 2			●	
	Level 3	●			
	Level 4				●

Table 4-7 Latin square design of 2 factors and 4 levels full-factorial experiment.

Similar to the full-factorial experiment introduced in section 4.2.1, each combination from the LSD is repeated for 3 times. The LFP separation yield is averaged and recorded in

Table 4-8 accordingly. The rectangular contour plot can then be plotted with the soaking temperature as the x-axis, the soaking time as the y-axis, and the LFP separation yield as the z value. A rectangular contour plot is a graphical technique for representing a 3-D surface by plotting z value, also named as contours, on a 2-D plane. Lines are drawn for connecting the (x, y) coordinates where the same z value occurs. The plot can also reveal the relationship between three explanatory variables and a response variable by the polar contour plot in the 3-dimensional space or the ternary contour plot in the 2-dimensional plane. In this study, the rectangular contour plot as shown in Figure 4-5(a) is adopted since only two input variables are involved. The infill color of the area between contours grows darker as the LFP separation yield gets higher. With merely 4 sampling subset, a quarter of the full-factorial experiments required, clear positive correlations between both soaking time/soaking temperature and the LFP separation yield are revealed by the rectangular contour plot. The full-factorial experiments aforementioned in section 4.2.1 are then conducted with the confidence that a regression model can be successfully developed. The rectangular contour plot of the full-factorial experiments as shown in Figure 4-5 (b) is also plotted with data from Table 4-2. A much similar trend can be observed between two rectangular contour plots.

Soaking Time/h	Soaking Temperature/°C	LFP Separation Yield
3	80	0
1	85	5
2	90	12
4	95	97

Table 4- 8 LFP separation yield of the selected Latin Square sampling subset.

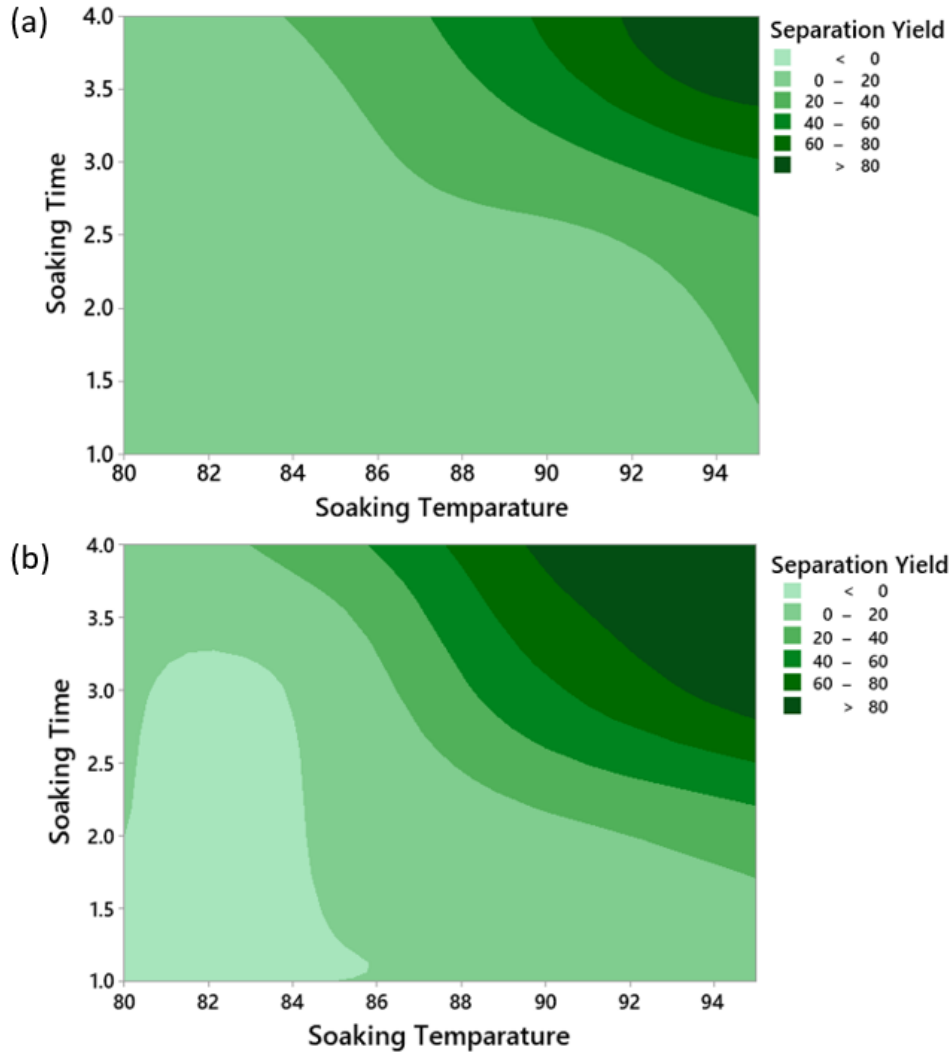


Figure 4-5 The contour plot plotted from the result of (a) the full factorial experiments and (b) the latin square sampling subset.

4.3 Conclusion

The intact LFP coating separation process studied in this chapter offered a great opportunity in achieving 100% LFP active material reclaiming with minimum process complexity for industrial-scale recycling of EoL LFP batteries. Compared to the traditional organic solvent extraction process assisted by the ultrasonic bath introduced in Chapter 3, the single step soaking process can save much effort in liquid-powder separation and organic

solvent reclaim. The success in the development of the LFP separation yield regression model has everything to do with the volume expansion of the LFP cathode coating material, though the mechanism behind this phenomenon requires further study. Meanwhile, the future development of this study should expand the rectangular contour plot to cover a broader range of the soaking time and the soaking temperature.

Chapter 5 LFP Direct Recycling

As aforementioned in Chapter 1, direct recycling process is by far the most environmental friendly recycling approach with the highest material recovery rate. The automated disassembly attempt as well as the cathode coating separation study both serve as the pretreatment steps for the direct recycling process which requires pure cathode coating as the raw material for the resynthesis of new battery-grid cathode powder. Processes such as heat sintering, co-precipitation, and sol-gel¹²³ are major resynthesize methods, among which the heat sintering method involves the direct solid-phase calcination is suitable for treating EoL cathode materials with simple elemental composition like LCO and LFP. This Chapter focuses on the regeneration of EoL LFP reclaimed from experiments in Chapter 4 utilizing the heat sintering method. Samples sintered under different temperatures and atmospheres are first characterized by SEM and XRD. The rate performance of the regenerated samples are then tested in the form of coin cells utilizing lithium chips as the counter electrodes.

5.1 EoL LFP Direct Regeneration

The separated LFP cathode coating sheets collected from the experiments conducted in Chapter 4 are grinded and sieved through a sieve with 325×325 mesh size. Then, the lithium deficiency of the sieved LFP powder caused by battery aging and incomplete discharge then need to be quantified by the Inductively Coupled Plasma Atomic Emission Spectrometer (ICP-AES) test which is an analytical technique used for the detection of chemical elements. It is an emission spectrophotometric technique, exploiting the fact that excited electrons emit energy at a given wavelength as they return to ground state after excitation by high temperature Argon Plasma.²⁰⁰ The mole ratio of remaining Lithium and phosphorus (Li/P ratio) is measured by the ICP-AES to confirm the value of x in the reclaimed $\text{Li}_{1-x}\text{FePO}_4$ powder. Since ICP-AES

analysis requires a sample to be in solution, the 3mg of LFP powder sample is first mixed into the acid solution consists of 7ml Hydrochloric Acid (HCl), 2ml Hydrogen Peroxide (H_2O_2), and 6ml DI water. The solution is then sealed and heated in the convection oven under 70°C for 24h to facilitate the dissolution. After further diluting the acid solution to 0.467 w%, dissolved samples are analyzed by ICP-AES provided by Soil Lab in Virginia Tech. The result shows that the Li/P ratio in the reclaimed $\text{Li}_{1-x}\text{FePO}_4$ powder is around 0.8, which indicates a 20% Lithium loss.

Figure 5-1 demonstrates the process flow of the direct regeneration process conducted. As the ICP result revealed the formula of the EoL LFP to be $\text{Li}_{0.8}\text{FePO}_4$, the EoL $\text{Li}_{0.8}\text{FePO}_4$ powders is mixed with LiOH at a mole ratios of LiOH/ $\text{Li}_{0.8}\text{FePO}_4$ at 20%. Then the homogeneous mixture powders are pressed into pellets with 0.75 inches in diameter. Four samples are sintered at 550°C , 650°C , and 750°C in Ar& H_2 atmosphere (abbreviated as 550-Ar& H_2 , 650-Ar& H_2 and 750-Ar& H_2) and 750°C in Ar atmosphere (abbreviated as 750-Ar). During the sintering process, $\text{Li}_{1-x}\text{FePO}_4$ react with LiOH following Eq.5-1. The tube furnace (OTF-1200X, MTI Corporation) is utilized as the sintering equipment to assure a neutral or reducing atmosphere. Unlike most LCO/NCM direct regeneration processes that sinter the mixture in air²⁰¹⁻²⁰⁵, the LFP cathode would easily oxidize ferrous for ferric with the presence of air or oxygen. Jie.et all analyzed the thermal decomposition of the EoL LFP cathode in the presence of oxygen using Thermogravimetry&Differential Scanning Calorimetry (TG-DSC), XRD, SEM, and Energy Dispersive Spectrometer (EDS). It is suggested that the oxidation reaction of iron phosphate as shown in Eq.5-2 occurs with the presence of oxygen during the high temperature treatment²⁰⁶. Thus in this study three EoL LFP samples are sintered in Ar& H_2 atmosphere and one EoL LFP sample is sintered in Ar atmosphere as the control experiment.

Pelletized material will then be crushed into fine powders after the heat sintering process for further tests.

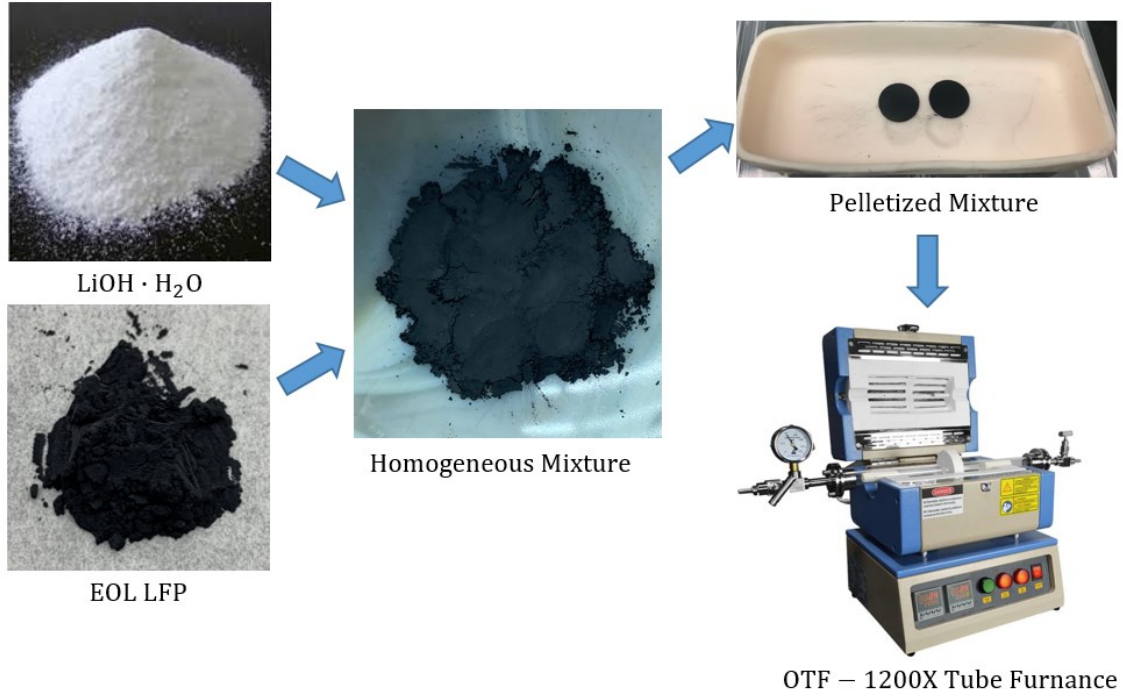
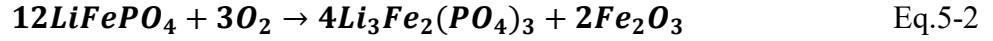
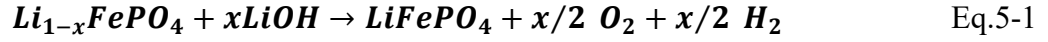


Figure 5-1 Process flow of the EoL LFP regeneration process.

Property of the sintered samples are then characterized by XRD which is a powerful nondestructive technique for characterizing crystalline materials. It provides information on structures, phases, preferred crystal orientations (texture), and other structural parameters, such as average grain size, crystallinity, strain, and crystal defects. The XRD patterns of products are measured by a bench-top X-ray diffractometer (Bruker, D2 PHASER). The scanning rate is to $0.06^\circ/s$ and the 2θ range is from 15° to 80° (Cu $K\alpha$ radiation, 40kV, 30mA, $\lambda = 1.5418 \text{ \AA}$). Figure 5-2 shows the comparison of the XRD pattern between six test subjects. XRD peaks in

the plot are produced by constructive interference of a monochromatic beam of X-rays scattered at specific angles from each set of lattice planes in a sample. The atomic positions within the lattice planes determines intensities of the peak. From the comparison between the pure commercial LFP powders from MSE supplies and the reclaimed EoL LFP, it is clear that apart from LFP peaks, there are other impurity peaks (FePO_4 and P_2O_5) observed in the EoL LFP which can be the decomposition product of LFP after numerous cycles. However, such impurity peaks disappear in all of the regenerated LFP samples as the intensity of the LFP peaks apparently grow stronger indicating that aforementioned impurities react with LiOH to form LFP during the sintering process.

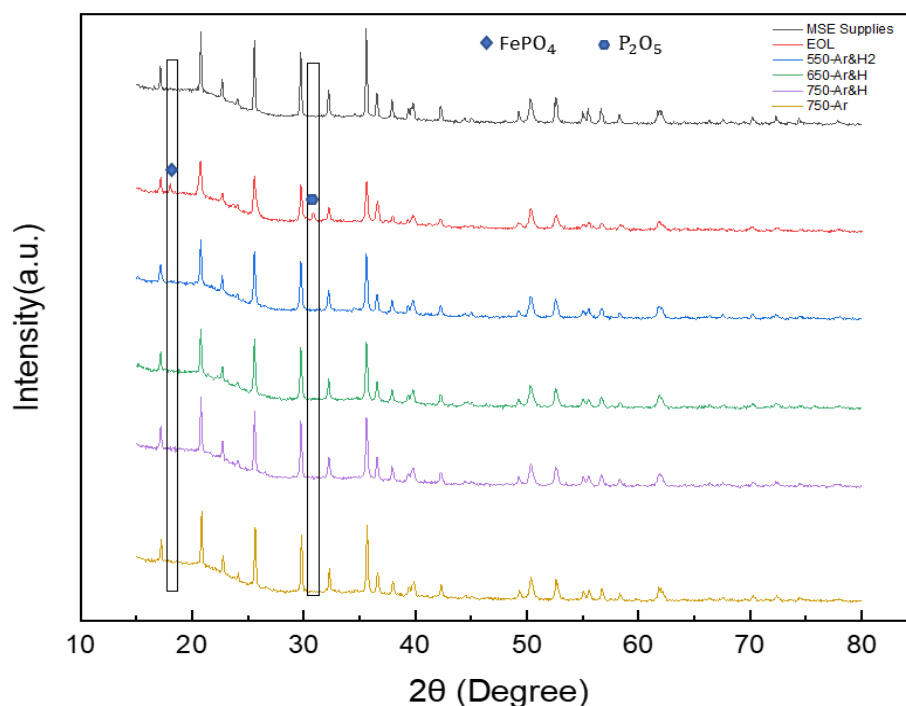


Figure 5-2 The XRD patterns of as-purchased LFP from MSE Supplies, EoL cathode materials, and recycled cathode materials sintered under 550°C , 650°C, 750°C within **Ar&H₂** atmosphere, and recycled material sintered under 750°C in Ar atmosphere.

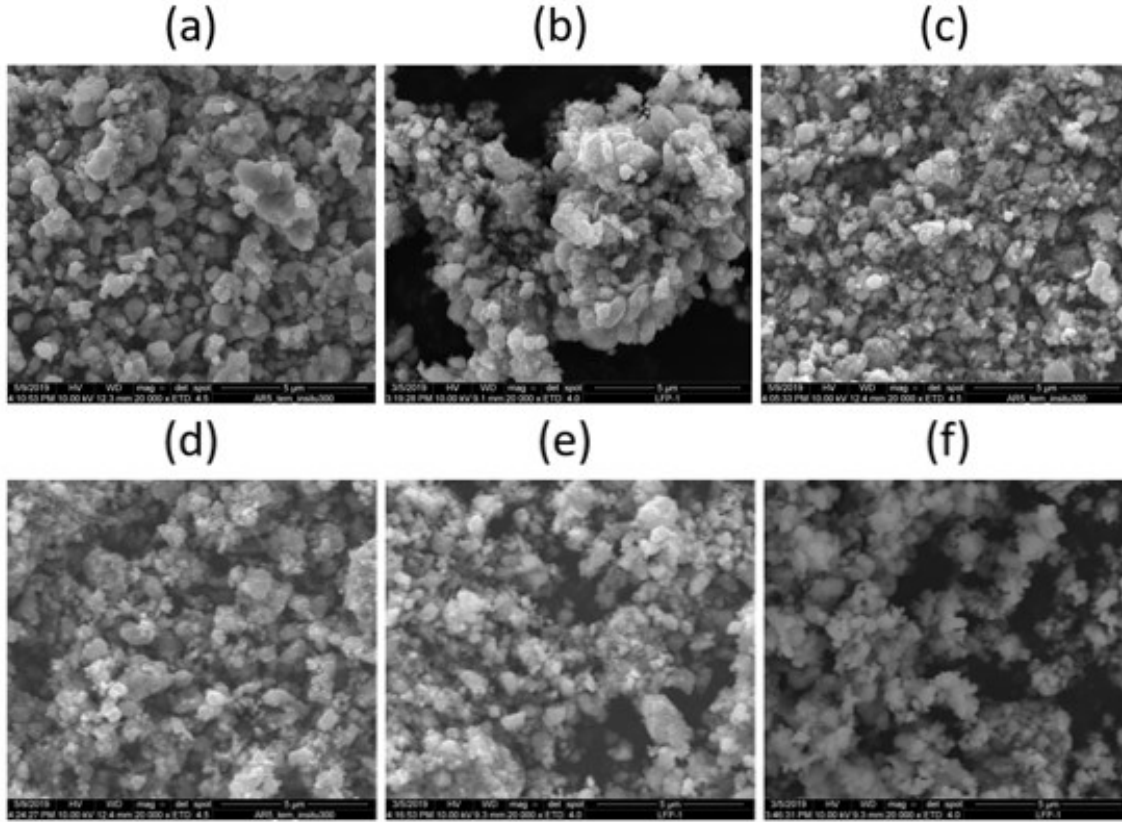


Figure 5-3 The SEM images of (a) as-purchased LFP from MSE Supplies, (b) EOL LFP, regenerated LFP sintered under (c) 550°C , (d) 650°C, (e) 750°C within **Ar&H₂** atmosphere, and regenerated LFP sintered under (f) 750°C in Ar atmosphere.

The morphology of all six samples are scanned by the environmental SEM (FEI Quanta 600 FEG) provided by Nanoscale Characterization and Fabrication Lab (NCFL) in Virginia Tech. The FEI Quanta 600 FEG is able to operate under high-vacuum, low-vacuum, and ESEM modes. The Quanta SEM system is also equipped with analytical systems, energy dispersive spectrometer, and electron backscatter diffraction. From SEM images in Figure 5-3, large secondary particles can be observed from the EoL LFP, which is most likely cause by the existence of the residual PVDF binder. However, these secondary particles does not exist over regenerated LFP samples regardless of the temperature and atmosphere and the particle

distribution in regenerated LFP samples are also more uniformed. Meanwhile, the inert or reducing atmosphere involved in the sintering process may restrain the thermal decomposition of the residual PVDF binder and a small amount of PVDF binder might still exist in regenerated LFP samples. Previous studies^{207,208} have pointed out that the residual PVDF have very limited effects on impedance and the electrochemical performances for the re-assembled cells. Hence, the existence of PVDF is acceptable for the following coin cell electrochemical performance tests.

5.2 Coin Cell Assembly

The electrochemical performance of the regenerated LFP cathode material is then tested in the form of coin cells. LFP cathode electrodes with 14mm in diameter required by coin cells are produced following the process flow as shown in Figure 5-4. LFP cathode powder and Timical carbon are first manually dry mixed for 5min. Pre-prepared 5% PVDF/NMP solution is then added to perform as the binder and the slurry mixture is further mixed for additional 20min. Noticing that within the first two mixing steps, the weight ratio of LFP cathode powder, carbon, and PVDF need to be controlled at 8:1:1, which is the most commonly adopted ratio in related research works. A film applicator with a 200 μ m gap is utilized to coat the slurry onto the Al current collector foil. After drying in the convection oven for 3 hours under 60°C, the coated electrode is cut into smaller round electrodes by the precision disc cutter. The last step before coin cell assembly is to dry the coin cell electrodes in the vacuum oven for additional 12h under 65°C.



Figure 5-4 Cathode electrodes preparation for coin cell assembly.

With cathode electrodes available, coin cells are then manually assembled inside the glove box. The explosive view of the coin cell assembly involved in this study is as shown in Figure 5-5 (a). The graphite anode electrode usually found in a regular LIB cell is replaced by a lithium chip for assuring the consistency between cells. Electrolyte, which is 1mol/L LiPF_6 dissolves in EC/EMC(3:7 in volume), is dropped between each layer during the assembly process. The closed positive case and negative case are then press sealed by the MSK-160E digital coin cell crimper as shown in Figure 5-5 (b). The crimped CR2032 cells as shown in Figure 5-5 (c) are then tested on the CT2001A classic battery tester.

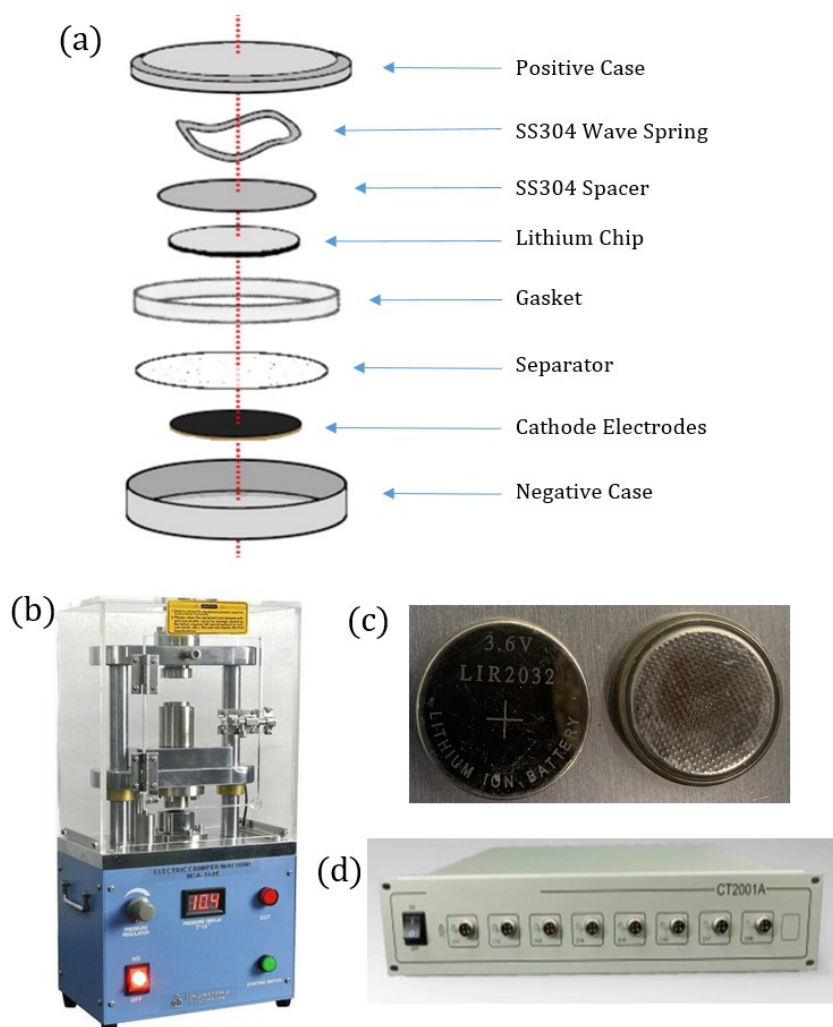


Figure 5-5 (a) Coin cell assembly explosive view, (b) MSK-160E digital coin cell assembly crimper, (c) assembled CR2032, and (d) CT2001A classic battery tester.

5.3 Electrochemical Performance of the Regenerated LFP

The electrochemical performance of five samples are tested. Apart from four EoL LFP samples regenerated under different conditions, the as purchased LFP powder from MSE supplies is also tested as the control experiment to verify the correction of the electrode preparation process and the coin cell assembly process. The rate performance of the assembled coin cells are tested at the C rate of 0.1C, 0.2C, 0.5C, and 2C for 5 cycles each. The discharging cut off voltage is set to 2.6V while the charging cut off voltage is set to 4.0V for all coin cells

tested. To avoid the inconsistency caused by the manually conducted electrode preparation process and the coin cell assembly, three coin cells of each sample are tested and only the ones with intermediate capacity are selected for comparison.

Figure 5-6 (a) compares the second cycle under 0.1C while Figure 5-6 (b) compares the result of the rate performance test. It can be seen that 750-Ar&H₂ has higher capacity than other sintered LFP samples at 0.1C. The reversible capacity for the first cycle of 750-Ar&H₂ is 129.3 mAh/g while 650-Ar&H₂ is 128.6 mAh/g. But the capacity of 650-Ar&H₂ start to exceed 750-Ar&H₂ when discharged at 0.2C. At 0.5C and 1C, the capacity of 650-Ar&H₂ is higher than 750-Ar&H₂ in each cycle. Thus among all sintered materials, 650-Ar&H₂ has the best rate performance as shown in Figure 5-6 (b). Noticing 750-Ar shows the lower specific capacity and poorer cycle performance compared to 750-Ar&H₂, which indicates that the reducing atmosphere is required for the LFP sintering process.

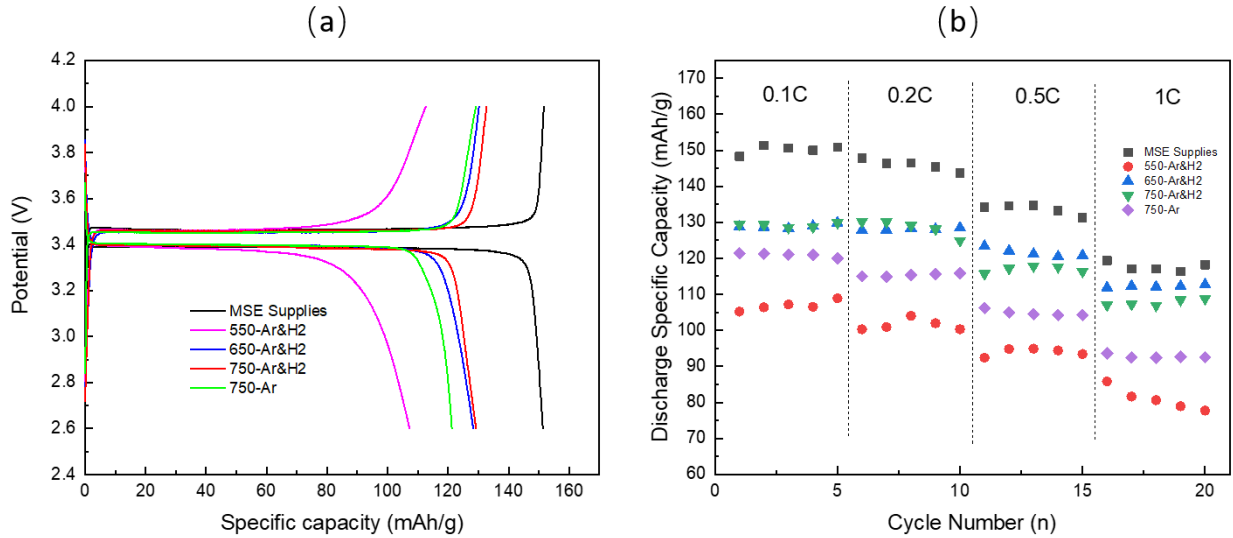


Figure 5-6 The charge/discharge voltage profiles at 0.1C (a) and rate performance (b) of cathode active material mixtures sintered under different conditions.

5.4 Conclusion and Future Development

Utilizing the EoL LFP reclaimed from studies of Chapter 4, the cathode materials have been successfully regenerated by direct solid phase sintering method. The XRD pattern and SEM images indicate that regenerated samples have a purer phase and more uniformed morphology compared to reclaimed EoL LFP powders. The capacities of samples regenerated at 650°C and 750°C under Ar&H₂ both reach around 130mAh/g at 0.1C discharge conditions. However, as C rate increases, the performance of 650-Ar&H₂ exceeds 750-Ar&H₂, which might be caused by decomposition of the resynthesized LFP at high regeneration temperature. The capacity of 750-Ar&H₂ exceed 750-Ar over all C-rates indicating that the reducing atmosphere is necessary for LFP sintering process. Future development of this study may focus on testing the cycle performance of regenerated LFP samples as well as exploring the influence of mixing additional LiOH to EoL LFP at various levels under the optimal temperature and atmosphere.

Chapter 6 Summary and Future Work

6.1 Summary of Contributions

The major goal of this dissertation is to facilitate the industrial application of the pretreatment techniques that is suitable for the direct recycling strategy. Machines and experiments involving the semi-destructive disassembly approach for cathode electrodes extraction from the EoL pouch LIBs and the organic solvent approach for the cathode coating reclamation from the cathode electrodes are designed, conducted, and prototyped.

The first chapter of this dissertation focuses on the complete disassembly strategy of the EoL pouch LIBs starting from the disassembly sequence planning based on the structure of the pouch LIB assembly. After successfully allocating all connections in the disassembly precedence graph, the disassembly system is divided into three consecutive disassembly modules, namely pouch trimming module, housing removal module, and electrode sorting module. Customized transporters, fixtures, and end-effectors are designed and prototyped for each module. The successfully conducted verification tests utilizing dummy cells indicate that the prototyped automated disassembly system is fully capable of extracting intact cathode electrodes out of EoL pouch LIBs.

The second chapter of this dissertation moves forward to the subsequent electrode coating separation process of EoL LCO LIBs focusing on the ultrasonic assisted organic solvent approach. Placket-Burman parameter screening experiments are first conducted and identified the DMAC as the best organic solvent while excluding the soaking time, the soaking temperature, and the sonicating temperature from the list of essential input variables. The following Taguchi DOE proved that the sonication time, the sheet size, and the solid-liquid weight ratio are all essential input variables towards the LCO separation yield. The successfully

developed linear regression model provides an essential tool for predicting the production process yield in the future industrial application of the organic solvent approach.

The third chapter studies the organic solvent approach in separating LFP coating material without involving any external assistance such as ultrasound or brutal impact. The phenomenon of volume expansion of the LFP cathode coating sheet enables the 100% pure coating material reclamation without any Al debris from Al current collector. A non-linear regression model is successfully developed to correlate the input variable (soaking time and soaking temperature) with the LFP separation yield, providing a reliable approach to predict the process variables that are able to minimize the energy consumption and maximize the time efficiency prior to hands-on production process development.

The last part of this dissertation initiates the direct regeneration study of the EoL LFP cathode coating material reclaimed from the organic solvent approach developed in Chapter 3. The XRD pattern indicates a successful repair of decomposed LFP powder after the sintering process and the SEM images shows a much more uniformed particle size distribution in the regenerated samples. The result of the rate performance test indicate that the optimum process parameter of the sintering process is 650°C under the reducing atmosphere.

6.2 Future Work

As aforementioned in section 2.5, the sorting module in the prototyped disassembly system is upgraded by the vision-sensor network as the first step for developing the cyber-physical enhanced automated disassembly system. The machine learning algorithm that cooperates with the physical model of each customized mechanism will fulfill the closed-loop smart control system with much better process flexibility and situation awareness ability compared to the originally developed open-loop control UI in LabVIEW. Such improvement

will also enable the automated disassembly system to deal with uncertainties from EoL LIBs due to years of services with more confidence.

The study of the organic solvent approach introduced in Chapter 3 focuses on the LCO separation yield as the response while putting aside the metal impurity level at the time. As the subsequent process of the semi-destructive disassembly approach, the studied organic solvent approach only need to control the impurity level of Al debris since other metals contained in an EoL LIB such as copper, iron, stainless steel, and etc. are already pre-separated by the prototyped automated disassembly system. More complete experiment designs considering both LCO separation yield and Al debris as responses are required. Meanwhile, the intensity and frequency of the ultrasound need to be taken into consideration in the future study if condition allows.

The organic solvent approach for separating LFP coating material from the cathode electrode is studied with 52mm*40mm electrode pieces at a relatively low solid-liquid ratio. In order to facilitate the industrial-scale application of this approach, future development needs to focus on treating the entire 0.8m LFP cathode electrode strip. Customized fixtures are needed to prevent layer stacking while soaking in NMP. Meanwhile, experiments conducted in Chapter 4 utilize fresh NMP for each electrode piece, which can be both expensive and environmentally harmful for industrial-scale production. Thus the efficiency degradation of reused NMP needs to be studied systematically in the future development.

Though Chapter 5 reveals the optimum sintering temperature and atmosphere by the rate performance test, the cycle performance of regenerated samples need to be further investigated. Meanwhile, the required reducing atmosphere prevents the decomposition of residual PVDF and the oxidation of carbon black, which may influence the electrochemical

performance characterization accuracy of regenerated LFP cathode materials. Thus extra material separation steps aiming at minimize the residual PVDF and carbon black in the regenerated LFP cathode material are expected for future development of the direct recycling research works.

Apart from the aforementioned future works corresponding to research activities of each Chapter, future studies in adopting Industrial Internet of Things (IIOT) in LIB remanufacturing process can be a crucial assurance for decreasing variation in the final product as well as reducing the production cost. Previous study²⁰⁹ indicated that by applying Advanced Process Control and streamline the production/material flow, we expect reduced cost of the battery management system, increased uniformity and yield of individual batteries, and at least 20% reduction of the manufacturing cost in battery manufacturing processes. Such approach could benefit the LIB re-manufacturing process even more since much more variations in supply chains and states of raw material (EoL LIBs) are expected. Thus how IIOT could enhance the efficiency and effectiveness of the LIB remanufacturing process will be studied in the future development of this dissertation.

REFERENCES

- 1 Whittingham, M. S. Electrical energy storage and intercalation chemistry. *Science* **192**, 1126-1127 (1976).
- 2 Mizushima, K., Jones, P., Wiseman, P. & Goodenough, J. B. Li_xCoO_2 ($0 < x < 1$): A new cathode material for batteries of high energy density. *Materials Research Bulletin* **15**, 783-789 (1980).
- 3 Yoshino, A., Sanekika, K. & Nakajima, T. (Google Patents, 1987).
- 4 Prize, T. N. The Nobel Prize in Chemistry 2019. (2019).
- 5 Fergus, J. W. Recent developments in cathode materials for lithium ion batteries. *Journal of power sources* **195**, 939-954 (2010).
- 6 Whittingham, M. S. Lithium batteries and cathode materials. *Chemical reviews* **104**, 4271-4302 (2004).
- 7 Yazami, R. & Touzain, P. A reversible graphite-lithium negative electrode for electrochemical generators. *Journal of Power Sources* **9**, 365-371 (1983).
- 8 Eftekhari, A. Low voltage anode materials for lithium-ion batteries. *Energy Storage Materials* **7**, 157-180 (2017).
- 9 Hayner, C. M., Zhao, X. & Kung, H. H. Materials for rechargeable lithium-ion batteries. *Annual review of chemical and biomolecular engineering* **3**, 445-471 (2012).
- 10 Chawla, N., Bharti, N. & Singh, S. Recent advances in non-flammable electrolytes for safer lithium-ion batteries. *Batteries* **5**, 19 (2019).
- 11 Fergus, J. W. Ceramic and polymeric solid electrolytes for lithium-ion batteries. *Journal of Power Sources* **195**, 4554-4569 (2010).
- 12 Yao, X. *et al.* Comparative study of trimethyl phosphite and trimethyl phosphate as electrolyte additives in lithium ion batteries. *Journal of power sources* **144**, 170-175 (2005).

- 13 Younesi, R., Veith, G. M., Johansson, P., Edström, K. & Vegge, T. Lithium salts for advanced lithium batteries: Li-metal, Li-O₂, and Li-S. *Energy & Environmental Science* **8**, 1905-1922 (2015).
- 14 Zhang, S. S. A review on electrolyte additives for lithium-ion batteries. *Journal of Power Sources* **162**, 1379-1394 (2006).
- 15 Huang, X. & Hitt, J. Lithium ion battery separators: development and performance characterization of a composite membrane. *Journal of membrane science* **425**, 163-168 (2013).
- 16 Choi, J.-A., Kim, S. H. & Kim, D.-W. Enhancement of thermal stability and cycling performance in lithium-ion cells through the use of ceramic-coated separators. *Journal of Power Sources* **195**, 6192-6196 (2010).
- 17 Abraham, K. M. Exploding Hoverboards Explained. (2016).
- 18 Guyomard, D. & Tarascon, J. M. Rocking-chair or lithium-ion rechargeable lithium batteries. *Advanced Materials* **6**, 408-412 (1994).
- 19 Heiskanen, S. K., Kim, J. & Lucht, B. L. Generation and evolution of the solid electrolyte interphase of lithium-ion batteries. *Joule* **3**, 2322-2333 (2019).
- 20 Ganesh, P., Kent, P. & Jiang, D.-e. Solid-electrolyte interphase formation and electrolyte reduction at Li-ion battery graphite anodes: Insights from first-principles molecular dynamics. *The Journal of Physical Chemistry C* **116**, 24476-24481 (2012).
- 21 Aurbach, D., Zinigrad, E., Cohen, Y. & Teller, H. A short review of failure mechanisms of lithium metal and lithiated graphite anodes in liquid electrolyte solutions. *Solid state ionics* **148**, 405-416 (2002).
- 22 Laresgoiti, I., Käbitz, S., Ecker, M. & Sauer, D. U. Modeling mechanical degradation in lithium ion batteries during cycling: Solid electrolyte interphase fracture. *Journal of Power Sources* **300**, 112-122 (2015).

- 23 Lee, S. S., Kim, T. H., Hu, S. J., Cai, W. W. & Abell, J. A. in *ASME 2010 international manufacturing science and engineering conference*. 541-549 (American Society of Mechanical Engineers Digital Collection).
- 24 Buck, D. S., Fattig, R. N. & Silk, B. J. (Google Patents, 2009).
- 25 Rao, E. *et al.* Roll-to-roll functionalization of polyolefin separators for high-performance lithium-ion batteries. *ACS Applied Energy Materials* **1**, 3292-3300 (2018).
- 26 Wood III, D. L. *et al.* Perspectives on the relationship between materials chemistry and roll-to-roll electrode manufacturing for high-energy lithium-ion batteries. *Energy Storage Materials* (2020).
- 27 Kwade, A. *et al.* Current status and challenges for automotive battery production technologies. *Nature Energy* **3**, 290-300, doi:10.1038/s41560-018-0130-3 (2018).
- 28 Mohanty, D. *et al.* Non-destructive evaluation of slot-die-coated lithium secondary battery electrodes by in-line laser caliper and IR thermography methods. *Analytical Methods* **6**, 674-683 (2014).
- 29 Mohanty, D. *et al.* Effect of electrode manufacturing defects on electrochemical performance of lithium-ion batteries: Cognizance of the battery failure sources. *Journal of Power Sources* **312**, 70-79 (2016).
- 30 Kurfer, J., Westermeier, M., Tammer, C. & Reinhart, G. Production of large-area lithium-ion cells—Preconditioning, cell stacking and quality assurance. *CIRP annals* **61**, 1-4 (2012).
- 31 Zhang, S. S. A review on the separators of liquid electrolyte Li-ion batteries. *Journal of power sources* **164**, 351-364 (2007).
- 32 Schilling, A., Schmitt, J., Dietrich, F. & Dröder, K. Analyzing Bending Stresses on Lithium-Ion Battery Cathodes induced by the Assembly Process. *Energy Technology* **4**, 1502-1508 (2016).

- 33 Schmitt, J., Raatz, A., Dietrich, F., Dröder, K. & Hesselbach, J. Process and performance optimization by selective assembly of battery electrodes. *CIRP Annals* **63**, 9-12, doi:10.1016/j.cirp.2014.03.018 (2014).
- 34 Knoche, T., Surek, F. & Reinhart, G. A process model for the electrolyte filling of lithium-ion batteries. *Procedia CIRP* **41**, 405-410 (2016).
- 35 Lu, P., Li, C., Schneider, E. W. & Harris, S. J. Chemistry, impedance, and morphology evolution in solid electrolyte interphase films during formation in lithium ion batteries. *The Journal of Physical Chemistry C* **118**, 896-903 (2014).
- 36 Bridges, C. A., Sun, X.-G., Zhao, J., Paranthaman, M. P. & Dai, S. In situ observation of solid electrolyte interphase formation in ordered mesoporous hard carbon by small-angle neutron scattering. *The Journal of Physical Chemistry C* **116**, 7701-7711 (2012).
- 37 Imhof, R. & Novák, P. In situ investigation of the electrochemical reduction of carbonate electrolyte solutions at graphite electrodes. *Journal of The Electrochemical Society* **145**, 1081-1087 (1998).
- 38 Schröder, R., Aydemir, M. & Seliger, G. Comparatively Assessing different Shapes of Lithium-ion Battery Cells. *Procedia Manufacturing* **8**, 104-111, doi:10.1016/j.promfg.2017.02.013 (2017).
- 39 Kwade, A. *et al.* Current status and challenges for automotive battery production technologies. *Nature Energy* **3**, 290 (2018).
- 40 Lu, L., Han, X., Li, J., Hua, J. & Ouyang, M. A review on the key issues for lithium-ion battery management in electric vehicles. *Journal of power sources* **226**, 272-288 (2013).
- 41 Goodenough, J. B. & Kim, Y. Challenges for rechargeable Li batteries. *Chemistry of materials* **22**, 587-603 (2010).
- 42 Vetter, J. *et al.* Ageing mechanisms in lithium-ion batteries. *Journal of power sources* **147**, 269-281 (2005).

- 43 Jannesari, H., Emami, M. & Ziegler, C. Effect of electrolyte transport properties and variations in the morphological parameters on the variation of side reaction rate across the anode electrode and the aging of lithium ion batteries. *Journal of Power Sources* **196**, 9654-9664 (2011).
- 44 Song, M. & Choe, S.-Y. Fast and safe charging method suppressing side reaction and lithium deposition reaction in lithium ion battery. *Journal of Power Sources* **436**, 226835 (2019).
- 45 Arora, P., White, R. E. & Doyle, M. Capacity fade mechanisms and side reactions in lithium-ion batteries. *Journal of the Electrochemical Society* **145**, 3647 (1998).
- 46 Barré, A. *et al.* A review on lithium-ion battery ageing mechanisms and estimations for automotive applications. *Journal of Power Sources* **241**, 680-689 (2013).
- 47 Wohlfahrt-Mehrens, M., Vogler, C. & Garche, J. Aging mechanisms of lithium cathode materials. *Journal of power sources* **127**, 58-64 (2004).
- 48 Deshpande, R. D. & Bernardi, D. M. Modeling solid-electrolyte interphase (SEI) fracture: coupled mechanical/chemical degradation of the lithium ion battery. *Journal of The Electrochemical Society* **164**, A461 (2017).
- 49 Shin, H., Park, J., Sastry, A. M. & Lu, W. Degradation of the solid electrolyte interphase induced by the deposition of manganese ions. *Journal of Power Sources* **284**, 416-427 (2015).
- 50 Kim, T., Ono, L. K., Fleck, N., Raga, S. R. & Qi, Y. Transition metal speciation as a degradation mechanism with the formation of a solid-electrolyte interphase (SEI) in Ni-rich transition metal oxide cathodes. *Journal of Materials Chemistry A* **6**, 14449-14463 (2018).
- 51 Tang, C.-Y., Ma, Y., Haasch, R. T., Ouyang, J.-H. & Dillon, S. J. Insights into solid-electrolyte interphase induced Li-ion degradation from in situ auger electron spectroscopy. *The journal of physical chemistry letters* **8**, 6226-6230 (2017).

- 52 Kim, J., Kim, H., Ryu, J. H. & Oh, S. M. Communication—Lithium Bis (fluorosulfonyl) imide (LiFSI) as a Promising Salt to Suppress Solid Electrolyte Interphase Degradation at Elevated Temperatures. *Journal of The Electrochemical Society* **167**, 080529 (2020).
- 53 Balbuena, P. B. & Wang, Y. *Lithium-ion batteries: solid-electrolyte interphase*. (Imperial college press, 2004).
- 54 Liu, G. & Lu, W. A model of concurrent lithium dendrite growth, SEI growth, SEI penetration and regrowth. *Journal of the Electrochemical Society* **164**, A1826 (2017).
- 55 Deshpande, R., Verbrugge, M., Cheng, Y.-T., Wang, J. & Liu, P. Battery cycle life prediction with coupled chemical degradation and fatigue mechanics. *Journal of the Electrochemical Society* **159**, A1730 (2012).
- 56 Li, Z., Huang, J., Liaw, B. Y., Metzler, V. & Zhang, J. A review of lithium deposition in lithium-ion and lithium metal secondary batteries. *Journal of power sources* **254**, 168-182 (2014).
- 57 Perkins, R. D., Randall, A. V., Zhang, X. & Plett, G. L. Controls oriented reduced order modeling of lithium deposition on overcharge. *Journal of Power Sources* **209**, 318-325 (2012).
- 58 Aurbach, D. Review of selected electrode–solution interactions which determine the performance of Li and Li ion batteries. *Journal of Power Sources* **89**, 206-218 (2000).
- 59 Koltypin, M., Cohen, Y. S., Markovsky, B., Cohen, Y. & Aurbach, D. The study of lithium insertion–deinsertion processes into composite graphite electrodes by in situ atomic force microscopy (AFM). *Electrochemistry communications* **4**, 17-23 (2002).
- 60 Yamaki, J.-i. *et al.* A consideration of the morphology of electrochemically deposited lithium in an organic electrolyte. *Journal of Power Sources* **74**, 219-227 (1998).
- 61 Wen, J., Yu, Y. & Chen, C. A review on lithium-ion batteries safety issues: existing problems and possible solutions. *Materials express* **2**, 197-212 (2012).

- 62 Chen, Z., Christensen, L. & Dahn, J. Comparison of PVDF and PVDF-TFE-P as binders for electrode materials showing large volume changes in lithium-ion batteries. *Journal of The Electrochemical Society* **150**, A1073 (2003).
- 63 Voelker, P. Trace degradation analysis of lithium-ion battery components. *R&D Magazine*, (April 2014) <http://www.rdmag.com/articles/2014/04/trace-degradation-analysislithium-ion-battery-components> Search PubMed, (accessed August 2015) (2014).
- 64 Abe, K. *et al.* Additives-containing functional electrolytes for suppressing electrolyte decomposition in lithium-ion batteries. *Electrochimica acta* **49**, 4613-4622 (2004).
- 65 Andersson, A. M., Edström, K. & Thomas, J. O. Characterisation of the ambient and elevated temperature performance of a graphite electrode. *Journal of power sources* **81**, 8-12 (1999).
- 66 Ramadass, P., Haran, B., White, R. & Popov, B. N. Capacity fade of Sony 18650 cells cycled at elevated temperatures: Part I. Cycling performance. *Journal of power sources* **112**, 606-613 (2002).
- 67 Abraham, D. *et al.* Surface changes on LiNiO₂. 8CoO₂ particles during testing of high-power lithium-ion cells. *Electrochemistry communications* **4**, 620-625 (2002).
- 68 Venkatraman, S., Shin, Y. & Manthiram, A. Phase Relationships and Structural and Chemical Stabilities of Charged Li_{1-x}CoO_{2-δ} and Li_{1-x}NiO_{2-δ} Cathodes. *Electrochemical and solid-state letters* **6**, A9-A12 (2003).
- 69 Park, J., Seo, J. H., Plett, G., Lu, W. & Sastry, A. M. Numerical simulation of the effect of the dissolution of LiMn₂O₄ particles on Li-ion battery performance. *Electrochemical and Solid-State Letters* **14**, A14-A18 (2011).
- 70 Bandhauer, T. M., Garimella, S. & Fuller, T. F. A critical review of thermal issues in lithium-ion batteries. *Journal of the Electrochemical Society* **158**, R1-R25 (2011).
- 71 Wang, X., Gaustad, G., Babbitt, C. W. & Richa, K. Economies of scale for future lithium-ion battery recycling infrastructure. *Resources, Conservation and Recycling* **83**, 53-62 (2014).

- 72 Bernardes, A. M., Espinosa, D. C. R. & Tenório, J. S. Recycling of batteries: a review of current processes and technologies. *Journal of Power Sources* **130**, 291-298 (2004).
- 73 Li, Y. *et al.* Leaching of heavy metals from E-waste in simulated landfill columns. *Waste Management* **29**, 2147-2150 (2009).
- 74 Yun, L. *et al.* Metallurgical and mechanical methods for recycling of lithium-ion battery pack for electric vehicles. *Resources, Conservation and Recycling* **136**, 198-208 (2018).
- 75 Winslow, K. M., Laux, S. J. & Townsend, T. G. A review on the growing concern and potential management strategies of waste lithium-ion batteries. *Resources, Conservation and Recycling* **129**, 263-277 (2018).
- 76 Meshram, P., Pandey, B. & Mankhand, T. Recovery of valuable metals from cathodic active material of spent lithium ion batteries: Leaching and kinetic aspects. *Waste management* **45**, 306-313 (2015).
- 77 Xu, J. *et al.* A review of processes and technologies for the recycling of lithium-ion secondary batteries. *Journal of Power Sources* **177**, 512-527, doi:10.1016/j.jpowsour.2007.11.074 (2008).
- 78 Hu, J., Zhang, J., Li, H., Chen, Y. & Wang, C. A promising approach for the recovery of high value-added metals from spent lithium-ion batteries. *Journal of Power Sources* **351**, 192-199 (2017).
- 79 Gratz, E., Sa, Q., Apelian, D. & Wang, Y. A closed loop process for recycling spent lithium ion batteries. *Journal of Power Sources* **262**, 255-262 (2014).
- 80 Yang, T. *et al.* An Effective Relithiation Process for Recycling Lithium-Ion Battery Cathode Materials. *Advanced Sustainable Systems* **4**, 1900088 (2020).
- 81 Li, X., Zhang, J., Song, D., Song, J. & Zhang, L. Direct regeneration of recycled cathode material mixture from scrapped LiFePO₄ batteries. *Journal of Power Sources* **345**, 78-84 (2017).
- 82 Lv, W. *et al.* A Critical Review and Analysis on the Recycling of Spent Lithium-Ion Batteries. *ACS Sustainable Chemistry & Engineering* **6**, 1504-1521, doi:10.1021/acssuschemeng.7b03811 (2018).

- 83 Harper, G. *et al.* Recycling lithium-ion batteries from electric vehicles. *Nature* **575**, 75-86 (2019).
- 84 Pistoia, G. & Liaw, B. *Behaviour of Lithium-Ion Batteries in Electric Vehicles: Battery Health, Performance, Safety, and Cost.* (Springer, 2018).
- 85 Herrmann, C., Raatz, A., Andrew, S. & Schmitt, J. Scenario-Based Development of Disassembly Systems for Automotive Lithium Ion Battery Systems. *Advanced Materials Research* **907**, 391-401, doi:10.4028/www.scientific.net/AMR.907.391 (2014).
- 86 Adhikaree, A. *et al.* in *2017 IEEE Energy Conversion Congress and Exposition (ECCE)*. 1004-1009 (IEEE).
- 87 Maharshi, S. Cloud based disassembly of electric vehicle battery. *Procedia Manufacturing* **30**, 136-142 (2019).
- 88 Schmitt, J., Haupt, H., Kurrat, M. & Raatz, A. in *2011 15th International Conference on Advanced Robotics (ICAR)*. 291-297 (IEEE).
- 89 Wegener, K., Andrew, S., Raatz, A., Dröder, K. & Herrmann, C. Disassembly of electric vehicle batteries using the example of the Audi Q5 hybrid system. *Procedia CIRP* **23**, 155-160 (2014).
- 90 Wegener, K., Chen, W. H., Dietrich, F., Dröder, K. & Kara, S. Robot assisted disassembly for the recycling of electric vehicle batteries. *Procedia Cirp* **29**, 716-721 (2015).
- 91 Luo, J., Solowjow, E., Wen, C., Ojea, J. A. & Agogino, A. M. in *2018 IEEE/RSJ International Conference on Intelligent Robots and Systems (IROS)*. 2062-2069 (IEEE).
- 92 Inoue, T., De Magistris, G., Munawar, A., Yokoya, T. & Tachibana, R. in *2017 IEEE/RSJ International Conference on Intelligent Robots and Systems (IROS)*. 819-825 (IEEE).
- 93 Nerakae, P., Uangpairaj, P. & Chamniprasart, K. Using machine vision for flexible automatic assembly system. *Procedia Computer Science* **96**, 428-435 (2016).
- 94 Öhl, J., Horn, D., Zimmermann, J., Stauber, R. & Gutfleisch, O. in *Materials Science Forum*. 74-78 (Trans Tech Publ).

- 95 Shin, S. M., Kim, N. H., Sohn, J. S., Yang, D. H. & Kim, Y. H. Development of a metal recovery process from Li-ion battery wastes. *Hydrometallurgy* **79**, 172-181 (2005).
- 96 Pagnanelli, F., Moscardini, E., Altimari, P., Atia, T. A. & Toro, L. Cobalt products from real waste fractions of end of life lithium ion batteries. *Waste management* **51**, 214-221 (2016).
- 97 Hanisch, C. *et al.* Recycling of lithium-ion batteries: a novel method to separate coating and foil of electrodes. *Journal of cleaner production* **108**, 301-311 (2015).
- 98 Zeng, X., Li, J. & Shen, B. Novel approach to recover cobalt and lithium from spent lithium-ion battery using oxalic acid. *Journal of hazardous materials* **295**, 112-118 (2015).
- 99 Zhang, X. *et al.* Toward sustainable and systematic recycling of spent rechargeable batteries. *Chem Soc Rev* **47**, 7239-7302, doi:10.1039/c8cs00297e (2018).
- 100 Hess, S., Wohlfahrt-Mehrens, M. & Wachtler, M. Flammability of Li-ion battery electrolytes: flash point and self-extinguishing time measurements. *Journal of The Electrochemical Society* **162**, A3084 (2015).
- 101 Wang, Q., Sun, J. & Chu, G. Lithium ion battery fire and explosion. *Fire Safety Science* **8**, 375-382 (2005).
- 102 Diekmann, J. *et al.* Ecological recycling of lithium-ion batteries from electric vehicles with focus on mechanical processes. *Journal of the Electrochemical Society* **164**, A6184-A6191 (2017).
- 103 Diekmann, J., Rothermel, S., Nowak, S. & Kwade, A. in *Recycling of Lithium-Ion Batteries* 33-38 (Springer, 2018).
- 104 Diekmann, J., Hanisch, C., Loellhoeffel, T., Schällicke, G. & Kwade, A. Ecologically Friendly Recycling of Lithium-Ion Batteries-the LithoRec Process. *ECS Transactions* **73**, 1 (2016).
- 105 Yan, J. *Handbook of Clean Energy Systems, 6 Volume Set*. Vol. 5 (John Wiley & Sons, 2015).

- 106 Diekmann, J. *et al.* Ecological Recycling of Lithium-Ion Batteries from Electric Vehicles with Focus on Mechanical Processes. *Journal of The Electrochemical Society* **164**, A6184-A6191, doi:10.1149/2.0271701jes (2016).
- 107 Contestabile, M., Panero, S. & Scrosati, B. A laboratory-scale lithium-ion battery recycling process. *Journal of Power Sources* **92**, 65-69 (2001).
- 108 Hanisch, C., Haselrieder, W. & Kwade, A. in *Glocalized Solutions for Sustainability in Manufacturing* 85-89 (Springer, 2011).
- 109 Hanisch, C. *et al.* In-production recycling of active materials from lithium-ion battery scraps. *ECS Transactions* **64**, 131 (2015).
- 110 Hanisch, C., Haselrieder, W. & Kwade, A. (Google Patents, 2017).
- 111 Li, J., Shi, P., Wang, Z., Chen, Y. & Chang, C.-C. A combined recovery process of metals in spent lithium-ion batteries. *Chemosphere* **77**, 1132-1136 (2009).
- 112 Li, L., Chen, R., Sun, F., Wu, F. & Liu, J. Preparation of LiCoO₂ films from spent lithium-ion batteries by a combined recycling process. *Hydrometallurgy* **108**, 220-225 (2011).
- 113 Li, L. *et al.* Ascorbic-acid-assisted recovery of cobalt and lithium from spent Li-ion batteries. *Journal of Power Sources* **218**, 21-27 (2012).
- 114 Song, D. *et al.* Heat treatment of LiCoO₂ recovered from cathode scraps with solvent method. *Journal of Power Sources* **249**, 137-141 (2014).
- 115 Song, X. *et al.* Direct regeneration of cathode materials from spent lithium iron phosphate batteries using a solid phase sintering method. *RSC advances* **7**, 4783-4790 (2017).
- 116 Toma, C. *et al.* in *IOP Conference Series: Materials Science and Engineering*. 012034 (IOP Publishing).
- 117 Fouad, O., Farghaly, F. & Bahgat, M. A novel approach for synthesis of nanocrystalline γ -LiAlO₂ from spent lithium-ion batteries. *Journal of analytical and applied pyrolysis* **78**, 65-69 (2007).

- 118 Bahgat, M., Farghaly, F., Basir, S. A. & Fouad, O. Synthesis, characterization and magnetic properties of microcrystalline lithium cobalt ferrite from spent lithium-ion batteries. *Journal of materials processing technology* **183**, 117-121 (2007).
- 119 Sun, Z. *et al.* Toward sustainability for recovery of critical metals from electronic waste: the hydrochemistry processes. *ACS Sustainable Chemistry & Engineering* **5**, 21-40 (2017).
- 120 Xiao, J., Li, J. & Xu, Z. Recycling metals from lithium ion battery by mechanical separation and vacuum metallurgy. *Journal of hazardous materials* **338**, 124-131 (2017).
- 121 Georgi-Maschler, T., Friedrich, B., Weyhe, R., Heegn, H. & Rutz, M. Development of a recycling process for Li-ion batteries. *Journal of power sources* **207**, 173-182 (2012).
- 122 Yao, Y. *et al.* Hydrometallurgical processes for recycling spent lithium-ion batteries: a critical review. *ACS Sustainable Chemistry & Engineering* **6**, 13611-13627 (2018).
- 123 Larcher, D. & Tarascon, J.-M. Towards greener and more sustainable batteries for electrical energy storage. *Nature chemistry* **7**, 19-29 (2015).
- 124 Chagnes, A. & Pospiech, B. A brief review on hydrometallurgical technologies for recycling spent lithium-ion batteries. *Journal of Chemical Technology & Biotechnology* **88**, 1191-1199 (2013).
- 125 Li, L. *et al.* Sustainable recovery of cathode materials from spent lithium-ion batteries using lactic acid leaching system. *ACS Sustainable Chemistry & Engineering* **5**, 5224-5233 (2017).
- 126 Nayaka, G. P. *et al.* An environmental friendly attempt to recycle the spent Li-ion battery cathode through organic acid leaching. *Journal of Environmental Chemical Engineering* **7**, doi:10.1016/j.jece.2018.102854 (2019).
- 127 Song, D. *et al.* Recovery and heat treatment of the Li (Ni_{1/3}Co_{1/3}Mn_{1/3}) O₂ cathode scrap material for lithium ion battery. *Journal of power sources* **232**, 348-352 (2013).

- 128 Mantuano, D. P., Dorella, G., Elias, R. C. A. & Mansur, M. B. Analysis of a hydrometallurgical route to recover base metals from spent rechargeable batteries by liquid–liquid extraction with Cyanex 272. *Journal of Power Sources* **159**, 1510-1518 (2006).
- 129 Tanong, K., Coudert, L., Mercier, G. & Blais, J.-F. Recovery of metals from a mixture of various spent batteries by a hydrometallurgical process. *Journal of environmental management* **181**, 95-107 (2016).
- 130 Wang, F., Sun, R., Xu, J., Chen, Z. & Kang, M. Recovery of cobalt from spent lithium ion batteries using sulphuric acid leaching followed by solid–liquid separation and solvent extraction. *RSC advances* **6**, 85303-85311 (2016).
- 131 Wang, R.-C., Lin, Y.-C. & Wu, S.-H. A novel recovery process of metal values from the cathode active materials of the lithium-ion secondary batteries. *Hydrometallurgy* **99**, 194-201 (2009).
- 132 Barik, S., Prabakaran, G. & Kumar, L. Leaching and separation of Co and Mn from electrode materials of spent lithium-ion batteries using hydrochloric acid: Laboratory and pilot scale study. *Journal of Cleaner Production* **147**, 37-43 (2017).
- 133 Takacova, Z., Havlik, T., Kukurugya, F. & Orac, D. Cobalt and lithium recovery from active mass of spent Li-ion batteries: Theoretical and experimental approach. *Hydrometallurgy* **163**, 9-17 (2016).
- 134 Barbieri, E., Lima, E., Cantarino, S., Lelis, M. & Freitas, M. Recycling of spent ion-lithium batteries as cobalt hydroxide, and cobalt oxide films formed under a conductive glass substrate, and their electrochemical properties. *Journal of Power Sources* **269**, 158-163 (2014).
- 135 Barbieri, E., Lima, E., Lelis, M. & Freitas, M. Recycling of cobalt from spent Li-ion batteries as β -Co(OH)₂ and the application of Co₃O₄ as a pseudocapacitor. *Journal of Power Sources* **270**, 158-165 (2014).
- 136 Lee, C. K. & Rhee, K.-I. Reductive leaching of cathodic active materials from lithium ion battery wastes. *Hydrometallurgy* **68**, 5-10 (2003).

- 137 Castillo, S., Ansart, F., Laberty-Robert, C. & Portal, J. Advances in the recovering of spent lithium battery compounds. *Journal of Power Sources* **112**, 247-254 (2002).
- 138 Li, J. *et al.* Study of extraction and purification of Ni, Co and Mn from spent battery material. *Hydrometallurgy* **99**, 7-12 (2009).
- 139 Meshram, P., Pandey, B. D., Mankhand, T. R. & Deveci, H. Comparision of different reductants in leaching of spent lithium ion batteries. *Jom* **68**, 2613-2623 (2016).
- 140 Pagnanelli, F. *et al.* Acid reducing leaching of cathodic powder from spent lithium ion batteries: glucose oxidative pathways and particle area evolution. *Journal of Industrial and Engineering Chemistry* **20**, 3201-3207 (2014).
- 141 Yang, L. *et al.* Preparation and magnetic performance of $\text{Co}_0.8\text{Fe}_{2.2}\text{O}_4$ by a sol–gel method using cathode materials of spent Li-ion batteries. *Ceramics International* **42**, 1897-1902 (2016).
- 142 Nayaka, G., Pai, K., Santhosh, G. & Manjanna, J. Dissolution of cathode active material of spent Li-ion batteries using tartaric acid and ascorbic acid mixture to recover Co. *Hydrometallurgy* **161**, 54-57 (2016).
- 143 Pinna, E. G., Ruiz, M. C., Ojeda, M. W. & Rodriguez, M. H. Cathodes of spent Li-ion batteries: Dissolution with phosphoric acid and recovery of lithium and cobalt from leach liquors. *Hydrometallurgy* **167**, 66-71 (2017).
- 144 Ferreira, D. A., Prados, L. M. Z., Majuste, D. & Mansur, M. B. Hydrometallurgical separation of aluminium, cobalt, copper and lithium from spent Li-ion batteries. *Journal of Power Sources* **187**, 238-246 (2009).
- 145 Zheng, Y. *et al.* Leaching procedure and kinetic studies of cobalt in cathode materials from spent lithium ion batteries using organic citric acid as leachant. *International Journal of Environmental Research* **10**, 159-168 (2016).

- 146 Sun, L. & Qiu, K. Organic oxalate as leachant and precipitant for the recovery of valuable metals from spent lithium-ion batteries. *Waste management* **32**, 1575-1582 (2012).
- 147 Liang, Y. *et al.* Life cycle assessment of lithium-ion batteries for greenhouse gas emissions. *Resources, conservation and recycling* **117**, 285-293 (2017).
- 148 Yang, L., Xi, G. & Xi, Y. Recovery of Co, Mn, Ni, and Li from spent lithium ion batteries for the preparation of $\text{LiNi}_{1/3}\text{Co}_{1/3}\text{Mn}_{1/3}\text{O}_2$ cathode materials. *Ceramics international* **41**, 11498-11503 (2015).
- 149 Cai, G., Fung, K. Y., Ng, K. M. & Wibowo, C. Process development for the recycle of spent lithium ion batteries by chemical precipitation. *Industrial & Engineering Chemistry Research* **53**, 18245-18259 (2014).
- 150 Joulié, M., Laucournet, R. & Billy, E. Hydrometallurgical process for the recovery of high value metals from spent lithium nickel cobalt aluminum oxide based lithium-ion batteries. *Journal of Power Sources* **247**, 551-555 (2014).
- 151 He, L.-P., Sun, S.-Y., Song, X.-F. & Yu, J.-G. Leaching process for recovering valuable metals from the $\text{LiNi}_{1/3}\text{Co}_{1/3}\text{Mn}_{1/3}\text{O}_2$ cathode of lithium-ion batteries. *Waste management* **64**, 171-181 (2017).
- 152 Li, L. *et al.* Recovery of valuable metals from spent lithium-ion batteries by ultrasonic-assisted leaching process. *Journal of Power Sources* **262**, 380-385 (2014).
- 153 Nie, H. *et al.* LiCoO_2 : recycling from spent batteries and regeneration with solid state synthesis. *Green chemistry* **17**, 1276-1280 (2015).
- 154 Chen, J. *et al.* Environmentally friendly recycling and effective repairing of cathode powders from spent LiFePO_4 batteries. *Green Chemistry* **18**, 2500-2506 (2016).
- 155 Chen, S. *et al.* Renovation of LiCoO_2 with outstanding cycling stability by thermal treatment with Li_2CO_3 from spent Li-ion batteries. *Journal of Energy Storage* **8**, 262-273 (2016).

- 156 Shi, Y., Chen, G. & Chen, Z. Effective regeneration of LiCoO₂ from spent lithium-ion batteries: a direct approach towards high-performance active particles. *Green Chemistry* **20**, 851-862, doi:10.1039/c7gc02831h (2018).
- 157 Dewulf, J. *et al.* Recycling rechargeable lithium ion batteries: Critical analysis of natural resource savings. *Resources, Conservation and Recycling* **54**, 229-234 (2010).
- 158 Zou, H., Gratz, E., Apelian, D. & Wang, Y. A novel method to recycle mixed cathode materials for lithium ion batteries. *Green Chemistry* **15**, 1183-1191 (2013).
- 159 Zhang, T. *et al.* Surface analysis of cobalt-enriched crushed products of spent lithium-ion batteries by X-ray photoelectron spectroscopy. *Separation and Purification Technology* **138**, 21-27 (2014).
- 160 Herrmann, C., Raatz, A., Mennenga, M., Schmitt, J. & Andrew, S. in *Leveraging Technology for a Sustainable World* 149-154 (Springer, 2012).
- 161 Weyrich, M., Natkunarajah, N. & Sc, M. Conception of an automated plant for the disassembly of lithium ion batteries. *Germany, Paul-Bonatz-Str*, 9-11.
- 162 Zhang, T. *et al.* Chemical and process mineralogical characterizations of spent lithium-ion batteries: an approach by multi-analytical techniques. *Waste management* **34**, 1051-1058 (2014).
- 163 Sa, Q. *et al.* Synthesis of high performance LiNi_{1/3}Mn_{1/3}Co_{1/3}O₂ from lithium ion battery recovery stream. *Journal of Power Sources* **282**, 140-145 (2015).
- 164 Guo, L. & Liu, G. W. in *Advanced Materials Research*. 983-988 (Trans Tech Publ).
- 165 Zhang, G. Q., Li, L. M. & Choi, S. in *2012 IEEE International Conference on Technologies for Practical Robot Applications (TePRA)*. 117-120 (IEEE).
- 166 Yao, L., Xi, Y., Xi, G. & Feng, Y. Synthesis of cobalt ferrite with enhanced magnetostriction properties by the sol–gel–hydrothermal route using spent Li-ion battery. *Journal of Alloys and Compounds* **680**, 73-79 (2016).

- 167 Santana, I., Moreira, T., Lelis, M. & Freitas, M. Photocatalytic properties of Co₃O₄/LiCoO₂ recycled from spent lithium-ion batteries using citric acid as leaching agent. *Materials Chemistry and Physics* **190**, 38-44 (2017).
- 168 Yang, Z. *et al.* Different types of MnO₂ recovered from spent LiMn₂O₄ batteries and their application in electrochemical capacitors. *Journal of Materials Science* **48**, 2512-2519 (2013).
- 169 Moura, M. *et al.* Synthesis, characterization and photocatalytic properties of nanostructured CoFe₂O₄ recycled from spent Li-ion batteries. *Chemosphere* **182**, 339-347 (2017).
- 170 Senćanski, J. *et al.* The synthesis of Li (CoMnNi) O₂ cathode material from spent-Li ion batteries and the proof of its functionality in aqueous lithium and sodium electrolytic solutions. *Journal of Power Sources* **342**, 690-703 (2017).
- 171 Perez, E. *et al.* Recovery of metals from simulant spent lithium-ion battery as organophosphonate coordination polymers in aqueous media. *Journal of hazardous materials* **317**, 617-621 (2016).
- 172 Curry, C. Lithium-ion battery costs and market. *Bloomberg New Energy Finance* **5** (2017).
- 173 Peterson, S. B., Apt, J. & Whitacre, J. Lithium-ion battery cell degradation resulting from realistic vehicle and vehicle-to-grid utilization. *Journal of Power Sources* **195**, 2385-2392 (2010).
- 174 Ellingsen, L. A. W. *et al.* Life cycle assessment of a lithium-ion battery vehicle pack. *Journal of Industrial Ecology* **18**, 113-124 (2014).
- 175 Sun, X., Hao, H., Zhao, F. & Liu, Z. Tracing global lithium flow: A trade-linked material flow analysis. *Resources, Conservation and Recycling* **124**, 50-61 (2017).
- 176 Zhang, X. *et al.* Toward sustainable and systematic recycling of spent rechargeable batteries. *Chemical Society Reviews* **47**, 7239-7302 (2018).
- 177 Shi, Y., Chen, G. & Chen, Z. Effective regeneration of LiCoO₂ from spent lithium-ion batteries: a direct approach towards high-performance active particles. *Green Chemistry* **20**, 851-862 (2018).

- 178 Kim, D.-S. *et al.* Simultaneous separation and renovation of lithium cobalt oxide from the cathode
of spent lithium ion rechargeable batteries. *Journal of Power Sources* **132**, 145-149 (2004).
- 179 Zheng, L., Sturges, R., Li, L. & Yang, T.
- 180 Schröder, R., Glodde, A., Aydemir, M. & Bach, G. in *Applied Mechanics and Materials*. 19-26 (Trans
Tech Publ).
- 181 LeCun, Y., Bengio, Y. & Hinton, G. Deep learning. *nature* **521**, 436-444 (2015).
- 182 Zheng, H., Fu, J., Mei, T. & Luo, J. in *Proceedings of the IEEE international conference on computer
vision*. 5209-5217.
- 183 Farrugia, H. Convolutional Neural Networks (CNNs) and Use Cases in Health. (2019).
- 184 Meshram, P., Pandey, B. & Mankhand, T. Extraction of lithium from primary and secondary
sources by pre-treatment, leaching and separation: A comprehensive review. *Hydrometallurgy*
150, 192-208 (2014).
- 185 Tedjar, F. Challenges for recycling advanced Li-ion batteries. (2013).
- 186 Katwala, A. The spiralling environmental cost of our lithium battery addiction. . (2018).
- 187 Els, P. Will lithium-ion battery supply slow the EV revolution? (2019).
- 188 Eckart, J. Batteries can be part of the fight against climate change - if we do these five things.
(2017).
- 189 Xu, J. *et al.* A review of processes and technologies for the recycling of lithium-ion secondary
batteries. *Journal of Power Sources* **177**, 512-527 (2008).
- 190 Li, L. *et al.* Disassembly Automation for Recycling End-of-Life Lithium-Ion Pouch Cells. *JOM* **71**,
4457-4464 (2019).
- 191 Li, L. *et al.* Disassembly Automation for Recycling End-of-Life Lithium-Ion Pouch Cells. *JOM*, 1-8
(2019).
- 192 Kendall, M. G. The advanced theory of statistics. *The advanced theory of statistics*. (1946).

- 193 Neyman, J. Outline of a theory of statistical estimation based on the classical theory of probability. *Philosophical Transactions of the Royal Society of London. Series A, Mathematical and Physical Sciences* **236**, 333-380 (1937).
- 194 Bland, J. M. & Peacock, J. L. Interpreting statistics with confidence. *The Obstetrician & Gynaecologist* **4**, 176-180 (2002).
- 195 Du Prel, J.-B., Hommel, G., Röhrig, B. & Blettner, M. Confidence interval or p-value?: part 4 of a series on evaluation of scientific publications. *Deutsches Ärzteblatt International* **106**, 335 (2009).
- 196 Hedayat, A. S., Sloane, N. J. A. & Stufken, J. *Orthogonal arrays: theory and applications*. (Springer Science & Business Media, 2012).
- 197 Taguchi, G. & Konishi, S. *Orthogonal arrays and linear graphs*. (na, 1987).
- 198 Sloane, N. J. A library of orthogonal arrays. *Fixed-level arrays with more than three levels: OA* **16** (2007).
- 199 Wang, W. & Wu, Y. An overview of recycling and treatment of spent LiFePO₄ batteries in China. *Resources, Conservation and Recycling* **127**, 233-243 (2017).
- 200 McClenathan, D. M., Wetzol, W. C., Lorge, S. E. & Hieftje, G. M. Effect of the plasma operating frequency on the figures of merit of an inductively coupled plasma time-of-flight mass spectrometer. *Journal of Analytical Atomic Spectrometry* **21**, 160-167 (2006).
- 201 Sloop, S. *et al.* A direct recycling case study from a lithium-ion battery recall. *Sustainable Materials and Technologies* **25**, e00152 (2020).
- 202 Gao, Y., Li, Y., Li, J., Xie, H. & Chen, Y. Direct recovery of LiCoO₂ from the recycled lithium-ion batteries via structure restoration. *Journal of Alloys and Compounds*, 156234 (2020).
- 203 Liu, Y.-J., Hu, Q.-Y., Li, X.-H., Wang, Z.-X. & Guo, H.-J. Recycle and synthesis of LiCoO₂ from incisors bound of Li-ion batteries. *Transactions of Nonferrous Metals Society of China* **16**, 956-959 (2006).

- 204 Zheng, P. *The Design and Optimization of a Lithium-ion Battery Direct Recycling Process*, Virginia Tech, (2019).
- 205 Ge, D. *Direct Lithium-ion Battery Recycling to Yield Battery Grade Cathode Materials*, Virginia Tech, (2019).
- 206 Jie, Y. *et al.* in *REWAS 2019* 401-409 (Springer, 2019).
- 207 Song, X. *et al.* Direct regeneration of cathode materials from spent lithium iron phosphate batteries using a solid phase sintering method. *RSC Advances* **7**, 4783-4790, doi:10.1039/c6ra27210j (2017).
- 208 Natarajan, S., Lakshmi, D. S., Bajaj, H. C. & Srivastava, D. N. Recovery and utilization of graphite and polymer materials from spent lithium-ion batteries for synthesizing polymer-graphite nanocomposite thin films. *Journal of Environmental Chemical Engineering* **3**, 2538-2545 (2015).
- 209 Asif, A. A. & Singh, R. Further cost reduction of battery manufacturing. *Batteries* **3**, 17 (2017).